Universidad de Granada
FisyMat

Multi-band

galaxy surveys

William Schoenell

Advised by: Narciso Benítez

Editor: Universidad de Granada. Tesis Doctorales
Autor: William Schoenell
ISBN: 978-84-9163-574-1
URI: http://hdl.handle.net/10481/48451

El doctorando William Schoenell y el director de la tesis Narciso Benítez Lozano

Garantizamos, al firmar esta tesis doctoral, que el trabajo ha sido realizado por el doctorando bajo la dirección de los directores de la tesis y hasta donde nuestro conocimiento alcanza, en la realización del trabajo, se han respetado los derechos de otros autores a ser citados, cuando se han utilizado sus resultados o publicaciones.

Lugar y fecha: Granada, 12 de Junio de 2017

Director de la Tesis	Doctorando
Firma	Firma

Abstract

This doctorate thesis covers the use of recent astronomical surveys and statistical techniques to answer questions about the composition of galaxies, by following two different perspectives: the instruments needed to gather the data and the development of a statistical tool to turn the observed data into physical properties of galaxies.

We start by giving some background contextualization about the largest extragalactic surveys to date, and how they influenced the three surveys studied in this thesis: the S-PLUS survey, the ALHAMBRA survey, and the J-PAS survey.

The first half of this work is dedicated to the S-PLUS survey, a Local Universe survey that started at the beginning of 2017 and is designed to study nearby galaxies in 12 bands with a 80 cm telescope. Its design, installation, and commissioning occurred in the course of this thesis and both hard and software components of the observatory are described as well how they are projected to map the sky autonomously every night.

In the second half of this work, we turn our attention into the data generated by other two multi-band surveys: the ALHAMBRA and J-PAS surveys. The ALHAMBRA survey, which completed the map of 3 deg^2 in 20 medium band optical filters on 2014, provided the photometric data and redshifts (photo-zs) used in this work. The studies performed here with the ALHAMBRA data will provide guidelines to explore the data of its successor, the J-PAS survey, which starts next year building a map of the whole northern sky in 56 narrow band filters.

We show how the problem of the estimation of the photo-z in the Universe is unfolded by the use of Bayesian statistics, where galaxies positions are described not by a single point estimator, but by a probability distribution function (PDF). Within the Bayesian photo-z framework, we develop a method for estimation of galaxy properties using the template-redshift PDFs given by photometric redshift codes as, for example, the BPZ code. We propose a concrete implementation of this method by fitting the photo-z templates with composite stellar populations models, or τ-models. The output of the proposed implementation is used to, in combination to the ALHAMBRA photo-z PDFs, estimate galaxies stellar properties like the mean ages, extinctions, and stellar masses. The derived stellar mass PDFs were used to estimate the stellar mass function in different redshift bins.

The resulting ages, stellar masses, and the stellar mass functions are shown to be systematically inclined to make galaxies bluer and, hence, less massive than the expected. This deficit of massive galaxies in the application of the method is discussed, and the solution proposed relies on changing the photo-z templates to more physical realistic ones while maintaining the so-pursued photo-z precision.

Resúmen

Esta tesis de doctorado abarca el uso de cartografiados astronómicos recientes y de técnicas estadísticas avanzadas para responder a preguntas acerca de la composición de galaxias, siguiendo dos perspectivas diferentes: la instrumentación necesaria para obtener los datos y el desarrollo de una herramienta estadística que permita convertir los datos observados en propiedades físicas de galaxias.

Comenzamos contextualizando sobre los cartografiados extragalácticos más grandes hasta la fecha y cómo influyeron en los tres cartografiados estudiados en esta tesis: S-PLUS, ALHAMBRA y J-PAS.

En la primera parte de este trabajo nos centramos en S-PLUS, un cartografiado del Universo Local que comenzó a principios de 2017 para estudiar galaxias cercanas utilizando 12 bandas con un telescopio de 80 cm. Su diseño, instalación, y puesta en funcionamento tuvo lugar en el transcurso de esta tesis en la que describimos tanto el hardware como el software utilizado, así como su autonomía para realizar el cartografiado del cielo cada noche.

En la segunda parte de este trabajo, nos centramos en los datos obtenidos por otros dos cartografiados de varias bandas: ALHAMBRA y J-PAS. El cartografiado ALHAMBRA, que completó el mapeado de 3 $\deg^2$ con 20 filtros ópticos de banda media en 2014, fproporcionó los datos fotométricos y redshifts (photo-zs) utilizados en este trabajo. Los estudios realizados con ALHAMBRA abrirán el camino para explorar los datos de su sucesor, J-PAS, que comenzará el próximo año a mapear el cielo septentrional con un conjunto de 56 filtros estrechos.

Mostramos cómo realizamos la estimación de los photo-z en el Universo mediante estadística bayesiana, describiendo la posición de las galaxias no mediante un simple punto, si no a través de una función de distribución de probabilidad (FDP). En este contexto, desarrollamos un método para estimar las propiedades de las galaxias utilizando los modelos de FDPs generadas por códigos de photo-z, por ejemplo, el código BPZ. Aplicamos este método para ajustar los modelos de photo-z con los modelos de poblaciones estelares compuestas, o τ-models. El resultado de estos ajustes se utiliza, combinando con las FDPs de ALHAMBRA, para estimar las propiedades estelares de las galaxias, como la edad media, extinción y masa estelar. Las FDPs de la masa se utilizan para estimar la función de masa estelar para diferentes intervalos de z.

Las edades obtenidas, masas estelares y las funciones de masa estelar muestran una tendencia que apunta a galaxies más azules y, por tanto, menos masivas que las esperadas. Discutimos esta falta de galaxias masivas, y la solución propuesta pasa por un cambio en los modelos de photo-z para que sean más realistas a la vez que mantienen la deseada precisión de los photo-z.

Table of Contents

Chapter One

Introduction

Surveys are a primary source of knowledge in any area of astronomy, from planets and stars to galaxies and the Universe. Astronomical surveys provide abundant, reliable, and homogeneous data, facilitating the adoption of statistical techniques for data mining. This thesis works with photometric surveys, presenting developments both in the instrumental/observational level and data analysis techniques. After a brief history of surveys in astronomy, this introductory chapter presents the specific surveys worked on during this doctorate.

1.1 A brief history of galaxy surveys

It dates from 1750, from Thomas Wright's book *An original theory or new hypothesis of the Universe*, the first idea that our vision of the Milky Way would be a projection, an "optical effect", of a subject which is inside a flat distribution of stars. He wrote,

> *To a spectator placed in an indefinite Space, all very remote Objects, appear to be equally distant to the observer Eye; and if we judge the Via Lactea from Phænomena only, we must of course conclude it a vast Ring of Stars, scattered promiscuously round the celestial Regions in the Direction of a perfect circle.*

Inspired by Wright, Immanuel Kant, in 1755 proposed in his book *Allgemeine Naturgeschichte und Theorie des Himmels* (Universal Natural History and Theory of Heaven) that the "Nebular Clouds", already discovered but with unknown nature were other "Island Universes" such as the one which we live.

From then on, these nebulae were cataloged, reaching thousands of known nebulae in 1885, when Caroline Herschel organized and presented the work of his deceased brother William Herschel, to the Royal Academy of Göttingen, eight volumes of the works *Book of Sweeps* and *The General Catalogue of Nebulae*. Due to this tremendous effort on the objects compilation, she earned a Golden medal from the Royal Astronomical Society.

In the following years, more of those nebulae were discovered, but the debate on whether these objects were part of our galaxy or they were galaxies remained open.

It was just a century ago, in 1920, where astronomers were still discussing the nature of these nebulae, more precisely "spiral nebulae" like Andromeda, whether they were part of our Galaxy, or "island universes", i.e., other galaxies. In the "Great Debate", promoted by National Academy of Sciences, Harlow Shapley and Heber D. Curtis discussed the scales of the Universe. While Shapley was for a Universe of the size of the Milky way, where these "spiral nebulae" are just gas clouds in the outskirts of the Galaxy, Curtis argued that these unusual objects are, in fact, distant galaxies and that we inhabit one of the many galaxies in the Universe.

The final solution for the Debate came with the accurate measurement of the distances to M31 and M33. This solution was achieved by the American astronomer Edwin Hubble in 1925. Using the relationship between the variability period and the absolute magnitudes of Cepheid stars, discovered by Henrietta Leavitt in 1912, Hubble estimated the distance to these famous spiral nebulae, obtaining values that put them outside the realm of our Galaxy.

Four years later, in 1929, Hubble revisited the relationship between the distance of the galaxies and their radial velocities and found a linear relationship between them using a sample of 29 galaxies[1]. These findings had a huge impact on the newborn extragalactic astronomy. Hubble not only discovered that the "spiral nebulae" were other galaxies, but also that they were consistently drifting away from us, leading to an expanding Universe.

This relationship, called nowadays as Hubble law, is the principal building block the modern observational cosmology. Hubble's law implications are so stable on the current scientific context that the distance of galaxies is very often only represented by their redshift, or z.

1.2 Modern surveys

The works of Hubble, from 1929 and later, turned surveys into a standard in astronomy. Data from surveys like the Palomar Observatory Sky Survey, which was published in 1958 and imaged more than $30,000$ $\deg^2$ in photographic plates during 9 years and are still used[2], changed our perspective of the astronomy from the analysis of single objects to a more statistical one.

[1] In those days the distance estimation to neighbor galaxies were limited to the ones that had stars with intrinsic luminosities that could be measured (mainly Cepheids and Novae) and were spatially resolved by the telescopes at that time.

[2] The Palomar Sky Survey has been digitalized and is available online as part of Digitized Sky Survey `https://archive.stsci.edu/dss/`

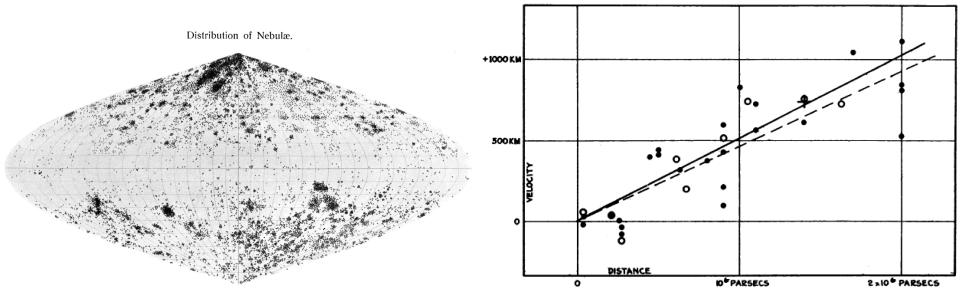

FIGURE 1.1 An overview of the Universe a century ago. In the left panel, we show a Galactic projection of how the Nebulae were distributed in the sky (from Charlier 1922), indicating a dearth of Nebulae in the central strip, known at the time as the "zone of avoidance". In right panel, we show the Hubble's diagram of distance versus radial velocity for galaxies, which lead to the discovery of the expansion of the Universe and the redshift-distance relationship (Hubble, 1929).

In the early 1990's charge coupled devices (CCDs) became widespread in astronomy. CCDs are more sensitive than the traditional photographic plates, they have a very high linearity (i.e., the number of electrons detected scales linearly with the number of photons that hit the detector), and the data come in a convenient digital format. This "CCD revolution" allowed the development of more ambitious projects like the 2dF Galaxy Redshift Survey (2dF) in the 1990's, the Six-degree-Field Galaxy Survey (6dF; in the southern hemisphere) and Sloan Digital Sky Survey (SDSS; in the northern hemisphere) in the 2000's, the Dark Energy Survey in the 2010's. They also paved the way for bigger projects that are being built, like the Large Synoptic Survey Telescope (LSST) which is expected to start in 2020 and the Javalambre Physics of the Accelerating Universe Astrophysical Survey (J-PAS) which starts observing with its full filter system next year.[3]

Since Hubble's discoveries, the fundamental property of galaxies is, undeniably, the redshift. Redshifts ubicate galaxies in the Universe, providing galaxy distribution maps which are essential to discover the nature of the matter in the Universe and how it is distributed. The galaxy distribution in the Universe is important to test cosmological models and, also, to provide the intrinsic luminosities of galaxies, which are necessary for the study of their baryonic content.

Optical galaxy surveys are usually divided into two observational strategies: spectroscopy and photometry. Spectroscopic surveys rely on selecting a sample of targets (usually using photometric colors) and directing their light into a dispersion element (generally a diffraction grat-

[3] Although there are many other surveys with different wavelength coverages, we dedicate this overview to the optical surveys which are the object of this thesis.

ing) which splits the light in its different wavelengths to be captured by a detector. The precision with which spectral features are measured by spectroscopy makes it the most accurate method to retrieve the redshift of galaxies. However, this accuracy comes at a price: the telescope time required to take a spectrum is much larger than that needed to obtain a broadband image. In spectroscopy the observed flux of the object is spread into many pixels of the detector, so the time necessary to reach the same signal-to-noise ratio of photometry is, of course, many times larger. Another caveat of spectrographs is that they are complex machines to build and their data calibration accompanies a more complex workflow when compared to photometry. On the other hand, photometric observations are faster and follow an usually straightforward data reduction scheme. With much less complex systems, photometric surveys are completed far more quickly with less time necessary for the instrument building and commissioning as well to execute the observations. The downside of traditional broadband photometry is that the redshifts derived from the data are usually inadequate to meet the precision needed for the various desired galaxy studies.

One thus faces a dilemma of either having very accurate redshifts with an expensive and time-consuming spectroscopic survey or a cheaper and faster, but less accurate one with broad-band photometry. Hickson et al. (1994) proposed an intermediate solution. By increasing the number of filters and decreasing their bandwidth a compromise between telescope time, spatial coverage and redshift accuracy can be reached[4]. This observational strategy provides data with reasonable redshift precision and fast spatial coverage. Some surveys that had this philosophy into their design include the UBC-NASA survey, (Hickson and Mulrooney, 1998) with 40 filters, the COMBO-17 survey with 17 (Wolf et al., 2003), COSMOS (Taniguchi et al., 2007), The ALHAMBRA survey (Moles et al., 2008) with 23 optical plus NIR filters and the J-PAS survey (Benítez et al., 2009a; Benitez et al., 2014) with 56 optical filters.

In the course of this thesis, three photometric surveys are studied. The ALHAMBRA survey, which provided the data for the evaluation of a method to recover physical properties of galaxies, the J-PAS survey which inspired the development of this method and will be the best place to use it on together with the S-PLUS Local Universe survey whose instrumental development is also part of this work. In the following sections, we introduce these three surveys, describing their observational details and provided data.

Field name	RA(J2000)	DEC(J2000)	E(B-V)
ALHAMBRA-1	00 29 46.0	+05 25 28	0.017
ALHAMBRA-2/DEEP2	02 28 32.0	+00 47 00	0.031
ALHAMBRA-3/SDSS	09 16 20.0	+46 02 20	0.015
ALHAMBRA-4/COSMOS	10 00 28.6	+02 12 21	0.018
ALHAMBRA-5/HDF-N	12 35 00.0	+61 57 00	0.011
ALHAMBRA-6/GROTH	14 16 38.0	+52 25 05	0.007
ALHAMBRA-7/ELAIS-N1	16 12 10.0	+54 30 00	0.005
ALHAMBRA-8/SDSS	23 45 50.0	+15 34 50	0.027

TABLE 1.1 The ALHAMBRA-Survey Fields. We include together with the name a reference to overlaps with other surveys of interest. Adapted from Moles et al. (2008).

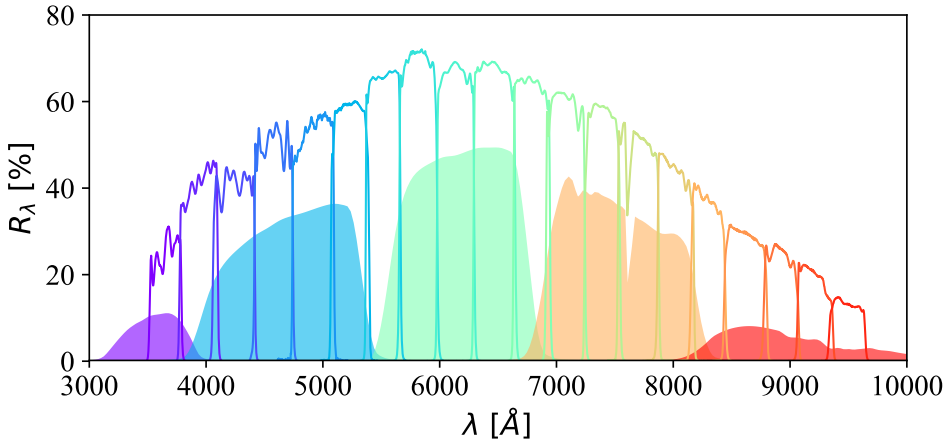

FIGURE 1.2 The 20 ALHAMBRA survey optical filter transmission curves plus the SDSS ugriz curves for comparison.

1.3 The ALHAMBRA survey

The ALHAMBRA (Advanced Large Homogeneous Area Medium Band Redshift Astronomical) survey (Moles et al., 2008) observed 2.79 sq. deg. of the northern sky with 20 contiguous and non-overlapping medium-band (300Å) filters covering the optical region of the spectrum (3500Å – 9700Å) plus J, H and Ks in the infrared. The instruments used in the observations where the Large Area Imager for Calar Alto (LAICA) in the optical and the Omega-2000 camera in the Near Infrared, both installed

[4]The reader is invited to read Benitez et al. (2014) for a more comprehensive view of the pros and cons between spectroscopic and medium and narrow band photometric surveys.

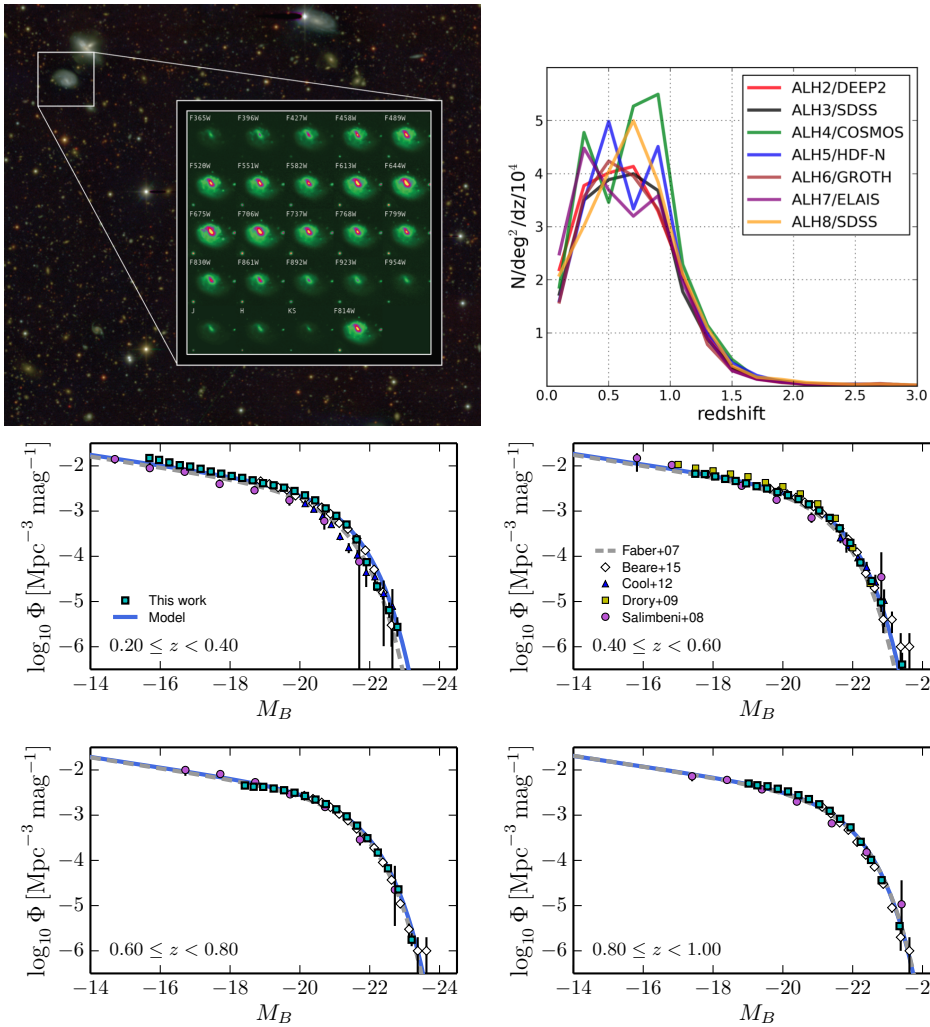

Examples of science done with the ALHAMBRA survey science. Top panels: left: an RGB composition of one ALHAMBRA field with the individual exposures of each of the 23 ALHAMBRA bands plus the synthetic F814*W* detection band in detail. Right: The galaxy redshift distribution for 7 ALHAMBRA pointings. Bottom panels: ALHAMBRA star-forming galaxies luminosity function. Images extracted from Molino et al. (2014) and López-Sanjuan et al. (2016).

FIGURE 1.3

in the primary focus of the Calar Alto 3.5m telescope.

The survey area is divided into 8 fields shown in Tab. 1.3, spread over different regions of the sky. The strategy of observing 8 non-contiguous fields in a very broad range of right ascensions maximizes the visibility of the fields throughout the year, minimizing the time to complete the survey. The areas were also chosen to overlap with other surveys such as SDSS, helping on the photometric calibration and maximizing the number of galaxies with measured spectroscopic redshifts in the field, essential to photometric redshifts, for calibration and precision determination purposes. The selection of 8 well-separated regions of the sky also comes in favor to minimize the cosmic variance. This cosmic variance effect can be seen on the right of Fig. 1.3, where the different fields often show structures due to galaxy clusters, the total survey distribution is therefore smoother.

The redshift precision of the ALHAMBRA survey was simulated by Benítez et al. (2009b). The expected precision before the begining of the survey was $\delta z/(1+z) \approx 0.014$ for galaxies with $m_I < 24$ mag. The final precision obtained by Molino et al. (2014) was $\delta z/(1+z) = 0.010$ for galaxies with $m_I < 22.5$ and $\delta z/(1+z) = 0.014$ for galaxies with $22.5 < m_I < 24.5$, in good agreement with the simulations. Molino et al. (2014) describes the ALHAMBRA data and its gold catalog, containing galaxies selected by their photometric redshift quality. The ALHAMBRA gold catalog corresponds to 98017 galaxies with absolute magnitude in the F814*W* filter in the $17 < m_{F814W} < 23$ and with redshift accuracy of $\delta z/(1+z) < 0.0012$ and single-peaked redshift probability distribution functions $p(z)$. This catalog will be used on the course of Chap. 4.

In Fig. 1.2 we show the optical filter transmission curves for the ALHAMBRA survey together with the SDSS in filled curves below for comparison. The near-IR filters are not shown as they will be not used for the work done on this thesis.

The main science goal of the ALHAMBRA survey is to detect and classify galaxies by its distances, broadening the knowledge of the galaxies distributions in the redshift space, collecting a homogeneous set of data, spread over different fields to minimize the cosmic variance. The results published by Molino et al. (2014) were an effort of 7 years to get the most reliable photometric redshifts out of this very informative dataset. In Fig. 1.3, we show examples of the science that can be done with ALHAMBRA's data. In the top row, left panel, we show an RGB composition of an ALHAMBRA field together with an example of a spatially resolved galaxy detailed with a "stamp" of its detection in each ALHAMBRA band in detail. In the right panel, we show the redshift galaxy distributions for the ALHAMBRA fields as measured by the photometric redshifts. In the following rows, we show the Bayesian star-forming galaxy luminosity function estimated by López-Sanjuan et al. (2016) in four different redshift bins and its comparison with other luminosity functions from literature.

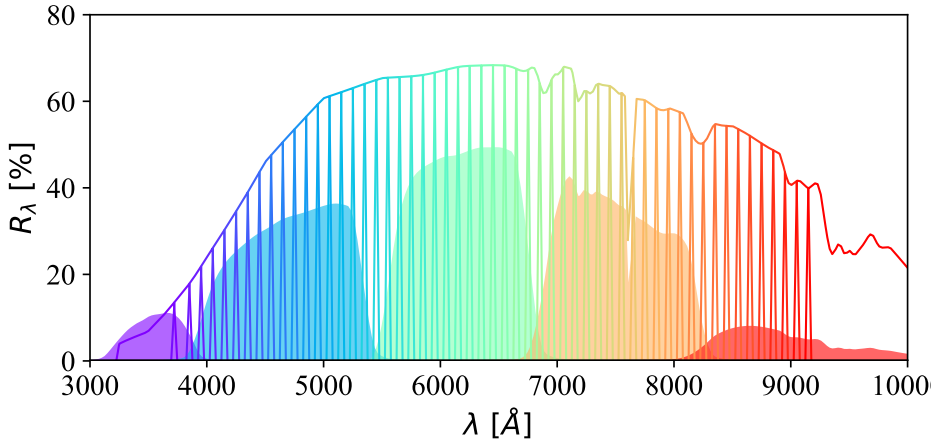

J-PAS filter transmission curves plus the SDSS ugriz curves for comparison. FIGURE 1.4

Left: JPAS 2.5m telescope installed at Pico del Buitre, in Javalambre Observatory. Right: JPCam, the JPAS camera, a 3D model showing the 14 CCDs and the cryogenic dewar. FIGURE 1.5

1.4 The J-PAS survey

The Javalambre Physics of the Accelerating Universe Astrophysical Survey (J-PAS) is the next generation of surveys like the ALHAMBRA survey. JPAS is a collaboration between Brazil and Spain which will map 80000 sq. deg. of the northern sky in 56 narrow-band filters ($\Delta\lambda \sim 145$Å) during the next 5 years. J-PAS survey will be carried out from a new facility built specially for it with two telescopes of large field-of-view (FoV) cameras. One with 86 cm of diameter and 2 deg^2 FoV, which will carry out the photometric calibrations of the survey and the 2.5 m diameter main telescope with a 4.7 deg^2 FoV and a 1.2 Gigapixel camera which will map the sky (both shown in Fig. 1.5). This system will provide a unique all-sky low spectral resolution IFU for objects of i-band

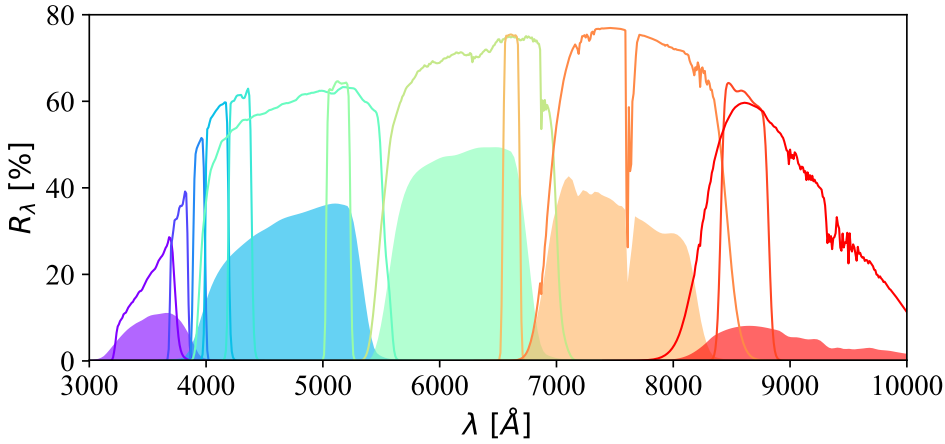

FIGURE 1.6 S-PLUS filter curves with the SDSS ugriz curves for comparison.

magnitudes up to $m_i \sim 24$.

The J-PAS survey comes into the philosophy described in §1.2 that multiple medium and narrow-band filters are more efficient redshift estimation machines. J-PAS is expected to observe 9×10^7 red galaxies with a photo-z precision of 0.3 %. Also, it will observe 7×10^5 galaxy clusters and groups (Benitez et al., 2014). Its multiplexing capability, i.e. the number of objects that can be observable at the same time by a telescope with a given field of view, will be of ~ 4000, four times better than the current spectroscopic projects.

In Fig. 1.4 we show the 56 J-PAS filter curves. Separated by 100 Å each, they have an overlap of $\sim$ 25Å as a result of a compromise between the planned photometric redshift precision with the most modern narrow-band filter design technology available.

In Fig. 1.5 we show a picture of the telescope installed in the Javalambre mountains together with the final mechanical model of the JPCam, indicating the disposition of the 14 CCDs that compose the instrument. This thesis was inspired by the data that are starting to be collected this year in the J-PAS survey as well as the ancillary data obtained with the smaller telescope (the T80) and especially its southern twin, the T80S.

1.5 The S-PLUS survey

The Southern Photometric Local Universe Survey (S-PLUS) project is the local Universe survey for which the T80S telescope, described in chapter 2, was designed. It is divided on 5 sub-surveys, each one will try to constrain a different aspect of the local Universe. In Fig. 1.6 we show the

filter curves for the S-PLUS filters, listed in Tab. 1.5. They were optimized to detect stellar features in the Galaxy and the Local Universe. In chapter 2 we describe in detail the project and installation of the T80S telescope.

Table 1.5 resumes the S-PLUS sub-surveys. The main survey will map 8000 deg^2 of the southern sky in the 12 filters installed in the T80SCam instrument. The filters are shown in Fig. 1.6 with a resume of their characteristics and the exposure times listed in Tab. 1.5.

Other 4 surveys will be conducted in parallel with the main survey, getting out the most of the available telescope time and in all different sky conditions. The ultra-short exposure survey will, concurrently with the main survey, take short exposures of 1s and 5s in 8 filters (u, g, r, i, z, F395, F410 and F430) to create a map of bright low metallicity and carbon-rich blue horizontal branch stars. The low cadence survey will regularly observe 1500 deg^2, mostly in non-photometric nights, in three filters (r, i and Hα) for the search of transients like variable stars, SNe, and asteroids. It will be the unique survey in the southern hemisphere which will observe for Hα variability. The high cadence survey will target 20 fields every 4–5 days, also using non-photometric nights, looking for SNe discovery, asteroids characterization and quasar variability studies.

S-PLUS will also map further 1500 deg^2 of the Galactic Plane and Bulge. The so-called Galactic survey will map Milky Way's bulge and disk in the 12 filters and will look for classification of the stars in the Galactic Plane, the discovery of pulsating white dwarfs and synergies with other Galactic Plane surveys like the VVV survey (Minniti et al., 2010).

The S-PLUS survey began observations at the beginning of 2017 and will run the observations (for the main survey) for the next 3 years. A preliminary RGB composition showing a field of the S-PLUS survey is presented in the next chapter, in Fig. 2.7.

1.6 This work

This thesis is dedicated to studying the current surveys in two different perspectives. In Chap. 2 we describe the development of a new facility, devoted to surveys of the local Universe, the T80S telescope and its instrument. As discussed in 1.5, four different surveys will map different regions of the sky in 12 filters. We detail the installation of the telescope, the software developed to automate it and the commissioning of the instrument.

On the other hand, we show an application to the data generated by these photometric surveys and photometric redshift codes in Chap. 3. We explain how we can obtain stellar physical properties, such stellar masses of galaxies, out of the photometry of galaxies. Then, in Chap. 4, we show how these stellar masses can be used to derive the ALHAMBRA survey stellar mass function.

Filter Name	λ_{eff} [Å]	$\Delta\lambda$ [Å]	Total t_{exp} [s]	Comment
u	3536	680	681	Javalambre u-band
F378	3733	230	660	[O II]
F395	3941	160	354	Ca H+K
F410	4095	300	177	Hδ
F430	4293	320	171	G-band
g	4780	1770	99	sloan-like g
F515	5134	280	183	Mgb Triplet
r	6267	1840	120	sloan-like r
F660	6614	220	870	Hα
i	7684	2130	138	sloan-like i
F861	8608	610	240	Ca Triplet
z	8956	2760	168	sloan-like z

TABLE 1.2 Summary of S-PLUS filters sorted by their central wavelength

S-PLUS sub-surveys

Survey	area	visits cadence	filters	exposure times	photometric quality
Main (S-PLUS) *Local Universe*	Southern region: 4230 deg^2	1	ALL	Tab. 1.5	photometric $0.7'' - 1.5''$
	Northern region: 1946 deg^2				
Ultra-short *Low metallicity and Carbon-rich stars*		1	U, G, R, I, Z F395, F410, F430	1s and 5s	same as Main
Low cadence *variable stars*	1500 deg^2	2 weeks	G, R, I and H_α	3× 20, 30, 30 and 290s	non-photometric
High cadence	40 deg^2	4 − 5 days			non-photometric
Galactic	Bulge: 400 deg^2	1^{st}	ALL	Tab. 1.5	photometric
	$350 < l < 10$ & $-15 < b < 5$	2^{nd}	″	1s	″
	Disk: 1020 deg^2	3^{rd}	″	5s	″
	$220 < l < 280$ & $-15 < b < 5$	4^{th} to 25^{th}	R, I, H_α	Tab. 1.5	non-photometric

Chapter Two

T80S: The S-PLUS telescope

This chapter is dedicated to the description of the T80S telescope and its instrument, the T80SCam. The T80S is an 80 cm telescope installed at Cerro Tololo Inter-American Observatory, in Northern Chile. With a large field of view, T80S is designed to survey the southern sky in 12 *optical filters as part of the S-PLUS survey. Also, it will be able to conduct an all-sky survey in the Johnson filters plus a polarimeter with the S-POL project.*

2.1 T80S installations

The T80-South telescope (T80S) is a new facility situated near the summit of Cerro Tololo in central Chile, at an altitude of 2,207 m, at latitude -30:10:10.78 and longitude -70:48:23.49 (Mamajek, 2012). Built by a partnership between two Brazilian institutions, the Fundação de Am-

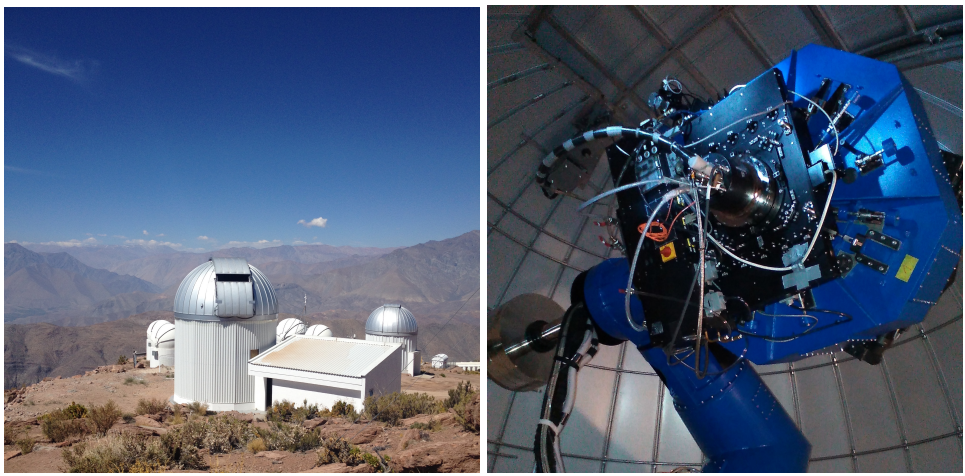

Figure 2.1 Left: T80S buildings. Telescope building on the left, control and computer room in the right (square) building. Right: T80S Telescope (blue parts) with the instrument (black parts) mounted on it.

paro à Pesquisa do Estado de São Paulo and the Observatório Nacional, it is installed on a small building with the dome, a small data center for data processing and two auxiliary rooms for instrument engineering purposes. The operation of the telescope is fully automated, and it is controlled by the `chimera` observatory control system (OCS) developed by the Federal University of Santa Catarina, the Federal University of Sergipe together with Instituto de Astrofísica de Andalucía. Details about `chimera` are described in §2.6.

In Fig. 2.1, we show a panoramic view of the site. In the right panel, we show the two buildings of T80S. The left building has two floors: in the 1^{st} floor is the technical room where tools are stored, and the instruments are handled while in the 2^{nd} floor the telescope (right panel) is installed. The right building hosts a small control room and a technical room where a small data center (described in §2.5) shares space with the camera cabinet and a water chiller used to cool the electronics in the warm parts of the instrument. In the right panel, we show a picture of the telescope (blue parts) with the instrument mounted on it (black parts). Detailed drawings of the two T80S buildings are shown in Appendix B.

2.2 Telescope

The T80S telescope is a new generation of small focal ratio Ritchey-Chretien Cassegrain telescopes with a field of view (FoV) of 2 square degrees. Such large FoVs are crucial to conducting astronomical surveys as they allow the coverage of large areas on the sky with fewer exposures, allowing for a much shorter survey completion time. The telescope design was done by Advanced Mechanical and Optical Systems (AMOS) in Liège, Belgium with the mechanical fabrication, assembly and control systems subcontracted to the German company ASTELCO Systems GmbH in Munich. The telescope is housed inside a 6m ASH dome[1], controlled by an ACE[2] SmartDome controller and its telescope control is done via a private protocol called OpenTPL developed by Tau-Tec GmbH. More details on the control of the telescope are explained in §2.6.

The telescope supports instruments of up to 75 kg, and its slewing speed is of 4 deg/sec with an acceleration of 1 deg/sec^2 with the full payload. This very fast speed, combined with its large FoV, makes T80S very competitive to react automatically to ultra-short events such as gamma ray bursts, even with the large GRB pointing error bars such as those of the INTEGRAL satellite (Gorosabel et al., 2014). T80S's pointing accuracy specifications are of < 10 arcsec RMS and the tracking accuracy specification is of 0.5 arcsec RMS over 15 sec, 0.5 arcsec RMS over 5

[1] `http://www.ashdome.com/`
[2] `http://www.astronomical.com/`

Optical specifications	
Configuration	Ritchey-Chrétien
Aperture	826 mm diameter
System F ratio	F/4.3
Plate scale	55.58 arcsec/mm
Focal length	3712 mm
Field of view	110 mm (1.7 deg)
Coma-free point	291.36 mm
Primary Mirror (M1)	
Curvature radius	-2471.295mm concave
Conic constant	-1.163946
Optical Diameter	826 mm
Central hole	349 mm
Effective collecting area	0.44m^2
Secondary F/4.5 mirror (M2)	
Distance from Primary	825.7695 mm
Radius of curvature	-1237.411 mm convex
Conic constant	-5.776745
Optical Diameter	302.879 mm

TABLE 2.1 T80S telescope optical specifications

min and 10 arcsec RMS over 60 min periods. In table 2.2 we summarize the telescope optics parameters. The FoV in full performance, i.e. no vignetting, is reduced from 2 deg^2 to 1.7 deg^2.

2.3 Instrument

The T80S telescope has only one instrument: the T80SCam. The instrument has two modes: photometry and polarimetry, which are not automatically interchangeable during an observing night. In both photometric and polarimetric mode, T80SCam uses a Spectral Instruments 1100S camera equipped with an E2V 290-99-1-F24 CCD (serial number 11323-24-01). This camera is mounted on the focal plane with a filter and shutter control unit (FSU) between it and the telescope flange as shown in Fig. 2.2, composing the T80SCam instrument altogether. The FSU is formed of a custom-made shutter by Bonn Shutters and two filter wheels[3]. The shutter is rated for a minimum exposure time of 1 ms with an RMS error of 300µs.

[3]The T80SCam, when converted to polarimetry mode, hosts four wheels for the filters, polarizers, and calibrators

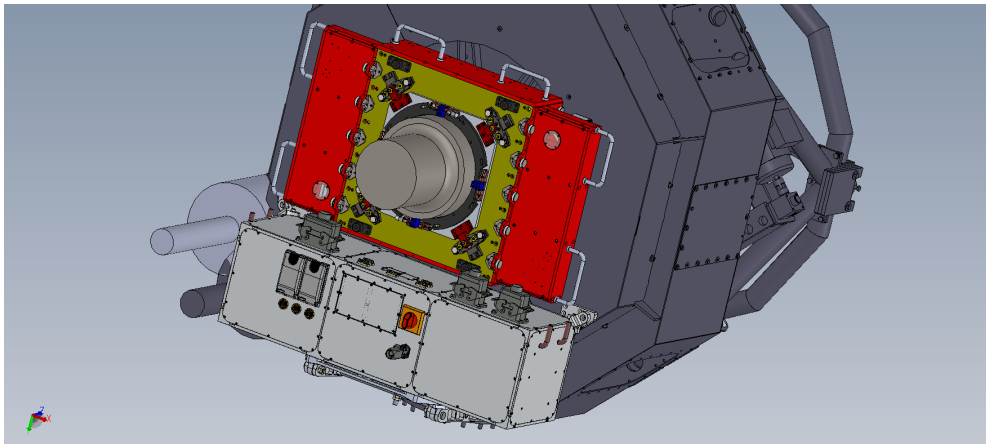

FIGURE 2.2 3D model of the T80S optical tube assembly with T80SCam mounted on it. In dark gray is shown the OTA, in light gray the FSU computer and PLCs enclosure, in red the FSU and, attached to the FSU, in medium-gray the camera dewar.

The camera hosts a CCD array of 9232×9216 pixels of $9\mu m$, giving a practical FoV of 1.4×1.4 deg^2 and a pixel scale of 0.55 arcseconds per pixel. The CCD is divided into 16 amplifiers with 16 possible readout speeds from 100 kHz to 1.01 MHz whose gains and readout noises are listed in Appendix C.

The mechanical part of the FSU was designed at Instituto de Pesquisas Espaciais by René Laporte, in Brazil, and produced by MetalCard. The control of the FSU was developed by another Brazilian company, Solunia, using Programable Logic Controllers (PLCs) from Beckhoff. Its control is done over ethernet using the ADS Beckhoff proprietary protocol. In Fig. 2.2 we show a 3D model of the instrument installed on the telescope with its different parts marked in different colors: dark gray for the telescope's optical tube assembly (OTA), in light gray the FSU computer and PLCs enclosure, in red the FSU and, attached to the FSU, in medium-gray the camera. In Fig. 2.3 we show in the left panel a picture of one of the two photometric filter wheels and, in the right panel, a photo of the camera dewar seen from the entrance window, with the CCD shown.

In the photometric mode, the FSU counts with two filter wheels with seven positions each (6 filters plus one clear) and a guiding camera is installed at the border of the focal plane. The auto-guider is a Prosilica GT2300C camera controlled via ethernet with a 12.85×9.64 mm detector which, translated to the T80S plate scale (Tab. 2.2), is equivalent to a field of view of 11.8×8.96 arcmin. It has a magnitude limit of $m_V = 15$ for exposures of 1 second and a signal-to-noise ratio of $S/N = 20$. In the

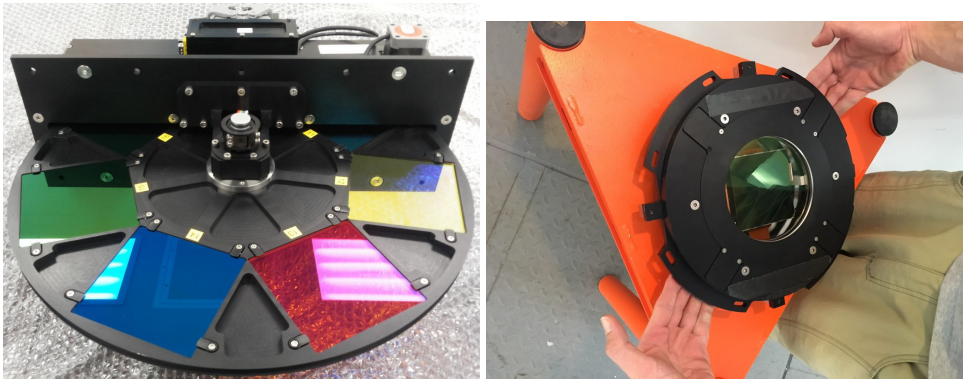

FIGURE 2.3 Left: One of the T80SCam filter wheels with the filters mounted on it. It represents one of the two wheels marked in red in Fig. 2.2. Right: A picture of the camera showing the CCD before being mounted on the telescope.

polarimetric mode, the FSU does not have the auto guiding option and counts with three filter wheels: a filter wheel (for the Johnson filters), an analyzer wheel, a calibration polarizer wheel and a wave plate. An extended description of the polarimeter mode of the T80SCam will be available in (Magalhães et al., in prep.).

2.4 Enviroment monitoring

The adequate environment monitoring is an important task in any observatory. In a robotic telescope as T80S, this duty is even more important to assure proper housekeeping of the observatory and quality of the data produced. Being T80S situated in a mountain with dozens of other telescopes, there is a vast set of environmental information available to feed into the observational decision algorithms and extract the most of the available observing time. In T80S operations, we divide the information available in two different categories: weather information, which stands for the local climate conditions like humidity and wind speed (described in §2.4.1), and astronomical conditions information, which stands for more astronomical related parameters such as seeing and sky extinction (described in §2.4.2).

The T80S OCS is designed to have multiple redundant instruments, reducing downtime in case of failures. In the event of an environment instrument, i.e., an anemometer, failure, the next on the priority list is used as the source of information to the observatory.

2.4.1 Weather

The site weather conditions are collected by three redundant weather stations: the T80S weather station, the LCOGT weather station, and the Blanco 4m telescope weather station. At any time new weather stations can be easily added.

The T80S weather station is installed on top of a radio tower close to the T80S building and provides measurements of temperature, humidity, wind speed and pressure from a commercial weather station model Vaisala WXT520 weather transmitter. Also, there is a sky transparency factor (from 0% to 100%) that is estimated from the difference between the ambient temperature and the sky temperature measured by near infrared (5.5 to 14μm) radiation sensor. This sensor is also provided by a commercial sky transparency monitor AAG Cloud watcher[4].

The LCOGT weather station, by its proximity, is the second weather station that is used in case the T80S weather station fails. It provides measurements of temperature, humidity, pressure, wind speed and also a sky transparency coefficient from 0% to 100%. The weather data is crawled by a chimera plugin `chimera-ctioenvironment`[5] from the LCOGT TelOps page[6] and made available as a chimera weather station.

The weather station located on the 4m Blanco telescope is the last station the OCS takes into account on deciding whether closing the dome or not. Its data are also provided by `chimera-ctioenviroment` module via the CTIO weather MySQL database providing temperature, humidity, pressure, wind speed and, more importantly, real-time seeing measurements whose importance is discussed in the next section.

2.4.2 Astronomical conditions

Two principal astronomical conditions are now measured at CTIO and will be used as variables for observing strategy decision: seeing and extinction. Seeing quantifies the turbulence caused by Earth's atmosphere, measured by the Full Width at Half Maximum (FWHM) of the point spread function (PSF) and extinction is measured by the linear coefficient of the fit of a straight line to the instrumental magnitudes over different airmasses.

The seeing quality is measured in real time by two different sources: the Tololo's MASS-DIMM (Tokovinin et al., 2003; Tokovinin and Kornilov, 2007) seeing monitor and the chimera quality control (`chimera-qc`) plugin (see §2.6 for more details about the observatory plugins). This information can be used to adjust the observing strategy according to the night astronomical conditions.

[4] `http://www.lunatico.es/ourproducts/aag-cloud-watcher.html`
[5] `https://github.com/astroufsc/chimera-ctioenviroment`
[6] `https://telops.lco.global/`

The Tololo's MASS-DIMM provides real time seeing information, which is compared, also in real time, with the average FWHM of the stars as measured by the chimera quality control (`chimera-qc`) plugin.

The extinction coefficients are measured by observing standard stars in different air masses throughout the night. The extinction coefficients derived from this method are the night average and still not integrated to the observing strategy algorithm §1.5. The alternatives to supply this information to the system in real time is to use data of either one of the all-sky cameras available in the mountain like the method proposed by Duriscoe et al. (2007) for the calculation of the extinction using the Tololo All Sky Camera or, alternatively, use the data from the aTmCam transparency monitor (Li et al., 2014), installed near the Blanco 4m telescope. Both methods for accurate sky transparency assessment are being studied and will be implemented into the observatory observing decision algorithm shortly.

2.4.3 Operational limits

The defined operational limits of T80S are listed below. If the operational limits are above the threshold, all operations are stopped, and the telescope is closed.

- Sky Transparency: Should be higher than 35%. If transparency gets lower than this limit, the site is locked until it stays more than 40% for 15 minutes.
- Humidity: Should be less than 85%. If humidity reaches this level, it should be under 70% for 30 minutes to unlock the dome.
- Dew point: Should be less than 3°C lower than the ambient temperature. If dew point reaches this level, it should be less than 5°C lower than the ambient temperature for 30 minutes to unlock the dome and restart observations.
- Wind Speed: Should be less than 16 m/s. If it reaches this level, it should it should be less than 13 m/s for 1 hour to unlock the dome and restart observations.

The observatory dome is open 2 hours before sunset to reduce the temperature difference between M1 and M2. A couple 2 hp fans extract air from inside the dome before the observations start. A 3^{rd}, smaller fan, blows air directly into M1 if its temperature is higher than ambient temperature. This procedure has proved efficient to stabilize M1 temperature around 2°C greater than M2 during the entire night.

Following this procedure, the optics keeps stable throughout the night, without the need for a costly and maintenance intensive air-conditioning system.

This procedure provides stable optics without requiring an air-conditioning system, which has a high acquisition and maintenance costs.

2.5 Data center

The T80S data center is designed to store the raw data from the observations and to have the computing power to reduce the data produced by the instrument in real time. It is located in the technical room, shown in the plant in Appendix B. The technical room is refrigerated by three air conditioning units mounted downwind to minimize any turbulence that may degrade seeing quality.

Running the pipeline every morning has several advantages. The information extracted from the reduced data can be used by the survey scheduling algorithm to decide whether or not to re-observe some or all of the previous night's fields. Owing to bandwidth limitations, only the reduced data can be transferred to the research institutions; thus, after reduction, the reduced images can be immediately transferred. Also, due to the limited bandwidth in Cerro Tololo, only the reduced data is transferred out of the observatory, and the raw data transferred by tapes as a mere backup. As a safety measure, all the raw survey data is backed up on magnetic tapes and regularly sent by mail to the T80S team at IAG/USP.

The data center counts with one router and one switch for network communications together with five servers: three application servers (APP), one camera server (CAM) and one storage server (STO). The APP servers run VMWare[7] vSphere Hypervisor as the operational system and the virtual machines are administered by a vSphere six solution, also from VMWare. The storage server runs on FreeNAS, an open source operating system designed for network attached storage appliances. The total storage capacity in the site is 40TB. The only non-virtualized operating system present in the observatory is the Windows Server 2012 which runs in the camera acquisition control server.

The main advantage of designing the observatory infrastructure from scratch, as we did in T80S, is that we could select all the hardware to be IP-manageable, so everything is connected via a network switch and has an IP address associated with it. This connectivity, related to the fact of all operating systems are virtual, makes hardware failures quickly fixed and eliminates the need for local intervention for switching main equipment to spare. Another advantage of having this fully virtualized environment is that software integration tests can be done in parallel, on a development virtual machine which is a simple clone of the production virtual machine. This arrangement speeds up the software development and integration tasks and minimizes downtime due to engineering works.

[7] `https://www.vmware.com`

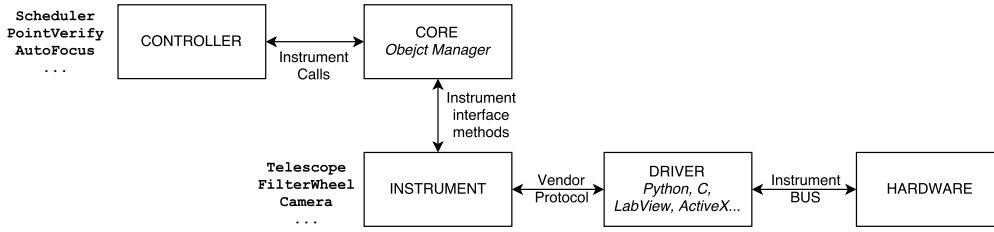

FIGURE 2.4 Chimera software diagram. Manager publishes methods of the chimera instruments which are available to the controllers.

2.6 Chimera: The T80S OCS

The T80S telescope operation is fully automated and controlled by the observatory control system (OCS) `chimera`[8] (Silva et al., 2017). Designed to be fully-distributed, modular and portable, `chimera` is developed in Python and uses Python Remote Objects[9] as the technology to distribute objects across different computers and operational systems. As its dependencies are very few, chimera has the advantage to run on many operating systems flavors such Windows, Linux, Mac OS and even Android, letting the implementations be easily ported from one architecture to another, facilitating the inclusion of new hardware. Portability and free access are the most prominent characteristics when we discuss observatory control systems, but in most observatories, we see that proprietary and hardware-specific software are still the standards.

Chimera is designed to isolate the instruments in an observatory from the modules which they control, so replacing a camera, a dome and even a telescope is an entirely transparent task due to its three abstraction layers: core, controllers, and instruments. These three layers are designed so the controllers are hardware-agnostic and can be used in any observatory with any instrument.

In Fig. 2.4 we show a simplified diagram of how `chimera` works. At its core, there is an entity called manager which publishes `Instrument` objects in the network. These objects are consumed by other objects, like the `Controller` objects. `Instrument` objects translates the vendor methods to standardized `chimera` interfaces. The system is very flexible, so the access between `Instruments` and `Controllers` are unrestricted. For example, a `Dome` object can access `Telescope` which is also a `Instrument` object to query its position and stay in sync.

The chimera layers are:

- Core: The core of chimera holds all methods common to all chimera modules such as low-end communication methods to translate PYRO

[8] `http://github.com/astroufsc/chimera/`
[9] `http://www.pythonhosted.org/Pyro/`

objects into chimera objects and basic astronomical-related methods like coordinate conversions and file name creation and events control.

- Instruments are the interfaces to the hardware, defining a standard set of methods for each observatory instrument. With this approach, every instrument has a common interface with methods and events, being some mandatory and some optional. For example, any `Camera` object has the mandatory method `expose`, but not `startFan`, which is implemented only if the camera has a controllable fan.

- Drivers do the bridge between the instruments and the vendor communication libraries and protocols. They expose the hardware regarding methods that can be used by the instruments.

- Controllers are the high-level interfaces operating on the instruments through their standard methods to do all the tasks to an astronomical observatory. These high-level tasks include, for example, focusing the telescope, checking telescope pointing and coordinating an observation schedule.

An example of how `chimera` objects can be easily imported and used in Python is shown in Appendix D, where we show a simple example of getting proxies for the `Telescope` and `Camera` objects of a fake observatory and use them to point to an object, expose and show the image.

2.7 T80S chimera plugins

This section is dedicated to explaining the chimera modules that make the T80S telescope work as a complete robotic facility. It is divided into two subsections: Controllers and Instrument Drivers. The controllers do the high-level tasks such as weather control, scientific and calibration images acquisition, optics alignment, and others. The instrument drivers are the interface between the high-level instruments abstraction to the low-level vendor protocols. The controllers and instruments shown here are the ones used in the T80S integration, being only a fraction of the 40 chimera plugins available in `chimera`'s repositories[10].

2.7.1 Controllers

2.7.1.1 chimera-autoalign

A large FoV telescope as T80S comes with some caveats. One of them is that the optics must have an active control to assure that the quality of the images is maintained. The optical corrections are done by a hexapod

[10] `https://github.com/astroufsc`

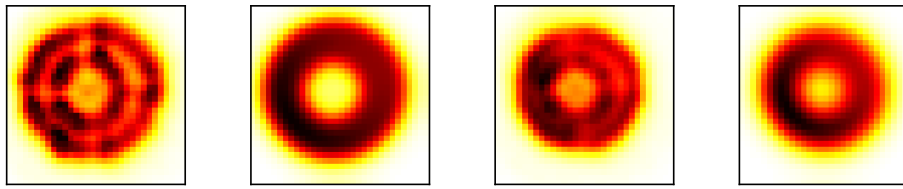

FIGURE 2.5 Two donut fit examples. For each image pair, the left panel shows the image obtained by the telescope of a defocused star and the right panel shows its fit as done by donut algorithm.

where the secondary mirror (M2) is mounted. The hexapod gives the capability of moving the M2 in 6 degrees of freedom: X, Y, Z, U, V and W, enabling active corrections in the optics alignment so, primary and secondary mirrors and camera are fully aligned in all observations.

The chimera-autoalign plugin uses the "donut" algorithm, created by Tokovinin and Heathcote (2006) to find the correct alignment of the telescope optics by fitting Zernike Polynomials Zernike (1934) to defocused images.

In Fig. 2.5 we show an example of Zernike coefficients fit done by `chimera-autoalign` plugin. The telescope is defocused, and an exposure of a stellar field is taken. The stars on the are detected by the SExtractor software and stamps of the star "donuts" are made. The stamps are fitted in parallel, and the Zernike coefficients for the telescope optics are calculated. From the coefficients obtained, an optical correction is applied by changing telescope's Hexapod position. The algorithm is run repeatdely until it reaches convergence. It usually does not take more than three interactions to reach convergence.

Source code: `https://github.com/astroufsc/chimera-autoalign` and `https://github.com/astroufsc/donut`

2.7.1.2 chimera-pverify

The `chimera-pverify` plugin is developed to automate the task of telescope pointing assessment. With the telescope pointed to a field, it compares the position given by the telescope from its encoders with the astrometric solution obtained with the `astrometry.net` (Lang et al., 2010) software from an image taken at this field. If the center of the field calculated by `astrometry.net` is not within a configured tolerance, offsets are applied in the position of the telescope, re-centering it, and the process is repeated until the difference in right ascension α and declination δ are within the tolerance.

This module is particularly useful for a precise mount model esti-

mation. A pointing list can be loaded into `chimera-pverify` and it observes them returning a table with the telescope encoder positions (α, δ) and the effective positions, obtained by the astrometric solution (α', δ'). These offsets are used as input data points to fit the telescope vendor mount model like, for example, the TPoint[11] software model.

Source code: `https://github.com/astroufsc/chimera-pverify`

2.7.1.3 chimera-skyflats

For wide field telescopes, as T80S (f/4.31), dome flats are non-uniform. A decent and uniform flat screen for those systems can be expensive and suffer inside-dome space limitations (Rheault et al., 2010). For that reason, taking flats using the twilight illumination is the most straightforward and, sometimes, the only solution. As shown by Chromey and Hasselbacher (1996) the sky gradients are minimal at the zenith, and the sky total flux decreases exponentially with the sun's altitude.

For the automated sky flats on T80S [12] we took a set of "manual" sky flats and measured the average counts per second of exposure time versus the sun altitude, then we fitted a simple exponential function:

$$N = A * e^{B*\alpha} + C \tag{2.1}$$

where N is count number per second, α is the sun's altitude and A, B and C are the fitted parameters which are stored in a `json` file for the automatic exposure time calculation.

Fig. 2.6 shows two examples of the exponential fit for the twilight flats taken in the T80S telescope. The left panel shows filter G and F430 in the right. Both dawn and dusk flats are taken into account for the exponential fit as we did not see a substantial difference between the sky brightness in the two periods. Each black point represents the average of the counts per second of one flat image versus the sun altitude. To optimize the sky flat acquisition, the less sensitive filters are taken when the sun is higher, then next the more sensitive ones are taken.

We briefly checked the gradients in the sky flats, and we found that the illumination of the CCD measured only by sky flats varies with the position of the sun on the horizon. These gradients turn sky flats useful only for high-frequency corrections, i.e. pixel-to-pixel, while the low-frequency, i.e. the global illumination, corrections should be done with another method. The proposed method is to use "photometric flats", which method was described by Manfroid (1995) and implies into the observation of a dense stellar field varying the position of the telescope in a grid of 20 – 30 different positions and fitting the illumination cor-

[11] `http://www.tpointsw.uk/`

[12] In practice, the sky flat algorithm implemented for T80S can be used in any telescope only by changing exponential parameters by the ones measured to the desired telescope, CCD and filter combination.

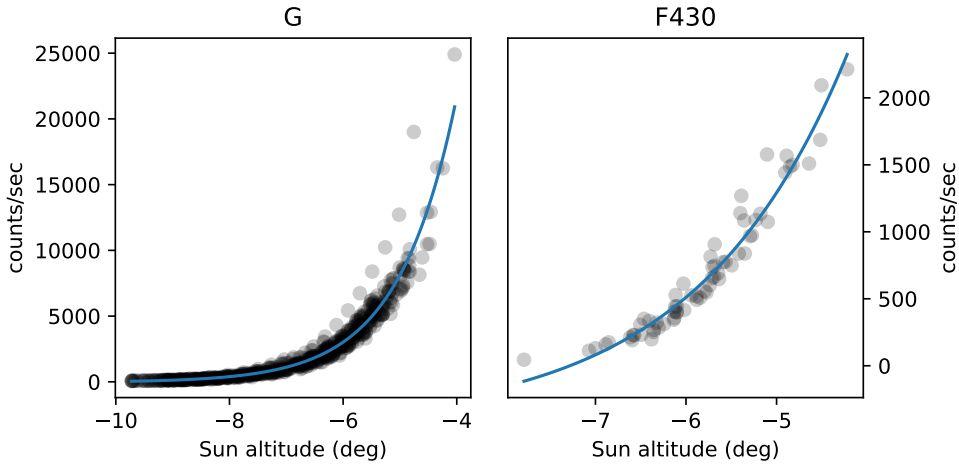

FIGURE 2.6 Example of chimera-sky flat fit for the broad-band filter G in the left panel and the narrow-band filter F430 in the right. Each black dot represents a sky flat from T80S, and the blue line is the exponential fit to the data points.

rection by comparing the instrumental magnitudes of the stars in the various pointing positions.

Source code: `https://github.com/astroufsc/chimera-skyflat`

2.7.1.4 chimera-supervisor

`chimera-supervisor` is a plug-in dedicated to managing the daily observatory activities. It plays the role of a night assistant of a classical, i.e. non-robotic, observatory. It is responsible for running pre-programmed actions, lock and unlocks observatory instruments according to the rules defined in a `yaml` file and loaded into a database. The rules may include the weather conditions where the dome and site can work as, for example, described in §2.4.3 and also operational actions like dome and telescope cover opening at the beginning of the night and closing at the end of it. It is also responsible for: running calibration scripts to take bias, dome and sky-flat calibration images; controlling mirror temperatures; turning fans on or off when necessary; and loading observation scripts into the scheduler.

`chimera-supervisor` also connects to all the instruments in the observatory and, if there is any untreated exception, human intervention is called via Telegram[13] messages.

Source code: `https://github.com/astroufsc/chimera-supervisor`

[13] https://telegram.org

2.7.2 Instrument drivers

In this section, we briefly list the instrument drivers designed to run the operations in T80S. As discussed in §2.5, all devices in the observatory have an Ethernet interface, enabling their configuration from any computer in the network.

- AAG Cloud Watcher: Controlled by, the `chimera-aagcloudwatcher`, the AAG Cloud Watcher measures the Sky Transparency by the difference between the ambient temperature and the sky temperature, measured by an infra-red temperature sensor, as described in §2.4.1. **Source code:** `https://github.com/astroufsc/chimera-aagcloudwatcher`
- ASTELCO telescope: T80S telescope and dome are controlled by the `chimera-astelco` module over the OpenTPL vendor proprietary protocol. It was tested for the T80S (NTM-1000) mount, should work for other telescope mounts of ASTELCO with minor or no modifications. **Source code:** `https://github.com/astroufsc/chimera-astelco`
- Emmerson Commander SK: The two extractor fans installed in the T80S dome are controlled by two Emmerson Commander SK frequency drivers who are accessible via Modbus/TCP protocol. Fan controls include power on and off and speed control. **Source code:** `https://github.com/astroufsc/chimera-commandersk`
- T80 Camera: The T80Cam, described in §2.3, is controlled by the `chimera-t80cam` module. It controls the camera exposure times its parameters as well the FSU in both photometric and polarimetric mode. **Source code:** `https://github.com/astroufsc/chimera-t80cam`
- Vaisala WXT520 weather transmitter: Temperature, humidity, pressure and wind speed are measured by a commercial weather station and fed into the OCS by this module. **Source code:** `https://github.com/astroufsc/chimera-vaisala`
- Flat lamps, fans, and other miscellaneous switchable appliances are controlled by `chimera` through a Schneider Electric Advantys OTB (model OTB1E0DM9LP) Ethernet network I/O module. **Source code:** `https://github.com/astroufsc/chimera-schneiderotb`

2.8 Project status and future

T80S was installed in November of 2014, and the observatory equipment was fully installed and commissioned during 2015 and 2016. During the equipment installation, `chimera` was improved and many bug fixes were done making it very reliable. Instruments were separated from the core of the `chimera` package, improving a lot the speed of the software development through plugins.

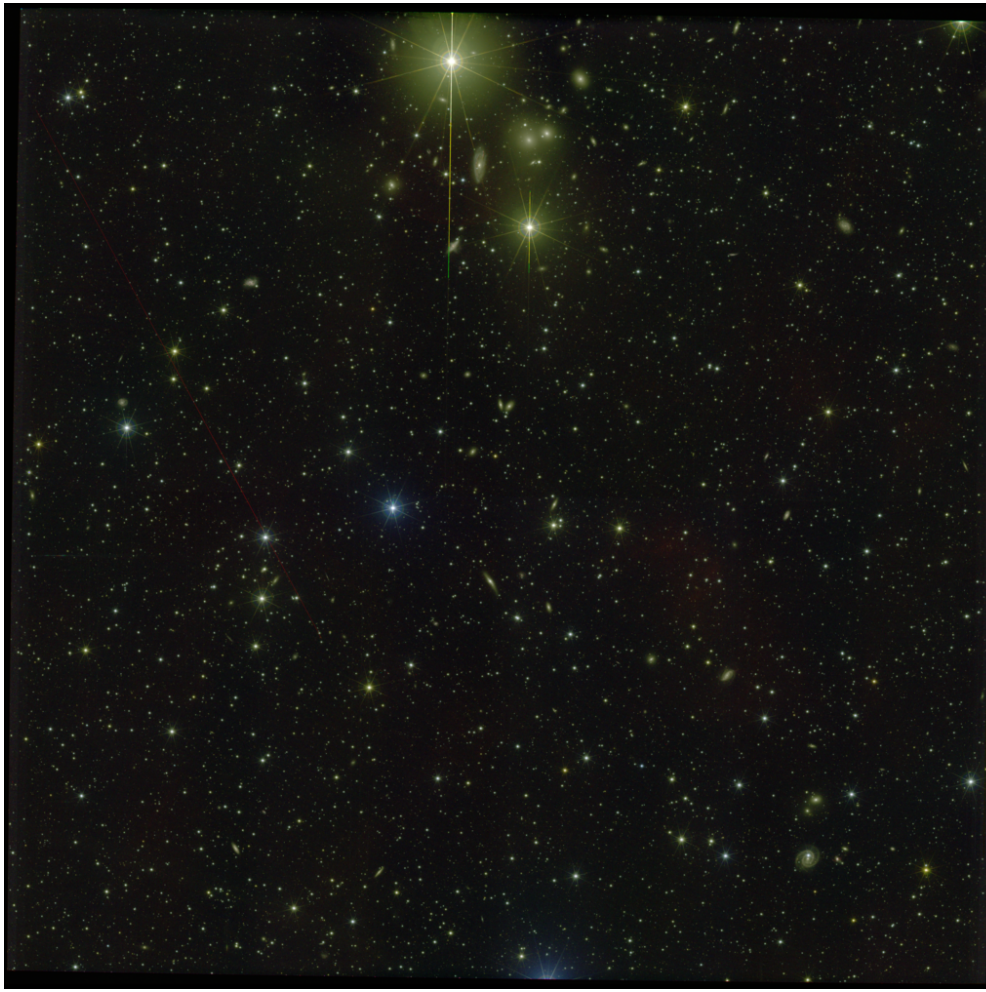

FIGURE 2.7 An example of the field of view of one T80S image. Red, Green and Blue colors are F660, R and G filters, respectively. Composite image made with trilogy software (Coe et al., 2012).

Since the telescope and its instrument was a joint project and the instrument had several issues before being able to be installed in the telescope, counterweights and a flange were designed to connect a small SBIG ST8 camera and make the commissioning of the telescope mount. The telescope mount was quickly commissioned and parameters, like pointing and tracking accuracy, were within the specifications.

On the other hand, the instrument commissioning took a bit longer than expected, almost a year. Since the camera was a new project of Spectral Instruments, faced several electronics problems when on Chile and had to be sent three times back to the USA to projects adjustments like changing capacitors and installing water cooling lines inside the electronics to minimize the thermal output near the focus of the telescope. The camera also verified a non-linearity on some amplifiers which are still under investigation.

The instrument optical alignment procedures had to be improved and several minor, but very time-consuming, issues like loose screws, lack of baffling and light leaks were fixed. Also, the algorithm for the optics alignment was translated from IDL to Python from the scripts used in SOAR telescope[14].

T80S began to observe the complete set of surveys described in §1.5 in the beginning of 2017 and it is expected to finish them by 2020. A maintenance plan was designed during the commissioning and visits to the telescope by the team who installed and commissioned it is rare as most of the preventive and corrective works needed to be done can be done either remotely or by the CTIO team, which is very qualified.

The dataset produced by T80S will provide a homogeneous photometric redshift survey of the Local Universe in the southern sky and, using the techniques shown in the next chapters will also provide insights on the stellar population properties and mass assembly evolution in the Local Universe.

[14] http://www.ctio.noao.edu/~atokovin/donut/index.html

Chapter Three

A method to estimate stellar properties of galaxies from photo-z templates

In this chapter, we introduce a new method which combines the output of a Bayesian photometric redshift code with a stellar population analysis to estimate fundamental galaxy properties, with emphasis on its stellar mass $M_\star$. The method applies to any set of photometric data, but we use it to the ALHAMBRA filter set. The next chapter uses the method to construct the stellar mass function of the ALHAMBRA survey.

3.1 Motivation

The primary motivation of the work described in this chapter is to have a robust method for determining stellar masses ($M_\star$) out of photometric data alone, without relying on any spectroscopic information. As explained in the introduction to this thesis, photometric surveys like DES Dark Energy Survey Collaboration et al. (2016), JPAS (Benitez et al., 2014), LSST LSST Dark Energy Science Collaboration (2012) and others are one of the main sources of data for observational cosmology and extragalactic astrophysics nowadays. Most of these mega-surveys aim to use the data to estimate galaxy redshifts and address cosmological questions like the nature of dark energy. However, it would certainly be interesting to use these same data to learn more about galaxies than just their redshifts. This is the central motivation of the work presented in this chapter.

Many previous studies used photometry to estimate $M_\star$, like Kauffmann et al. (2003); Tremonti et al. (2004); Blanton et al. (2005); Brinchmann et al. (2004); Tojeiro et al. (2007); Taylor et al. (2011). All of these, however, make use of a spectroscopic z to map the observed filter onto the galaxy frame and to convert fluxes to luminosities, which are then combined with a stellar mass-to-light ratio (Υ) to determine $M_\star$. Taylor et al. (2011), for instance, builds an extensive library of model galaxy spectra, from which synthetic magnitudes are computed to be then compared to the SDSS DR7 u, g, r, i and z optical filters. Redshifts, obtained both with SDSS and AAOmega spectrographs, enter the calculations in

two stages. First, to convert the u, g, r, i and z transmission profiles to the galaxy's frame, compensating for the $(1+z)$ shift and stretching in wavelengths. The colours thus obtained allow the estimation of Υ_X in any filter X (the i-band in Taylor's case). The second step where z is needed is to compute the distance and then luminosities, necessary to estimate the stellar mass from $M_\star = L_i \times \Upsilon_i$ (again using the i-band as reference).

This approach needs to be modified when spectroscopic z's are not available. In general terms, one now needs to simultaneously estimate both the stellar population properties and the redshift out of photometric data alone. This is done, for instance, by Díaz-García et al. (2015) where only red galaxies are, and only those where the photo-z is precise enough to be treated as a spectroscopic z.

In this work, we separate the task of estimating z from that of estimating $M_\star$ and other stellar population properties. In broad lines, the method works as follows:

1. it applies a photo-z code to a photometric dataset D to obtain $p(z, T|D)$, the probability that a galaxy is at redshift z and is described by a spectral template T given the data;

2. it fits the template spectra in terms of stellar population models, obtaining the probability $p(\theta|z, T)$ of a given property θ (e.g., the mass-to-light ratio Υ) for fixed z and T;

3. it applies a "template expansion" to combine the photo-z probability distribution function (PDF) with the stellar property PDF to obtain $p(\theta|D)$, the probability of property θ given the data.

The main advantages of this method are:

1. The template expansion strategy limits the scope of possible galaxy spectra to a compact and representative set of real-world galaxies, reducing the color space to a realistic one, spanned by templates known to work well in photo-z estimation. This contrasts with a purely theoretical approach which allows for any mathematically possible, including physically unrealistic, galaxy colors.

2. The use of empirical spectral templates further makes it possible to remove emission lines from the modeling, cleanly circumventing the complexity of modeling both stellar populations and emission lines simultaneously.

3. Once $p(\theta|z, T)$ is calculated over a grid in z and T and for a given set of filters, estimating any galaxy stellar property is just a matter of combining $p(\theta|z, T)$ with the galaxy's redshift-template PDF $p(z, T|D)$.

4. Although we will apply our method only to the ALHAMBRA survey, the non-dependence on spectroscopic redshifts makes our method applicable to larger datasets and will enable us to have robust stellar masses probability distribution functions to any photometric redshift survey such as DES and JPAS.

The plan for this chapter is as follows. We start in §3.2 by describing the BPZ code of Benítez (2000) and how it produces a PDF of z and T given the photometric data. Our method to estimate physical properties $\vec{\theta}$ out of the output of BPZ is introduced in §3.3, where the probabilistic formalism is presented. The implementation of the method requires some pre-processing steps, the construction of stellar population models, and a code to explore the parameter space efficiently to produce the PDFs of interest, all of which are discussed in §3.4. We then proceed to §3.5, where we derive the PDFs of relevant physical properties from the BPZ templates, a key ingredient in our analysis. §3.6 explains how stellar masses are estimated. Finally, §3.7 illustrates the method by applying it to a few galaxies from the ALHAMBRA survey, combining the results of BPZ and our method to estimate of their stellar masses, mass-to-light ratios, mean stellar ages, and extinctions.

3.2 Bayesian photometric redshifts: The BPZ method

Photometric redshifts are the cheapest and fastest way for the determination of the distance of galaxies. The precision of these distances is undeniably smaller than the spectroscopic ones but the number of galaxies that can be covered with the same amount of telescope time offsets this difference. Also, as shown by many authors (Mandelbaum et al., 2008; Cunha et al., 2009; Wittman, 2009; Bordoloi et al., 2010; Abrahamse et al., 2011; Sheldon et al., 2012), it is important to adopt a probabilistic approach and derive full probability distribution functions (PDF) when dealing with photo-z's, as simple estimators like the maximum likelihood may lead to significant biases.

In this work, we use the Bayesian photometric redshift code BPZ of Benítez (2000). This section explains BPZ in detail, as most of the formalism and ingredients are the same used in the derivation of stellar properties in the next sections.

BPZ calculates the PDF of a galaxy being at a redshift z_i and of a spectral type T_j, where $i = 1 \ldots N_z$ and $j = 1 \ldots N_T$ are indices which run over pre-specified grids. In the implementation of BPZ used here z runs from 0 to 7 in steps of $\Delta z = 0.001$ (hence $N_z = 7000$), and $N_T = 41$. Fig. 3.1 shows 11 of these 41 template spectra. The others are obtained by linear interpolation between them.

The code computes the PDF of z_i and T_j for a data set D comprising observed magnitudes m_l in $l = 1 \ldots n$ filters. D therefore represents a data vector $\vec{m} = \{m_1, m_2, \ldots m_n\}$. Benítez (2000) reorganizes the data

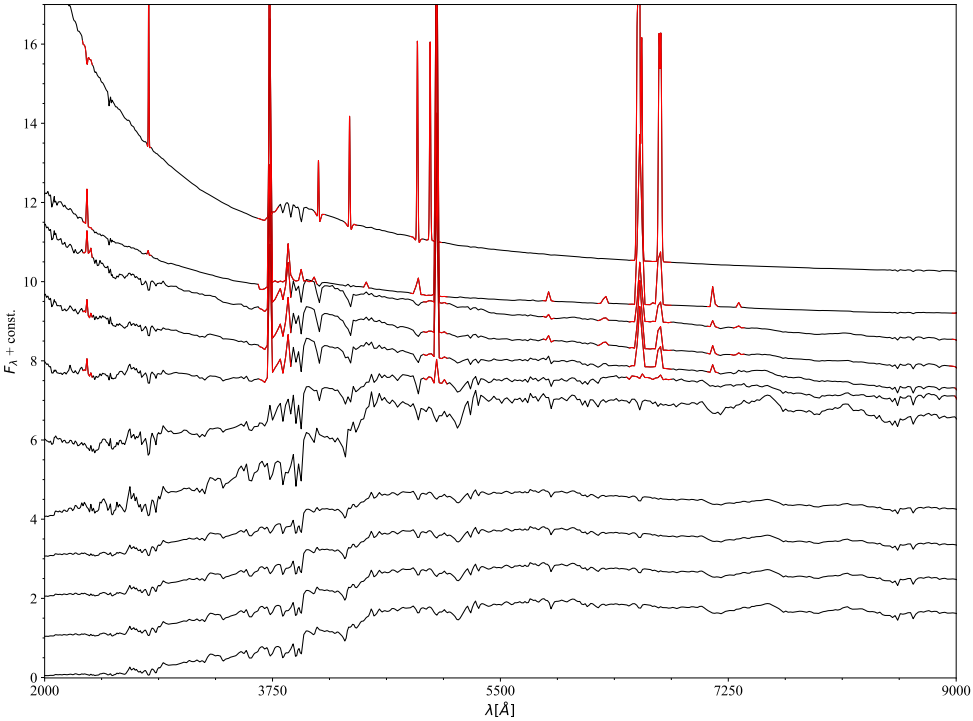

The 11 BPZ templates used on this work. From top to bottom we have 4 starburst templates, 1 Scd, 1 Sbc, 1 ESo and 4 elliptical. FIGURE 3.1

into colors $C_l = m_l - m_0$ and a reference magnitude m_0, such that D can be represented by $\{\vec{C}, m_0\}$, which is a convenient way of separating shape ($\vec{C}$), and amplitude (m_0) information. The $\vec{C}$ colors are enough to estimate the mass-to-light ratio Υ and other intensive properties (like the mean stellar age, or the extinction), while m_0 is needed to convert apparent magnitudes (or, equivalently, fluxes) to absolute ones (or luminosities) and thus stellar masses.

The goal of BPZ is thus to evaluate the probability $p(z_i, T_j|D, I) = p(z_i, T_j|\vec{C}, m_0, I)$, where, following Bayesian notational convention (e.g. Sivia and Sikilling, 2006), I stands for all assumptions involved in the analysis. From Bayes theorem, we have that[1]

[1] Though intuitively valid, this expression entails a few subtleties: First, the probability of the combination a, b, and c can be written as $p(a, b, c) = p(a|b, c) \times p(b, c) = p(b|a, c) \times p(a, c)$, from which it follows that $p(a|b, c) = p(b|a, c) \times p(a, c)/p(b, c)$. For $a \equiv (z_i, T_j)$, $b \equiv \vec{C}$ and $c \equiv m_0$, it follows that $p(z_i, T_j|\vec{C}, m_0) = p(\vec{C}|z_i, T_j, m_0) \times p(z_i, T_j, m_0)/p(\vec{C}, m_0)$. Second, $p(\vec{C}|z_i, T_j, m_0) = p(\vec{C}|z_i, T_j)$ since the colors (the spectral shape information) do depend on redshift and template, but not on m_0 (which sets the "intensity" scale). Third, $p(z_i, T_j, m_0) = p(z_i, T_j|m_0) \times p(m_0) = p(z_i, T_j|m_0)$

$$p(z_i, T_j|\vec{C}, m_0) = \frac{p(z_i, T_j|m_0) \times p(\vec{C}|z_i, T_j)}{p(\vec{C}, m_0)}, \tag{3.1}$$

where the implicit generic dependence on I has been omitted for the sake of clarity. The left side of this equation is called the posterior. On the right side we have the product of the prior on z_i and T_j times the joint template-redshift likelihood, divided by the so-called evidence of the data. Since we are just interested in the estimation of z and T, the evidence turns into an ordinary normalization constant (Sivia and Sikilling, 2006), as is common in Bayesian work. Let us examine the two terms in the numerator of eq. 3.1.

The likelihood $p(\vec{C}|z_i, T_j)$ expresses the probability of the colors $\vec{C}$ given that the redshift is z_i and the spectral type is T_j. For gaussian errors,

$$p(\vec{C}|z_i, T_j) \propto e^{-\frac{1}{2}\chi^2_{ij}} \tag{3.2}$$

where χ^2_{ij} measures the difference between the observed and template colors. These are better expressed in terms of the differences in magnitudes:

$$\chi^2_{ij} = \sum_{l=1}^{n} \left(m_l - m^T_{l,ij} + A_{ij} \right)^2 w_l^2 \tag{3.3}$$

where m_l is the observed magnitude in filter l, $m^T_{l,i,j}$ denotes the magnitude of template j at redshift z_i in filter l, and the weight w_l[2] is the inverse of the uncertaintiy in m_l, i.e., $w_l = \frac{1}{\sigma_l}$. Since the template spectra come in arbitrary units, the template magnitudes $m^T_{l,i,j}$ are not really comparable to the observed ones (m_l) in absolute value. This is the role of the term A_{ij}, defined to minimize the difference between m_l and $m^T_{l,ij}$ over all filters: $A_{ij} = \sum w_l^2 (m^T_{l,ij} - m_l) / \sum w_l^2$, as obtained from $\partial\chi^2/\partial A_{ij} = 0$. In summary, equations 3.2 and 3.3 quantify the spectral similarity between template j at redshift z_i and the observations, irrespective of differences in scale.

Let us now turn to the first term on the right side of eq. 3.1. The template-redshift prior $p(z_i, T_j|m_0)$ is used to modulate the likelihood such that unrealistic template, redshift, and apparent magnitude combinations are given less weight than more realistic ones. In practice, two effects are taken into account with this prior: galaxies cannot be too far if they are bright (i.e. low apparent magnitude m_0) and average galaxy colors must be slightly bluer as z increases.

Fig. 3.2, taken from Benítez (2000), exemplifies both the likelihood and prior terms (top two panels, respectively). The curves are drawn for

since $p(m_0)$ can be set to a constant = 1 without loss of generality. The outcome of these developements is eq. 3.1.

[2] This weight can be changed to accommodate, for example, templates with intrinsic errors, error scaling factors, etc.

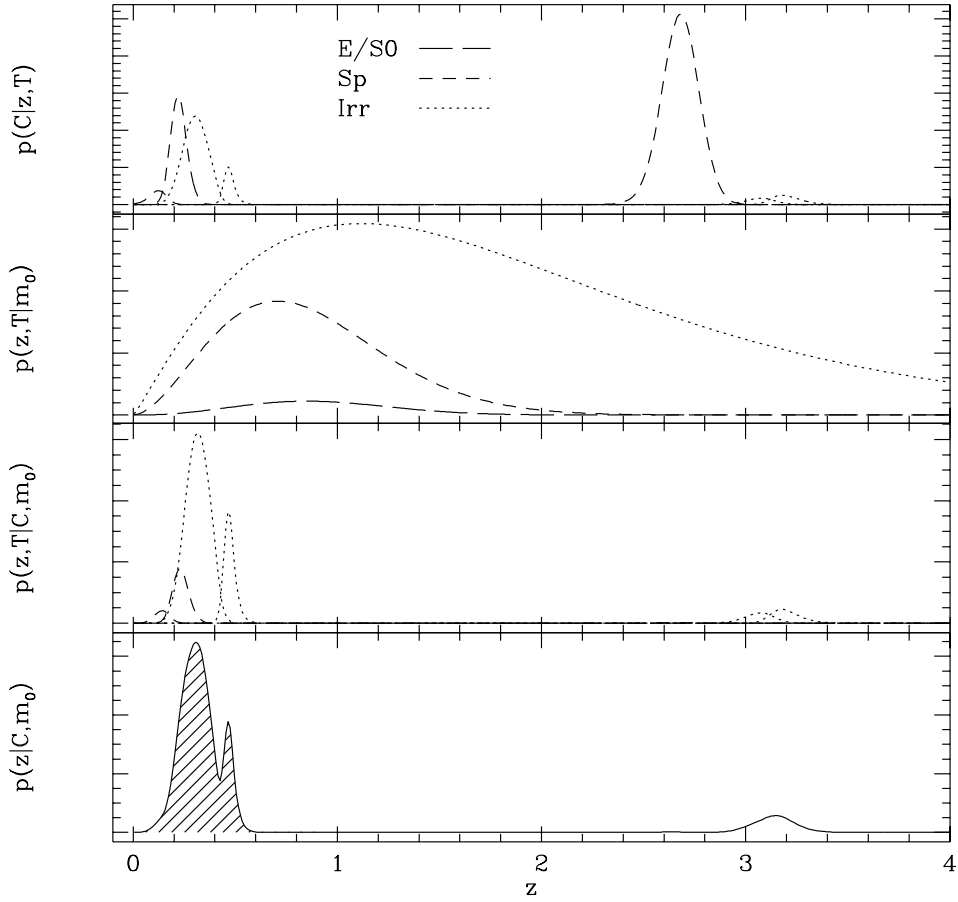

FIGURE 3.2

From Benítez (2000). The panels illustrate how BPZ works. The data in this case is a fake galaxy with an Irr spectral type with I $\approx$ 26 to which noise was added to seven bands (UBVIJHK). From top to bottom: *(a)* Likelihood of the observed colors as a function of z for templates representing three spectral types, E/So, Sp, and Irr. *(b)* Joint redshift template prior. *(c)* Posterior probability of z and T given the data and prior. *(d)* PDF of z after marginalization over the template space.

three templates, referred to as E/So (representative of elliptical/lenticular galaxies), Sp (for spirals) and Irr (for Irregulars). By itself, the likelihood favors a $z \sim 2.7$ Sp solution, although solutions in the $z = 0.2$–0.6 range are also plausible. The high-z solution is however highly unlikely. Basically, it implies too large a luminosity for a galaxy, and this is reflected in the second panel in Fig. 3.2, where the prior is plotted. This prior distribution is empirically calibrated using colors and spectroscopic redshifts for the Hubble Deep Field North. The posterior probability, $p(z, T|\vec{C}, m_0)$, plotted in the third panel from the top, combines the likelihood with the prior. Note that, if a flat prior were assumed, the most likely redshift for the galaxy would be around 2.7, but, after applying the prior distribution, this peak goes back to around $z \sim 0.3$, and the preferred template is Irr, the correct solution.

Marginalizing over all templates leads to the final PDF for z, plotted in the bottom panel of Fig. 3.2. This is the primary product of BPZ, and indeed of any photo-z code. For our purposes, however, the primary output of BPZ is the one shown in the third panel from the top in Fig. 3.2, the joint template-redshift probability distribution, $p(z_i, T_j|\vec{C}, m_0)$. This is the essential ingredient for the developments below.

3.3 From $p(z, T|D)$ to $p(\vec{\theta}, z|D)$: Estimatting stellar properties

The goal of a stellar population analysis of a set of data D is to estimate properties (or parameters) which describe the galaxy's star formation history. Let $\vec{\theta}$ be a generic vector of such properties, so that the goal is to evaluate $p(\vec{\theta}|D)$. The redshift may be seen as one of the components of $\vec{\theta}$, but let us treat it separately. Also, as in the previous section, let us separate the photometric data into shape and amplitude terms, $D = \{\vec{C}, m_0\}$. The goal is thus to derive

$$p(\vec{\theta}, z|\vec{C}, m_0) \tag{3.4}$$

the probability of $\vec{\theta}$ and z given the data.

One way to approach this problem is to build an extensive grid $\vec{\theta}_k$, $k = 1 \ldots N_S$, and compute the galaxy spectra S_k corresponding to the $\vec{\theta}_k$ parameters. Further discretizing z in a $\{z_i,\ i = 1 \ldots N_z\}$ grid leads to a combined $N_S \times N_z$ space of $(\vec{\theta}_k, z_i)$ combinations, whose predicted photometry can be compared to the data to evaluate eq. 3.4. This essentially what BPZ does, except that it uses a library of templates T_j instead of parametric S_k model spectra. As already mentioned, the problem with this approach is that the $k = 1 \ldots N_S$ model-space can be huge and may contain many spectra which are not realistic, in the sense of not being present in the galaxy population. It is therefore not practical to calculate these probabilities directly (using BPZ or other similar codes) since the color/redshift degeneracies will be much worse than for a compact,

well-calibrated empirical library. Naturally, these degeneracies affect not only the ability to recover z but also the estimation of stellar population properties.

To circumvent these difficulties let us write

$$p(\vec{\theta}_k, z_i|\vec{C}, m_0) = \sum_{j=1}^{N_T} p(\theta_k, z_i, T_j|\vec{C}, m_0) \tag{3.5}$$

which can be described as a "template expansion". Using the chain rule, the term inside the summation on the right-hand-side can be re-written as

$$p(\vec{\theta}_k, z_i, T_j|\vec{C}, m_0) = p(z_i, T_j|\vec{C}, m_0)p(\vec{\theta}_k|z_i, T_j, \vec{C}, m_0) \tag{3.6}$$

These two equations contain the essence of our method. The first term on the right, $p(z_i, T_j|\vec{C}, m_0)$, gives the probability of a galaxy being at redshift z_i and of spectral type T_j given its observed photometry. This is a direct product of BPZ. Indeed, this term is exactly the same as eq. 3.1. Our task is thus simplified to the evaluation of the second term, $p(\vec{\theta}_k|z_i, T_j, \vec{C}, m_0)$, the probability of properties $\vec{\theta}_k$ given z_i, T_j and the data.

In fact our task is even simpler, since $\vec{C}$ and m_0 may be dropped from the right of the condition bar in $p(\vec{\theta}_k|z_i, T_j, \vec{C}, m_0)$. The first can be dropped because matching the colors $\vec{C}$ is basically the same as matching the spectral type T_j, so it is redundant to have both to the right of the condition bar. The second (m_0) may be dropped by ensuring $\vec{\theta}$ does not include distance-dependent quantities. For example, as long as $\vec{\theta}$ includes the stellar mass-to-light ratio, but not the stellar mass, the dependence on m_0 may be omitted. In the end, we have

$$p(\vec{\theta}_k|z_i, T_j, \vec{C}, m_0) = p(\vec{\theta}_k|z_i, T_j) \tag{3.7}$$

i.e., the probability that a galaxy with stellar properties $\vec{\theta}_k$ matches the photometry of a template T_j at redshift z_i. From Bayes theorem, and ignoring normalization factors

$$p(\vec{\theta}_k|z_i, T_j) \propto p(\vec{\theta}_k|z_i)p(T_j|\vec{\theta}_k, z_i) \tag{3.8}$$

where the prior $p(\vec{\theta}_k|z_i)$ may include constraints like one which forbids stars in the model $\vec{\theta}_k$ to be older than the corresponding age of the Universe at redshift z_i. The likelihood term can be written as

$$p(T_j|\vec{\theta}_k, z_i) \propto e^{-\frac{1}{2}\chi^2_{ijk}} \tag{3.9}$$

where

$$\begin{aligned}\chi^2_{ijk} &= \chi^2(\vec{\theta}_k, T_j, z_i) \\ &= \sum_{l=1}^{n} \left(m_l(\vec{\theta}_k, z_i) - m_l(T_j, z_i) + A_{ijk} \right)^2 w_l^2 \end{aligned} \tag{3.10}$$

In this expression $m_l(\vec{\theta}_k, z_i)$ denotes the magnitude at filter l of the model spectrum $S_k = S_k(\vec{\theta}_k)$ at $z = z_i$ and $m_l(T_j, z_i)$ is the magnitude of template T_j in the same filter and redshift. As in eq. 3.3, the term A_{ijk} accounts for irrelevant scale offsets between model and template magnitudes, and can be trivially obtained from $\partial\chi^2_{ijk}/\partial A_{ijk} = 0$.

The weights w_l in eq. 3.10 need not be the inverse of the errors in the observed magnitudes. In fact, eq. 3.10 is not directly related to the data. This occurs because $p(\vec{\theta}_k|z_i, T_j)$ itself (eq. 3.8) make no explicit reference to the data. We are actually fitting the $l = 1 \ldots n$ photometry of template T_j with a model S_k (both at $z = z_i$). The choice of w_l can thus be tuned to reflect the degree to which we want these fits to work. The standard choice in this thesis will be to define $w_l = w = \frac{1}{\epsilon}$ with $\epsilon = 0.05$ mag. This value is typical of the photometric precision of ALHAMBRA (Molino et al., 2014) and it is the same value was used by Taylor et al. (2011) as an error-floor in their analysis. The effects of ϵ upon our results will be discussed below.

Grouping the main equations above, we have that:

$$\begin{aligned} p(\vec{\theta}_k, z_i|\vec{C}, m_0) &= \sum_{j=1}^{N_T} p(z_i, T_j|\vec{C}, m_0) p(\vec{\theta}_k|z_i, T_j) \\ &\propto p(\vec{\theta}_k|z_i) \sum_{j=1}^{N_T} p(z_i, T_j|\vec{C}, m_0) e^{-\frac{1}{2}\chi^2_{ijk}} \end{aligned} \tag{3.11}$$

Before moving on to describe how we implement this method, let us summarize in words the main ideas behind this mathematical formalism. In its essence, the method *(1)* "outsources" the estimation of redshift and spectral type to BPZ, which does this through its joint (z_i, T_j) PDF; *(2)* estimates the stellar properties of the BPZ templates by matching them to model stellar galaxy spectra observed at the same z and through the same filters as the data, and *(3)* combines the results with the BPZ PDF for (z_i, T_j) to estimate the stellar properties.

3.4 Implementation of the method

In this section we show how we estimate $p(\vec{\theta}_k|z_i, T_j)$, the probability of properties $\vec{\theta}_k$ for a given template and redshift. As seen above, this involves comparing template and model magnitudes (eq. 3.10). Since our goal in this work is to test our method, and there are endless combinations of possible ways to model a set of galaxy magnitudes, we carried

$$p(\vec{\theta}_k, z_i|\vec{C}, m_0) = \sum_{j=1}^{N_T} p(z_i, T_j|\vec{C}, m_0) p(\vec{\theta}_k|z_i, T_j) \quad \text{(Eq. 3.10)}$$

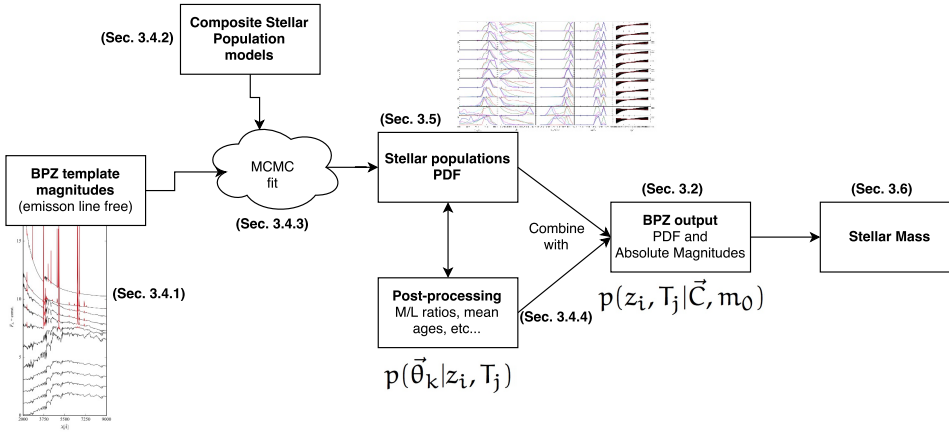

FIGURE 3.3 Scheme of how BPZ templates are fitted with a set composite stellar population models to obtain $p(\vec{\theta}_k|z_i, T_j)$, later combined with the output of BPZ to estimate the PDF of stellar properties $\vec{\theta}$, including the stellar mass.

out the spectral fitting in an easy way. Specifically, we model galaxy spectra as produced by an exponentially decaying burst of star formation of a single metallicity and attenuated by a screen of dust. The widely used models of Bruzual and Charlot (2003) are used to compute these model spectra. This traditional approach has been previously followed by several studies, like (Brinchmann et al., 2004; Bundy, 2006; Pozzetti et al., 2007; Taylor et al., 2011). All of these, however, assumed knowledge of a spectroscopic z, while our method does not. Our innovation is therefore not on the stellar population modeling, but on the way, we extract both a photo-z and galaxy properties $\vec{\theta}$ out of purely photometric data.

Fig. 3.3 shows a schematic flow chart of the whole process, which involves the following steps:

1. The first step is to adequate the BPZ template spectra to be comparable to composite stellar populations models. This pre-processing step is described in §3.4.1.

2. One then needs to formulate a recipe to create a model spectrum, which we do in a simple parametric way explained in §3.4.2.

3. Template and model colors are then compared by means of a Markov Chains Monte Carlo (MCMC) code that maps the parameter space, computing $\chi^2_{ijk} = \chi^2(\vec{\theta}_k, T_j, z_i)$. These are then used to produce

PDFs of the parameters $\vec{\theta}$ and others associated with it. This step is detailed in §3.4.3 and §3.4.4.

4. The results are then combined with the $p(z_i, T_j|D)$ output by BPZ to produce the final estimate of galaxy properties, as illustrated in §3.7.

3.4.1 Pre-processing of the BPZ templates: Emission line removal

In this work we used the results of version 2.0 of BPZ (Benítez et al, in prep.) applied to the ALHAMBRA-Gold catalogue[3] described by Molino et al. (2014). The template library used in these works comprises the eleven spectra shown in Fig. 3.1. Five templates were originally drawn from PEGASE library Fioc and Rocca-Volmerange (1997) and re-calibrated using FIREWORKS photometry and spectroscopic redshifts (Wuyts et al., 2008). This recalibration is done to adjust small inter-calibration offsets that may exist between the spectroscopic templates and the photometric colors. In addition five GRASIL (Silva et al., 1998) and one extreme Starburst template were added to form the library. BPZ interpolates from these 11 templates, leading to a final library of $j = 1 \ldots N_T = 41$ templates T_j for each redshift z_i.

Before fitting these templates with stellar populations, we first remove their emission lines. These are important for BPZ, as they carry information relevant for the estimation of z. For a stellar population analysis, however, emission lines must be removed. In figure 3.1 we mark in red the spectral regions which are chopped from the analysis because of emission lines. This is, in fact, a clear advantage of our method compared to those who fit the observed photometry directly. This more direct approach has to include emission lines in the modeling, which is not only complex but also enlarges the parameter space significantly (from one containing only stellar population properties to a large space also containing the properties of the ionized gas). Our approach circumvents such difficulties in a straightforward and elegant way, leaving the emission lines for the photo-z estimate, but eliminating them from the stellar population analysis.

Once emission lines were removed, we then evaluate the magnitudes $m_l^T(z_i, T_j)$ of each template at each redshift and for each of the $l = 1 \ldots n$ filters. As explained before, the template spectra are in arbitrary units, but this is not important because scale factors are corrected for in the comparison of model and template magnitudes (cf. eq. 3.10).

After these pre-processing steps, the template magnitudes $m_l^T(z_i, T_j)$ are ready to be fitted with the models described next.

[3] https://cloud.iaa.csic.es/alhambra/

Parameter	Units	min/max values	Description
t_0	yr	10^6 to $t_U(z)$	Age of the exponential burst. $t_U(z)$ is the age of Universe at z
β	–	0.1 to 10	$\beta = \tau/t_0$. τ is the burst e-folding time
Z	$Z_\odot$	0.2, 0.4, 1, 1.5	Stellar metallicity
A_V	mag	-0.1 to 2	Extinction in the V-band.

Synthetic CSP library parameters priors and descriptions. TABLE 3.1

3.4.2 Model spectra for composite stellar populations

Model magnitudes m_l are computed from model spectra generated from the BC03 library of simple stellar populations (SSP). These models provide the spectrum $SSP_\lambda(t, Z)$ of an SSP of age t and metallicity Z for 221 ages between 0 and 20 Gyr and 6 metallicities between 1/200 and $2.5Z_\odot$. The predictions for the two lowest metallicities (1/200 and 1/50 solar) are highly uncertain, so we will not consider those in our modeling. This should not be a problem, as these Z's are too low to represent real galaxies anyway.

Galaxies are not SSPs. Their actual star formation histories (SFH) are complex and still the subject of much investigation (Asari et al., 2007; Tojeiro et al., 2007; Pacifici et al., 2016). As anticipated above, we will follow the simple and widely used strategy of modeling the time-dependence of the star formation rate (SFR) with an exponentially decaying function

$$\psi(t) = \begin{cases} \psi_0 e^{-\frac{(t_0 - t)}{\tau}} & \text{if } t \leq t_0 \\ 0 & \text{otherwise.} \end{cases} \tag{3.12}$$

where t_0 is the lookback time of the start of the burst, t is age of the stellar population, and the e-folding time-scale τ = (see Maraston et al., 2010, for criticisms about this approach). For $\tau \ll t_0$ the model behaves like an SSP of age $t_0 - t$, while when τ is of the order of t_0 or larger $\psi(t)$ approaches a constant SFR regime. The actual effect of τ is therefore better represented by the ratio $\beta = \tau/t_0$ than by the value of τ itself.

The spectrum of a composite stellar population (CSP) whose history is described by the SFR function $\psi(t)$ can be obtained integrating the spectra of SSPs, from those as old as the Universe at corresponding redshift, $t = t_U(z)$, to the ones born today, $t = 0$:

$$S(\lambda) = \int_0^{t_U(z)} SSP_\lambda(t, Z)\psi(t)dt \times 10^{-0.4 A_V q_\lambda} \tag{3.13}$$

The term on the right of eq. 3.13 describes the attenuation by a screen of dust. The extinction is measured by its contribution on the V-band, A_V, while $q_\lambda = A_\lambda/A_V$ describes the reddening law. In our experiments we used both the Cardelli et al. (1989) and Calzetti et al. (1994) laws.

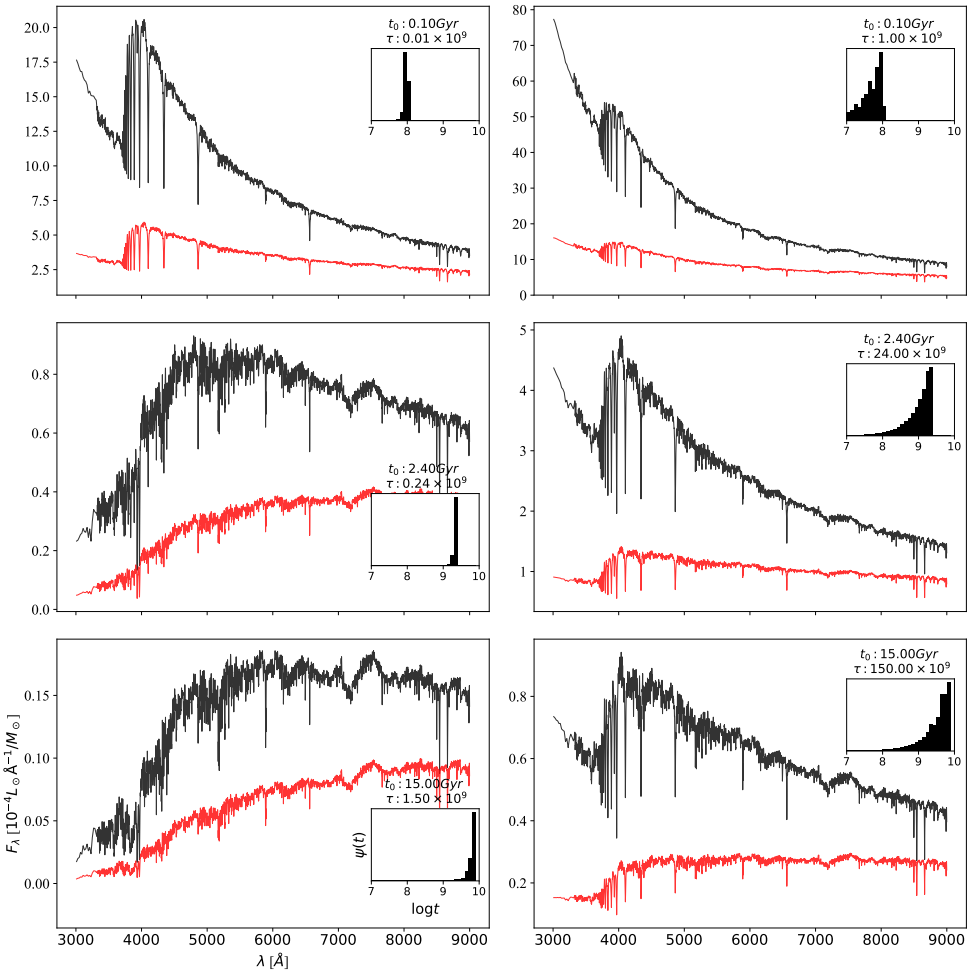

FIGURE 3.4 Example of typical composite stellar populations used on the fit. From top to bottom CSPs with burst starting at ages $t_0 = 0.1, 2.4$ and $15Gyr$. The left panels have $\beta = \tau/t_0 = 0.1$ and the right panels $\beta = 10$.

In Fig. 3.4 we plot six examples of CSP spectra generated with this recipe. In each panel we plot $\psi(t)$ and the corresponding spectrum. The examples correspond to $t_0 = 0.1, 2.4$ and 15 Gyr, in the top, middle, and bottom rows, and $\beta = 0.1$ on the left and $\beta = 10$ on the right. We also show in red the same CSP spectrum but with $A_V = 1$ mag of extinction with a Calzetti et al. (1994) law. The BC03 SSP models used to construct these CSP spectra use the Chabrier (2003) initial mass function (IMF) and Padova 1994 stellar evolution tracks.

The $\psi(t)$ functions in the insets of Fig. 3.4 are shown as sampled in the discrete t-grid of BC03, which explains why they sometimes do not look as simple exponentials. In fact, in practice eq. 3.13 is evaluated discretely as a sum over all SSP populations:

$$S(\lambda) = \sum_{i=1}^{N_{SSP}} SSP_\lambda(t_i, Z)\psi(t_i)\Delta t_i \times 10^{-0.4 A_V q_\lambda} \tag{3.14}$$

where $\psi(t_i)\Delta t_i$ is the mass formed in stars with ages in the Δt_i range around t_i.

Equation 3.13, or its discrete version 3.14, give the spectrum $S(\lambda)$ for a model galaxy described by parameters $\vec{\theta} = (t_0, \tau, A_V, Z)$. Rigorously speaking, ψ_0 should also be included as a 5^{th} parameter in this list. However, ψ_0 only affects the amplitude of $S(\lambda)$, which makes it irrelevant because the comparison of models and template photometry (via eq. 3.10) will be made only in terms of colors. In other words, the absolute scale of $S(\lambda)$ is not important at this stage.

Table 3.1 lists the allowed ranges for t_0, $\beta = \tau/t_0$, A_V, and Z. The first three are treated as continuous variables, while Z can only assume one of the four metallicities allowed as interpolating SSP models to other metallicities is not recommendable. These ranges can be understood as an implicit prior on the parameters vector $\vec{\theta}$ (the same prior appearing in eq. 3.11). These ranges were chosen to be similar to existing studies on the literature, like Taylor et al. (2011) and Brinchmann et al. (2004). Our goal is to use a set of well known and tested constraints to be able to isolate sources of the error from the new methodology that we are developing here to known sources of error from the models themselves. Once the method is proven to give good results, playing with different priors and SSP model libraries should be straightforward.

Synthetic magnitudes are obtained from $S(\lambda)$ by convolving it with the filter curves and redshifting the model spectrum to the appropriate z. For a filter l with transmission curve R_λ:

$$m_l(\vec{\theta}, z) = -2.5 \log \frac{\int_l S(\lambda')' R_\lambda \lambda d\lambda}{\int_l \lambda^{-1} R_\lambda d_\lambda} - 2.41 \tag{3.15}$$

where the prime means that these observables were shifted to the observed frame, i.e., $\lambda' = \lambda(1+z)$ and $S' = S/(1+z)$. Note also that the

term 2.41 (which comes from the definition of AB magnitudes) is actually superfluous here, since, as explained before, we only care about the synthetic colors, so zero points are irrelevant at this stage.

If we substitute $S(\lambda)$ from eq 3.14 and re-arrange the terms that do not depend on λ outside the integral we have

$$m_l(\vec{\theta}, z) = -2.5 \log \sum_{i=1}^{N_{SSP}} \psi(t_i) \Delta t_i \frac{\int_l SSP'_{\lambda'}(t_i, Z) 10^{-0.4 A_V q_{\lambda'}} R_\lambda \lambda d\lambda}{\int_l \lambda^{-1} R_\lambda d_\lambda} \tag{3.16}$$

The calculation of $S(\lambda)$ and the associated magnitudes can be computationally expensive, specially if we want to span the full parameter-space in order to map the probability distribution function of $\vec{\theta}$. To speed up the calculations we expand the term $10^{-0.4 A_V q_\lambda}$ as a Taylor series[4] centered on the filter's pivotal wavelength and limit the expansion to the first 10 terms. This allows us to calculate the integral part of eq. 3.16 (which is the most computationally intensive) beforehand and cache it for further use.

Evaluating eq. 3.16 for parameters $\vec{\theta}_k$ and for redshifts z_i gives us the model magnitudes $m_l(\vec{\theta}_k, z_i)$ that we need to plug in eq. 3.10, where they are compared to the template magnitudes $m_l^T(z_i, T_j)$. This comparison yields χ^2_{ijk}, which then allows us to compute $p(\vec{\theta}_k | z_i, T_j)$, the probability of parameters $\vec{\theta}_k$ given a redshift-template pair. This is our main goal here, since, as explained above, the rest of the work is outsourced to BPZ. In the next section we explain how to explore the parameter space $\vec{\theta}_k$ to evaluate $p(\vec{\theta}_k | z_i, T_j)$.

3.4.3 Fitting BPZ template colors with CSP models: Mapping the parameter space with an MCMC method

There is not an unique approach for estimating $p(\vec{\theta}_k | z_i, T_j)$. The simplest technique would be to make a fine grid on the model space, generating a set of $\vec{\theta}_k$ values, with $k = 1 \ldots N_S$. For each point in this grid one would derive model magnitudes and compute the corresponding χ^2_{ijk} (eq. 3.10). This grid-based technique is widely used in the literature (e.g., Gallazzi et al., 2005). A problem with this approach is that most of the mathematically possible models are not physically realistic, so a smarter parameter space search was developed.

To explore the parameter/color space more wisely, we used an MCMC method. For that, we used the recent but already widely used emcee[5] code (Foreman-Mackey et al., 2013) to map the probability space on regions where the probability is non-negligible ("importance sampling", in the language of Silva et al. (1998)). The emcee code is a Python code

[4] Another approach to this could be to use brute-force and calculate the integral on the A_V prior interval with very small steps of, i.e., 0.01 mag.

[5] `https://github.com/dfm/emcee`

that implements the affine-invariant ensemble sampler for Markov Chain Monte Carlo (MCMC). We randomly initialize 70 walkers and sample the parameter space looking for a set of most probable likelihoods. To achieve that, we run each walker for 3000 steps, removing the first 1000 steps as a burn-in phase. After removing the burn-in steps, we evaluate fine (1000 bins) histograms on all properties. The result is a likelihood array $p(\vec{\theta_k}|z_i, T_j)$ with $k = 1, \ldots, 1000$ which, combined with the photometric redshift $p(z_i, T_j|\vec{C}, m_0)$ on equation 3.8, will give us the stellar properties.

Figs. 3.5 and 3.6 illustrate how the MCMC code works. The two examples are chosen to represent typical elliptical and spiral galaxies, respectively.

In Fig. 3.5 we are fitting a test galaxy generated with $t_0 = 13$ Gyr, $\tau = 1.6$ Gyr, $A_V = 0.016$ mag, and $Z = 2.5Z_\odot$, an old, metal rich and little reddened population similar to that found in elliptical galaxies. The top four panels show the 3000 iterations of the MCMC code, which each line representing one of 7 randomly chosen walkers (or chains). Each panel represents one of the four dimensions of $\vec{\theta}$: t_0 (top panel), $\beta = \tau/t_0$ (second panel from the top), A_V (third), and Z (fourth) with the χ^2 for each chain on the fifth panel. The bottom panel shows the input photometry (red line and dots) and its $\pm 1\sigma$ uncertainty. These values were generated from the input parameters and perturbed with gaussian noise with $\sigma = 0.05$ mag. The black lines draw 1000 randomly selected "spectra". The right panel histograms are non-weighted histograms of the frequency of how each parameter was explored by the walkers.

In Fig. 3.6 we repeat the experiment, this time for parameters more characteristic of spiral galaxies: $t_0 = 5.5$ Gyr, $\tau = 2.9$ Gyr, $A_V = 0.7$ mag, and $Z = 1/2Z_\odot$. Again, the model photometry was perturbed with 0.05 mag gaussian noise and shown the same way done on Fig. 3.5.

These plots illustrate 7 out of 70 chains starting randomly distributed on the parameter space (Table 3.1) and how they evolve during the 3000 steps. We see in the 1^{st} and 2^{nd} panels from top of Fig. 3.6 that sometimes one or two chains take a bit more than the 1000 burn-in steps to go from a local minimum to the global, but this does not impact the determination of the stellar properties, since the majority of the chains find their way to the global minimum, as seen on the histograms drawn on the right. Also, the values of the parameters of those chains are penalized with a lower probability than the others.

Since the photometry is disturbed by a Gaussian noise of $\sigma = 0.05$ mag, there is no need to the model that fits best the photometric points to be exactly the one generated by the input parameters. This is evident in Fig. 3.6, where the fitted parameteres correspond to models a bit youger and less metallic but with more extinction than the ones used as input (indicated by the red lines). The models agree in general, but not exactly, as expected. As we add up noise, the probability distributions broaden and the degerenacies (like the age-extinction degeneracy) becomes more

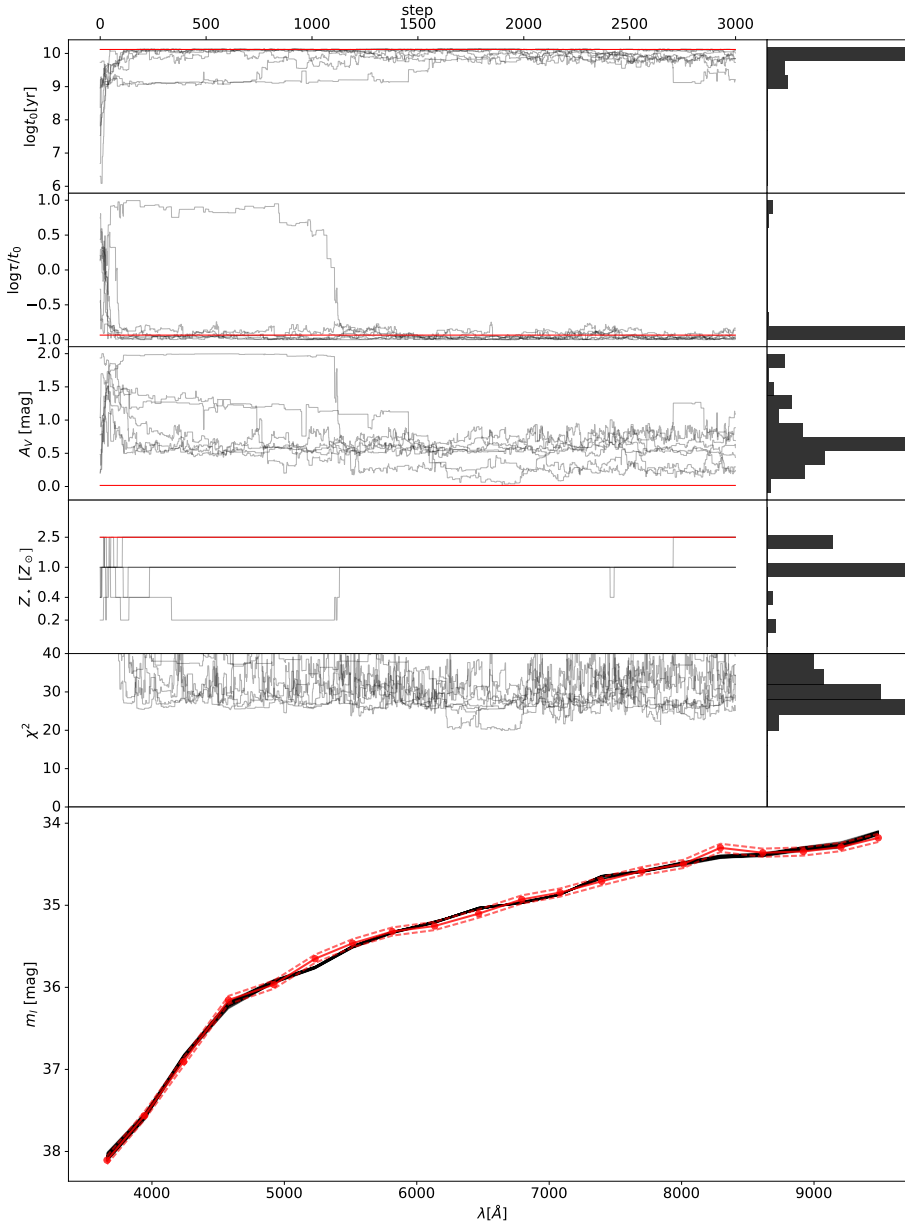

FIGURE 3.5 Full chain example. For each step, we show in the left panels fitted parameter evolution over the steps in x axis while in the right panels, a histogram for all steps also for each fitted parameter burst initial age t_0, e-folding time $\beta = \tau/t_0$, extinction A_V and metallicity Z. The red lines are the "true" values of parameters used to generate the random CSP that was used as input.

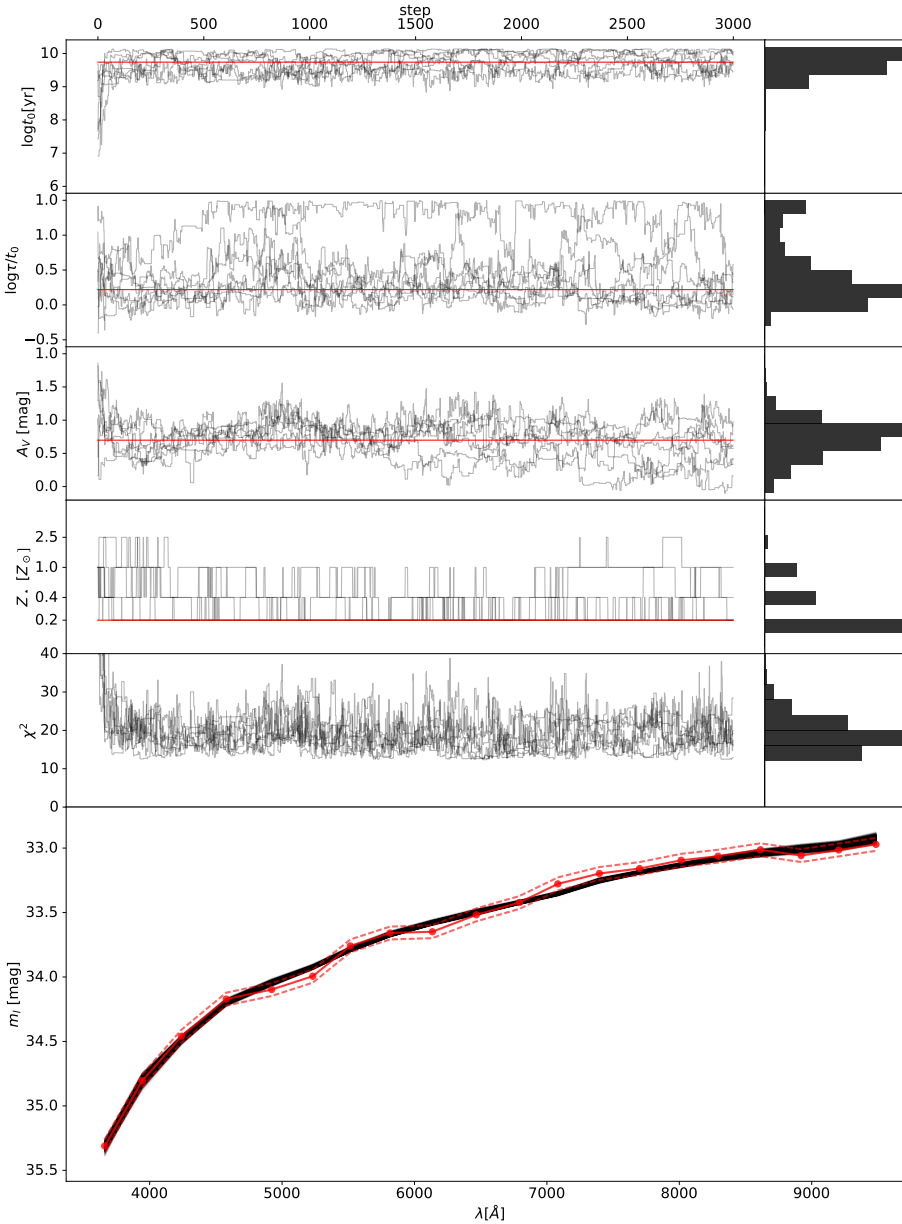

As Fig. 3.5, but for a mock galaxy with younger stellar populations, emulating the case of a spiral galaxy. The true parameters in this case are $t_0 = 5.5$ Gyr, $\tau = 2.9$ Gyr, $A_V = 0.7$ mag, and $Z = 1/2Z_\odot$.

FIGURE 3.6

noticeable.

Figs. 3.5 and 3.6 are just two of many simulations carried out to test our method. A detailed description of these tests can be found in appendix A, where we quantify how the photometric error and redshift affect the estimation of stellar population properties of interest.

The adopted MCMC parameters (70 chains with 3000 steps each and a burn-in phase of 1000 steps on each chain) are very conservative and could be easily reduced to improve the speed of the fitting, but the method itself with these parameters runs with reasonable speed. Also, it is worth to mention once again that once this fit is ran for a model+filter set, the resulting $p(\vec{\theta}|z_i, T_j)$ is stored and used for all the galaxies of a survey without need of re-calculation.

3.4.4 Mean ages and mass-to-light ratios

With the steps described above we are ready to apply our method to the BPZ templates T_j at redshifts z_i and derive $p(\vec{\theta}|z_i, T_j)$, where $\vec{\theta}$ represents (t_0, β, A_V, Z). However, it is more interesting and relevant for this work to express our results not in terms of these four parameters, but in terms of mean stellar ages $\langle \log t_\star \rangle$ and the mass-to-light ratio Υ. We thus want to move from a description originally based on $\vec{\theta} = (t_0, \beta, A_V, Z)$ to one where $\vec{\theta}$ represents the properties we actually want to estimate, $(\langle \log t_\star \rangle, \Upsilon, A_V, Z)$.

The motivation to estimate Υ should be obvious, since the primary goal of this whole study is to determine stellar masses, and these come from the combination of a luminosity with a mass-to-light ratio. Regarding $\langle \log t_\star \rangle$, mean stellar ages are far more widely used that the pair (t_0, β) to summarize the SFH of galaxies (e.g. Cid Fernandes et al., 2005; Gallazzi et al., 2005; González Delgado et al., 2015). Moreover, using $\langle \log t_\star \rangle$ instead of (t_0, β) reduces the description of a galaxy's SFH to a single value, mitigating degeneracies and thus leading to more robust results.

3.4.4.1 The mean stellar age $\langle \log t_\star \rangle$

We define a mean log stellar age as

$$\langle \log t_\star \rangle = \sum_{i=1}^{N_{SSP}} w_i \log t_i \tag{3.17}$$

where the weight w_i is given by

$$w_i = \frac{(1 - r_i)\psi(t_i)\Delta t_i}{\sum_{i=1}^{N_{SSP}} (1 - r_i)\psi(t_i)\Delta t_i} \tag{3.18}$$

if we want a mass-weighted mean age. The factor $(1 - r_i)$ corrects the mass $\psi(t_i)\Delta t_i$ originally formed in stars which now have age t_i by the mass which has been returned to the ISM by winds and SNe.

Alternatively, we may define

$$w_i = \frac{SSP_\lambda(t, Z)\psi(t_i)\Delta t_i}{\sum_{i=1}^{N_{SSP}} SSP_\lambda(t, Z)\psi(t_i)\Delta t_i} \tag{3.19}$$

if we want $\langle \log t_\star \rangle$ to represent a luminosity-weighted mean age. We will work with the luminosity weighted definition, as is usual in stellar population studies (e.g. Cid Fernandes et al., 2005). Our $\langle \log t_\star \rangle$ values are computed at a reference wavelength of 5500 Å (the V-band).

3.4.4.2 The mass-to-light ratio Υ

The mass-to-light ratio at a wavelength λ is trivially obtained from $S(\lambda)$ as given by eq. 3.13 (or its discrete form, eq. 3.14) divided by the stellar mass.

As usual in stellar population studies, one may work with either the total mass ever turned into stars $M'_\star = \int_0^{t_0} \psi(t)dt$, or with the mass which actually remains in stars at the time of the observation ($t = 0$):

$$M_\star = \int_0^{t_0} (1 - r(t))\psi(t)dt = \sum_{i=1}^{N_{SSP}} (1 - r_i)\psi(t_i)\Delta t_i \tag{3.20}$$

where again $r = r(t)$ denotes the returned mass fraction. This is the definition we need to estimate current stellar masses. The mass-to-light ratio is thus

$$\Upsilon_\lambda = \frac{\int_0^{t_0} (1 - r(t))\psi(t)dt}{\int_0^{t_0} SSP_\lambda(t, Z)\psi(t)dt \times 10^{-0.4 A_V q_\lambda}} \tag{3.21}$$

or, in discrete form,

$$\Upsilon_\lambda = \frac{\sum_{i=1}^{N_{SSP}} (1 - r_i)\psi(t_i)\Delta t_i}{\sum_{i=1}^{N_{SSP}} SSP_\lambda(t_i, Z)\psi(t_i)\Delta t_i \times 10^{-0.4 A_V q_\lambda}} \tag{3.22}$$

This gives monochromatic mass-to-light ratios at λ, in units of, say, $M_\odot/(L_\odot \text{Å}^{-1})$. To obtain Υ for a filter X the denominator in eqs. 3.21 and 3.22 must be integrated over the filter response curve. This converts $S(\lambda)$ to S_X:

$$S_X = \frac{\int_X S(\lambda) R_\lambda \lambda d\lambda}{\int_X R_\lambda \lambda^{-1} d\lambda} \tag{3.23}$$

3.5 Results: $p(\langle \log t_\star \rangle, \Upsilon, A_V, Z | z_i, T_j)$

Let us finally evaluate the PDFs of our parameters of interest ($\langle \log t_\star \rangle$, Υ, A_V and Z) for the BPZ templates. As expressed in the introduction our primary interest is to derive masses, so the main parameter here is Υ. Still, we want to test whether we can use the same data and method to

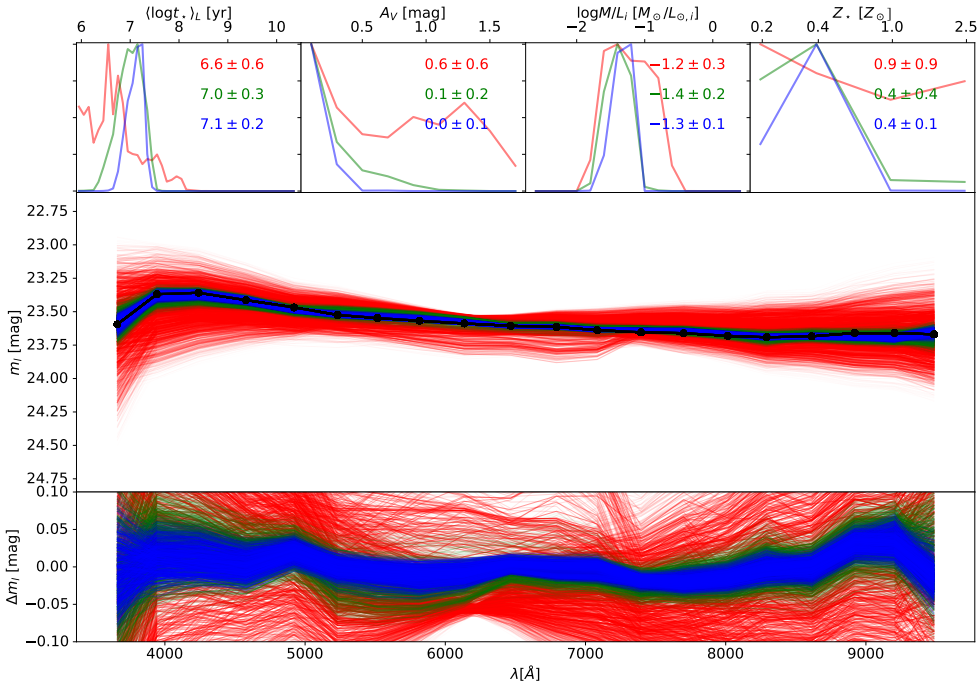

FIGURE 3.7 Output of the MCMC fit for the 1st template from the top in Fig. 3.1. The top panels show the PDFs for mean age, extinction, mass-to-light ratio and metallicity with their average and standard deviations indicated. Blue, green, and red colors represent PDFs obtained for $\epsilon = 0.05$, 0.1 and 0.5 mag respectively. The middle panel shows 3000 random fits (1000×3 values of ϵ) also color-coded by ϵ of the magnitudes of the template magnitudes drawn in black. The bottom panel shows the difference between the same 3000 fits and the template magnitudes.

learn about other properties of the galaxy, like its mean age, extinction, and metallicity.

Fig. 3.7 shows results for an example BPZ template, the 1^{st} spectrum from the top in Fig. 3.1. In terms of magnitudes m_l at the ALHAMBRA filters, this template looks like the thick red line in the middle panel of Fig. 3.7. The redshift was fixed at $z = 0$ for this example. The upper boxes show the PDFs of (from left to right): $\langle \log t_\star \rangle$, Υ_i, A_V and Z. Blue, green and red curves in these panels show the PDFs obtained for $\epsilon = 0.05$, 0.1 and 0.5 mag, respectively.

The value of ϵ enters the definition of χ^2_{ijk} (eq. 3.10) through the weights $w_l = 1/\epsilon$. Larger values of ϵ therefore allow the Markov chains to explore larger regions of the parameters space, which in turn leads to larger $\Delta m_l = m_l(\vec{\theta}_k, z_i) - m_l(z_i, T_j)$ model $-$ template differences and vice-versa. This can be seen in the middle panel, where colored lines plot 1000 random subsets of the models generated by the MCMC code while fitting the template colors. Blue, green and red lines correspond to chains using $\epsilon = 0.05$, 0.1 and 0.5 mag, respectively. As expected, the red models are the ones exhibiting a larger dispersion around the template values (black line). The blue lines, on the other hand, are tightly concentrated around the template photometry. The bottom panel shows the $\Delta m_l = m_l(\vec{\theta}_k, z_i) - m_l(z_i, T_j)$ residuals for the same subset of chain parameters used in the middle panel.

While the excellent spectral fits shown in the middle and bottom panels are reassuring, the main results of the analysis are given in the upper panels. The plots show PDFs becoming increasingly broader as ϵ increases, in agreement with our expectations, since the larger ϵ is, the less informative the data are, and thus the least constrained are the parameters. In particular, A_V and Z are practically unconstrained for $\epsilon = 0.5$ mag. The luminosity-weighted mean age $\langle \log t_\star \rangle$ is also considerably affected, but the PDF of the mass-to-light ratio Υ_i does not deteriorate so much. Of course, $\epsilon = 0.5$ mag is too large an error compared to real data. A value ten times smaller, $\epsilon = 0.05$ mag, is more typical for the ALHAMBRA survey (Molino et al., 2014), and indeed, as explained before, is the default value for this thesis. For this level of uncertainty the PDFs show that, at least for this example, Υ_i, $\langle \log t_\star \rangle$, and A_V are all reasonably well constrained. This can be seen by the mean $\pm$ standard deviation values of the PDFs shown in each panel of Fig. 3.7.

In Fig. 3.8 we show the final photometric fits and of $p(\vec{\theta}|z, T)$ for the 11 main BPZ templates, the same ones whose spectra were shown in Fig. 3.1. Blue, green, and red curves again show PDFs obtained for $\epsilon = 0.05$, 0.1 and 0.5 mag. As discussed above, the blue lines are the ones relevant for this thesis. The fits are again shown for $z = 0$. Results for other z's are not significantly different, as shown in appendix A.

Fig. 3.8 demonstrates that the metallicity is not well constrained using photometry alone. This is in agreement with other studies such as Walcher et al. (2008) where, for simulations without any source of noise

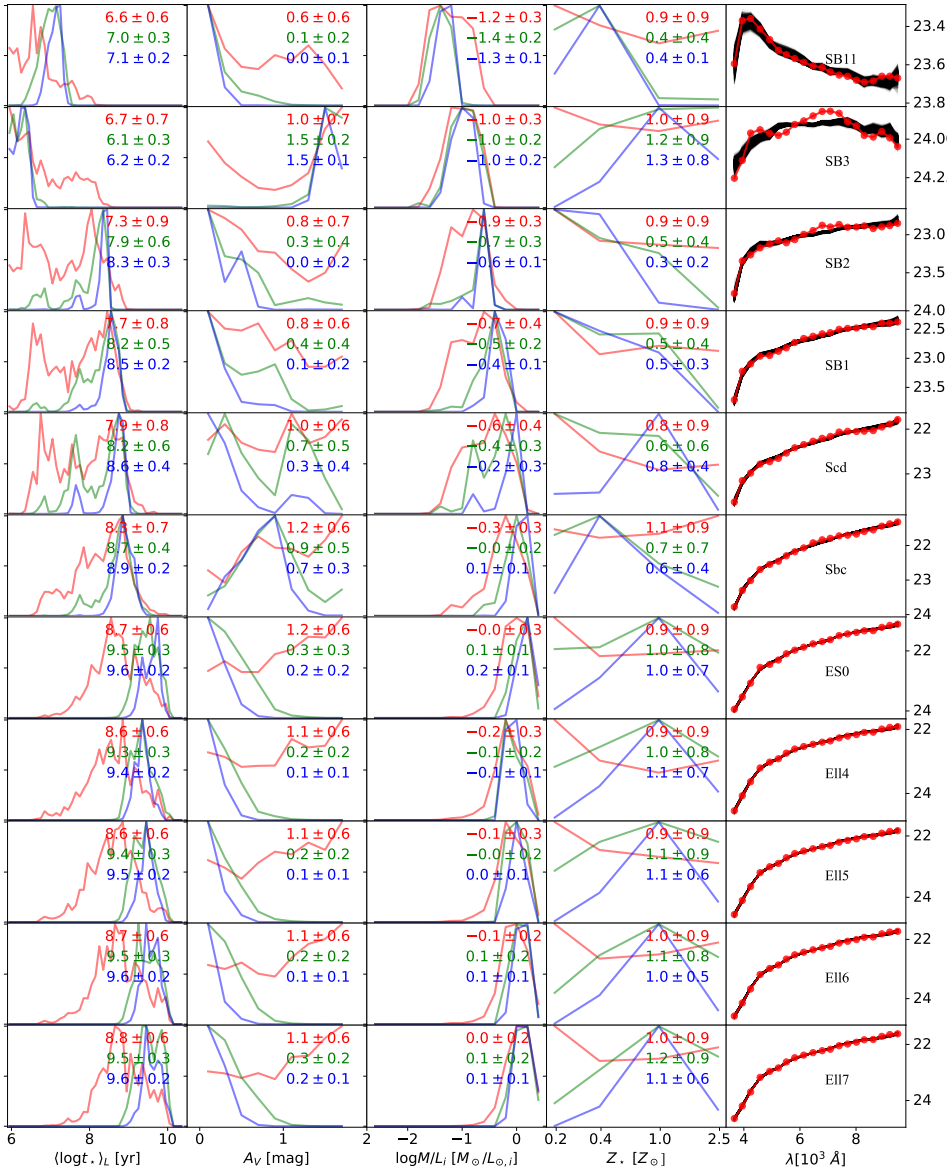

FIGURE 3.8 Output of the MCMC fitting for the 11 templates plotted on Fig. 3.1. Each row shows the PDFs for mean age, extinction, mass-to-light ratio and metallicity with the same color-coding as in Fig 3.7: blue, green, and red curves are $\epsilon = 0.05$, 0.1 and 0.5 mag, respectively. The rightmost panel shows the fit of the template (in red) with also 1000 models drawn in grayscale.

added, the metallicity is not well recovered from photometric data. The simulations in the appendix confirm this.

Mean ages and extinction, on the other hand, are reasonably well constrained in most cases. For $\epsilon = 0.05$ mag, the typical uncertainty in $\langle \log t_\star \rangle$ is 0.2 dex, as measured by the standard deviation of its PDF. The worst case is that in the fifth panel from the top, where the 0.4 dex uncertainty reflects a bimodal PDF. Uncertainties in A_V are in the 0.1–0.2 mag range, except, again, for the fifth template from the top, which shows a bimodal PDF(A_V). As ϵ increases the PDFs of both $\langle \log t_\star \rangle$ and A_V broaden, becoming essentially useless for $\epsilon = 0.5$ mag (red curves).

Mass-to-light ratios are well constrained, with a typical uncertainty of 0.1 dex for $\epsilon = 0.05$ mag. Unlike for $\langle \log t_\star \rangle$ and A_V, the PDF of Υ_i does not deteriorate dramatically as ϵ increases. This can be explained by a fortunate coincidence that an error in age is counterbalanced by an error in extinction in the opposite direction, keeping the mass-to-light ratio approximately stable. This point is extensively discussed by Taylor et al. (2011).

The only noticeable problem found in the fitting of the templates is that the SB3 (2^{nd} template from the top) has a pretty bad fit, leading to an age that is the youngest possible and a maximum A_V.

If we look at the spectrum of this template in detail we see virtually no continuum and prominent emission lines. After removing the emission lines from the spectrum there is not much information left on it. Although this template is useful to constrain the redshift of galaxies (due to its emission lines) its stellar populations' information is limited due to its almost inexistent continuum. Furthermore, in the ALHAMBRA gold catalog less than 1% of the 98017 objects use this template as best choice to fit z, so that it has a very limited impact on our analysis.

3.6 Stellar masses

As discussed in §3.2 (see discussion leading to eq. 3.7), the method described above recovers only the intensive physical properties of galaxies, like Υ_X. This is because we have deliberately ignored the actual flux scales by dealing only with colors.

To recover an extensive properties like $M_\star$ one must know the galaxy's intrinsic luminosity L_X[6]. BPZ provides a calibrated absolute magnitude for each galaxy as a function of the redshift and spectral type on the Johnson *B*-band filter $M_B(z_i, T_j)$. This can be easily converted to the luminosity of the galaxy by the relation:

$$L_B(m_0, z_i, T_j) = 10^{-0.4(M_B(m_0, z_i, T_j) - M_{B,\odot})} \tag{3.24}$$

[6] L_X is the luminosity of a galaxy on the filter *X* in units of $L_{X,\odot}$, the solar luminosity in the X band.

which gives L_B in units of $L_{B,\odot}$. This can then be used in combination with the mass-to-light ratio Υ_B to compute the stellar mass:

$$M_\star(m_0, z_i, T_j) = \Upsilon_B(z_i, T_j) L_B(m_0, z_i, T_j) \tag{3.25}$$

The PDF of $M_\star$ is obtained from the PDF of $\Upsilon_B(z_i, T_j)$ and the $L_B(m_0, z_i, T_j)$ relation given in eq. 3.24. In practice, the procedure is the following:

1. For fixed z_i and T_j, convert $p(\Upsilon_B|z_i, T_j)$ to $p(M_\star = \Upsilon_B L_B|z_i, T_j)$. The resulting PDF is identical in shape to that shown in the third column of Fig. 3.8), but the x-axis is shifted by $+\log L_B / L_{B,\odot}$.
2. Resample $p(M_\star|z_i, T_j)$ to a pre-defined grid of $M_\star$ values. This purely technical step is necessary because the $M_\star$ axis scales with L_B, which varies for each (z_i, T_j), and we will need to combine all PDFs.
3. Add up the $p(M_\star|z_i, T_j)$ for all pairs (z_i, T_j), weighting in by the BPZ-given $p(z_i, T_j|\vec{C}, m_0)$.

This gives us the probability of the stellar mass being $M_\star$ given the data, $p(M_\star|\vec{C}, m_0)$, the primary goal of our whole analysis.

3.7 Example applications

To close this chapter, we apply our method to two low-z galaxies from the ALHAMBRA gold catalog Molino et al. (2014). Figs. 3.9 and 3.10 show two examples of galaxies fitted by our method, one Spiral and one Elliptical. The left panels show on top the RGB composite image of the galaxy and the outputs of BPZ, $p(z)$ and $p(T)$ (in the middle and bottom panels, respectively). The right panels show the PDFs of (from top to bottom) the stellar mass, the mass-to-light ratio, the (luminosity weighted) mean logarithmic stellar age, and the extinction, as obtained with the method presented in this chapter. Metallicities are not shown as they are too uncertain.

Fig. 3.9 shows an example of an elliptical galaxy with a redshift of $z = 0.242 \pm 0.014$ with a quite broad template PDF distribution. Although $p(T)$ is broad, the mass-to-light ratio ($\log \Upsilon_i[M_\odot/L_{i,\odot}] = 0.0 \pm 0.1$) and, hence, the stellar mass ($\log M_\star[M_\odot] = 10.5 \pm 0.1$) is very constrained, with a dispersion of ± 0.1 dex. This is expected, as the mass-to-light ratio distributions are very similar for those templates, as seen in fig. 3.8. As also expected for these "elliptical-galaxy" templates, the stars are old ($\langle \log t \rangle_L[yr] = 9.5 \pm 0.2$) there is little extinction ($A_V = 0.1 \pm 0.2$ mag).

On the other hand, in Fig. 3.10 we show a typical startburst example at $z = 0.120 \pm 0.012$, with younger stellar populations ($\langle \log t \rangle_L[yr] = 8.4 \pm 0.5$), extiction of $A_V = 0.5 \pm 0.4$, stellar mass $\log M_\star[M_\odot] = 9.4 \pm 0.3$ and Υ_i about half the value for the elliptical galaxy in the previous example. The starburst-like templates (the 5 first templates from top to bottom on

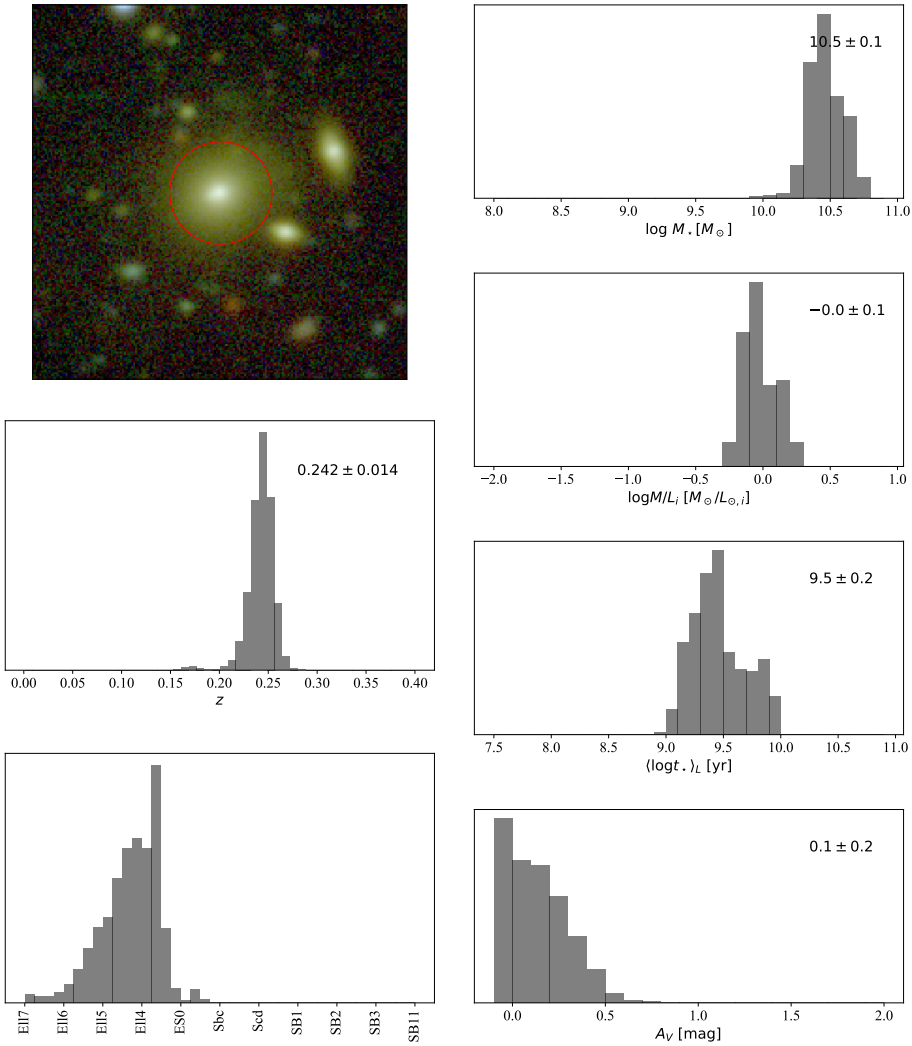

FIGURE 3.9

A typical elliptical galaxy example. From top to bottom in left panels we show an RGB image of the galaxy, the redshift and template PDFs, $p(z)$ and $p(T)$. On the right panels, we show the stellar mass, the stellar mass-to-light ratio, average age, and extinction. Values labeled inside each panel indicate the mean $\pm$ standard deviation of the corresponding PDF.

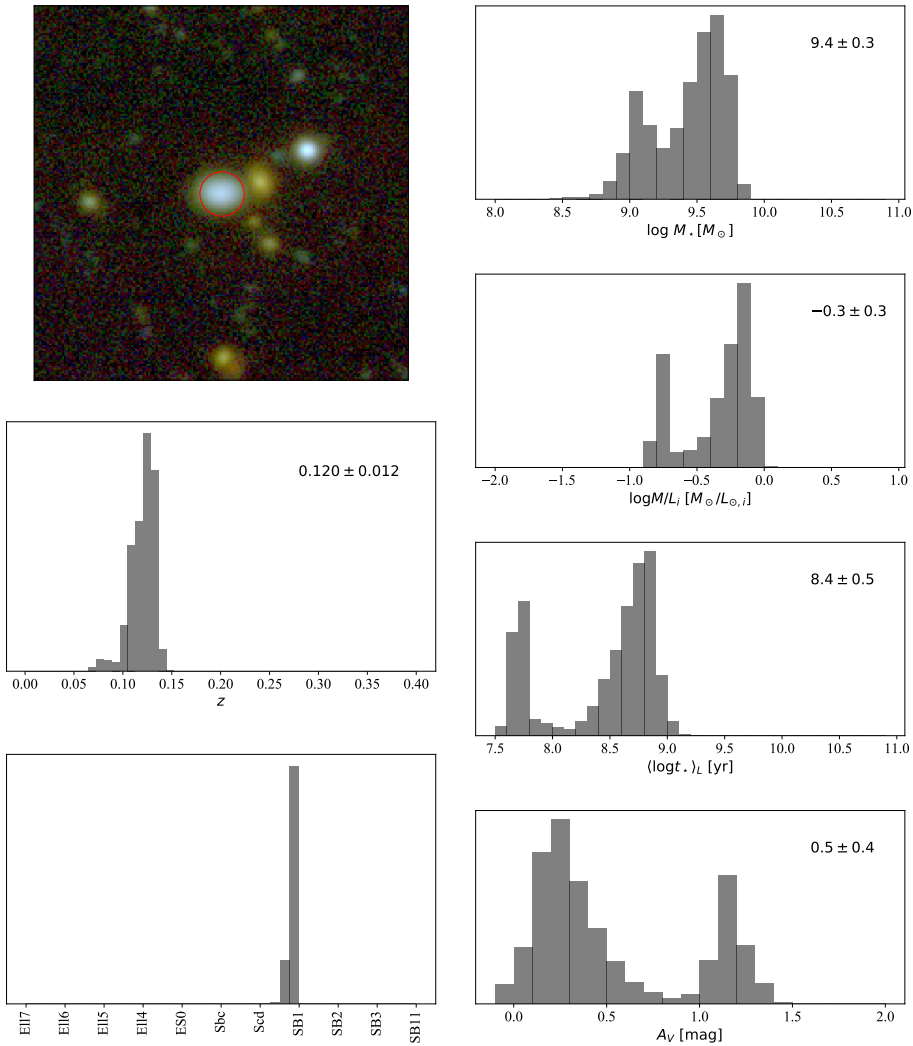

FIGURE 3.10 As in Fig. 3.9 but for a Starburst galaxy with two templates in p(T) which leads to a bimodal distribution in the stellar parameters.

Fig. 3.8) span a wider range of values on their stellar properties than the elliptical galaxies (up to 1 dex in age, compared to 0.2 dex for the elliptical templates, for instance), so the template PDF $p(T)$ plays a critical role. In Fig. 3.10 we see that the distribution in the template space comprises only two templates, much narrower than the elliptical one, but since they are very different in their parameters distributions, the final mass distribution is very broad, with ± 0.3 dex of dispersion. The two templates that compose the $p(T)$ (Scd and SB1) have such different stellar properties (see in detail in Fig. 3.8) that their contribution to the object's stellar population parameters summed with the redshift PDF $p(z)$ produces a bimodal distribution.

Looking at these two examples and the stellar properties PDFs shown in Fig. 3.8, it is expected that the uncertainty on the parameters is bigger for galaxies fitted by BPZ with starburst templates than the others.

We have applied the same methodology to the whole ALHAMBRA gold catalog, producing estimates of their stellar masses, ages, and extinction for 98017 galaxies. The results of this analysis are presented in the next chapter.

Chapter Four

The stellar mass function of ALHAMBRA galaxies

In this chapter we apply our method to estimate stellar properties of galaxies out of photometric data to the ALHAMBRA survey, focusing on results related to the stellar mass ($M_\star$). We first characterize the sample in terms observational properties and BPZ-based redshifts. Then we investigate how stellar masses, mean ages and extinction are distributed and correlated in the sample. Finally, after defining volume corrections factors, we present our results for the galaxy mass function in ALHAMBRA and its evolution between $z = 0.7$ and 0.

4.1 Introduction

The method introduced in the previous chapter combines the output of a Bayesian photo-z code with a stellar population modeling of the spectral templates used by the code to estimate properties such as the stellar mass, mean age and extinction in a galaxy. The method is very flexible. Although we have only worked with the BPZ templates, other templates can be straightforwardly incorporated into the analysis. Also, although we made only a very simple stellar population modeling (following the widely used "tau-models", where star formation histories are described by exponentially decaying functions of time), this analysis too can be easily extended to more complex models. For instance, one may implement superpositions of two or more $\Psi(t) \propto e^{-(t-t_0)/\tau}$ exponential bursts, with random dates and decay times. Alternatively, instead of working with these ad-hoc mathematical recipes one may use $\Psi(t)$ functions extracted from suites of detailed simulations of galaxy evolution (as done, for instance, by Pacifici et al. (2016)).

In short, there are plenty of ways to improve the ingredients used in our method. The method itself, however, would remain exactly the same. The only added complication would be that more complex stellar population models would require longer computational times to converge, but this is a one-off effort, since the templates only need to be fitted once. Once that is done, the resulting $p(\vec{\theta}|z, T)$ probability distribution

funcions are fixed and available to estimate stellar properties using just the output of BPZ or any other similar code.

Improvements along the lines discussed above are certainly interesting, but we will leave them for future work. In this section, we want to illustrate the use of our method by applying it to data from an actual survey, the ALHAMBRA survey. Examples of stellar properties for individual ALHAMBRA galaxies were in fact given at the end of chapter 3 (Figs. 3.9 and 3.10). Here we will apply it to all galaxies in the sample and explore the results in a statistical way.

In order to have a well defined goal, we will focus on the stellar mass $M_\star$ and use our results to estimate the stellar mass function of ALHAMBRA galaxies. Specifically, we want to obtain the number of galaxies at redshift z and of mass $M_\star$ per unit volume and logarithmic mass interval:

$$\Phi(M_\star, z) = \frac{dN}{dV d\log M_\star} \tag{4.1}$$

With the surge of panchromatic photometric and spectroscopic all-sky surveys in the past two decades, the available data to constrain the stellar mass function (MF) of galaxies had a massive increase. Recent studies on the galaxy MF include Cole et al. (2001); Hogg et al. (2002); Bell et al. (2003); Blanton et al. (2003); Panter et al. (2004); Bundy et al. (2006); Fontana et al. (2004, 2006); Pozzetti et al. (2007); Baldry et al. (2008); Walcher et al. (2008); Drory et al. (2009); Ilbert et al. (2010); Pozzetti et al. (2010); Bernardi et al. (2013); Muzzin et al. (2013); Davidzon et al. (2013); Szomoru et al. (2013); Maraston et al. (2012); Baldry et al. (2012); Moustakas et al. (2013); Wild et al. (2014). These studies employ data from surveys such as COMBO-17, COSMOS, UltraVista, SDSS, VIPERS, zCOSMOS, S-COSMOS, VVDS, HST/CANDELS, BOSS, SWIRE, GALEX, CFHTLS, PRIMUS, GOODS-MUSIC and K20, spaning from the local Universe to high redshift and covering almost all ranges of the electromagnetic spectrum.

Fig. 4.1 shows two examples of stellar MFs from the literature. The left panel, extracted from Baldry et al. (2008), shows the local mass function (i.e. $z < 0.1$) as derived by different authors from the 2dF Galaxy Redshift Survey plus 2MASS data in the case of Cole et al. (2001) and from SDSS data (using both spectroscopy and photometry) in the others. The figure shows the familiar Schechter-like shaped curve (Schechter, 1976), similar to the galaxy luminosity function, with few high mass galaxies and many low mass ones, with a knee around $\approx 10^{11} M_\odot$. The right panel, extracted from Ilbert et al. (2010), shows the results of Fontana et al. (2004, 2006); Bundy et al. (2006); Borch et al. (2006); Pozzetti et al. (2007), who computed the MFs for higher redshift bins using data from various sources from ESO/VLT to Hubble ACS. Note that the actual data points (open circles) sample progressively smaller mass ranges as z increases due to completeness effects.

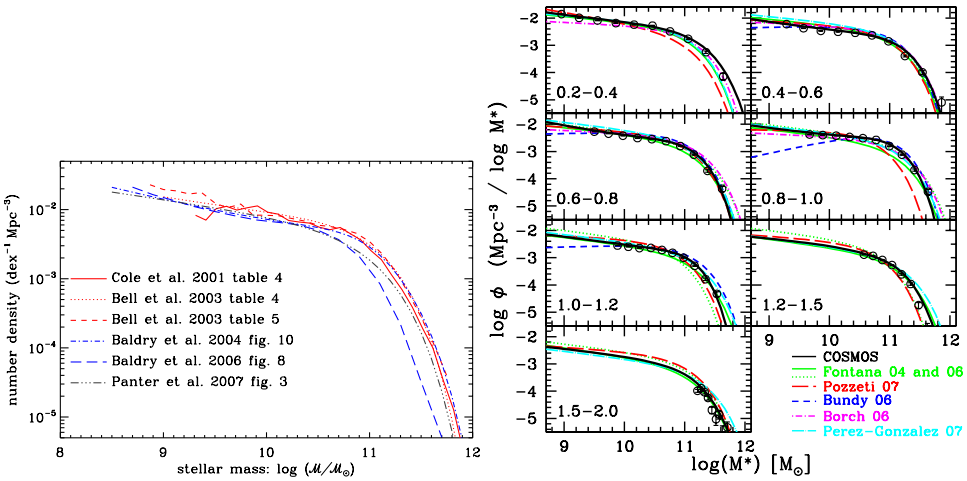

FIGURE 4.1 Left: The MF for galaxies in the local Universe ($z < 0.1$) obtained from the SDSS survey. Extracted from Baldry et al. (2008). Right: The evolution of the MF from $z = 2.0$ to the present as derived from the COSMOS survey. Extracted from Ilbert et al. (2010).

The mass function is important to understand star formation and galaxy evolution and estimate the baryonic mass fraction Ω_M of the Universe. It helps to constrain models of galaxy star formation and evolution trough the cosmic time.

This chapter is organized as follows. §4.2 describes the ALHAMBRA data used in this study, including observed and BPZ-derived properties. In §4.3 we present the results of the application of the method developed in chapter 3 to the ALHAMBRA data. Histograms of the stellar mass, mean age and extinction are shown, as well as correlations among these properties. From then on we focus on the stellar mass $M_\star$ and its distribution. Effective volumes are discussed in §4.4 and used in §4.5, where we present our results for the galaxy mass function, the main goal of this study. §4.6 discusses our results, compares them to those in the literature, and outlines directions for future work.

4.2 The data: ALHAMBRA gold catalog description

As reviewed in chapter 1, the ALHAMBRA survey observed a total of $2.79 \mathrm{deg}^2$ split into 8 fields, observed through 21 $\sim$ 300 Å-wide optical filters plus J, H and Ks on the near infrared. The survey was originally presented in (Moles et al., 2008), and its photo-z efficiencies were simulated in Benítez et al. (2009b). The final photo-z catalog was published by (Molino et al., 2014) and used by (López-Sanjuan et al., 2016) to estimate

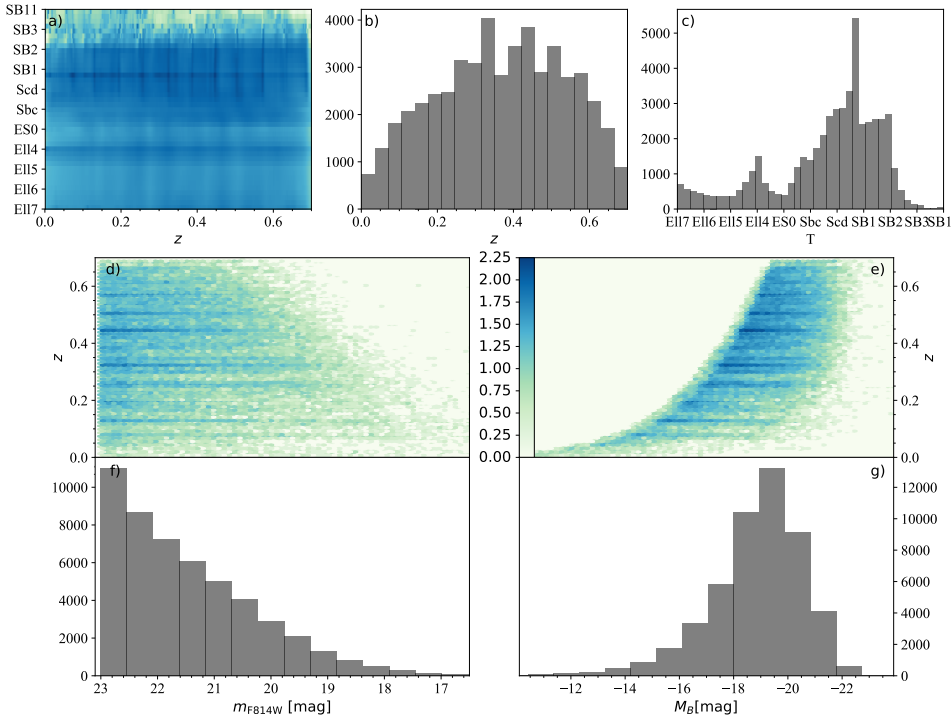

FIGURE 4.2

ALHAMBRA gold sample object distributions. In panel (a) the redshift versus template frequency with its projections in redshift in the histogram of panel (b) and template in panel (c). In panel (d) the distribution of galaxies in apparent magnitude m_{F814W} versus redshift and its projection in magnitude on panel (f). Panels (e) and (g) shows the same of panels on the left but for the absolute rest-frame B magnitude M_B. The colors of the density plots (a), (d) and (e) represent the logarithm of the number of the objects in each bin log N and its scale is given by the colormap in panel (e).

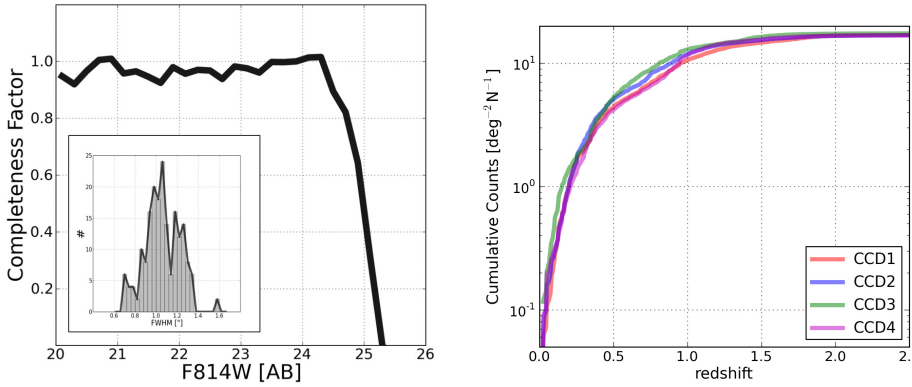

FIGURE 4.3 Left: ALHAMBRA gold simulated completeness versus apparent magnitude in F814W filter. Right: cumulative galaxy counts versus redshift for each ALHAMBRA CCD. Figure extracted from Molino et al. (2014).

the luminosity function (defined as eq. 4.1, but for galaxy luminosity instead of mass.)

We will focus our analysis on the so called ALHAMBRA gold catalog described in §4.2, which is defined as a sub-sample of the ALHAMBRA survey with the most accurate redshifts ($\sigma_z < 0.012$) and with the redshift probability $p(z)$ defined by a single peak in the magnitude range of $17 < m_{F814W} < 23$. The ~ 100000 galaxies in this sample were processed through BPZ using the same templates discussed in the previous chapter. As discussed there, BPZ produces PDFs for redshift z and spectral type (T) for each galaxy, as well as PDFs for its absolute magnitude in any desired band. After the cut in $z < 0.7$, we get a final sample of 50311 objects.

Fig. 4.2 presents some global information on the sample. Panel (a) shows a 2-dimensional representation of the template-redshift probability $p(z, T)$ with its projection over z on panel (b) and over T in panel (c). The object apparent magnitude m_{F814W} in the F814W filter distribution versus z is shown in panel (d) while its total counts per magnitude bin are shown in panel (f). The absolute rest-frame B magnitude versus z is shown on panel, (e) while their total counts per magnitude bin are shown in panel (g). For simplicity, in these figures, each galaxy is represented by a point, instead of a PDF.

Fig. 4.3, extracted from (Molino et al., 2014), shows the completeness of the ALHAMBRA survey. On the left panel, the completeness factor versus magnitude is shown. On the right panel, we show the cumulative counts of the ALHAMBRA galaxies versus redshift for the four CCDs on the LAICA mosaic. The survey completeness factor of fig. 4.3 was

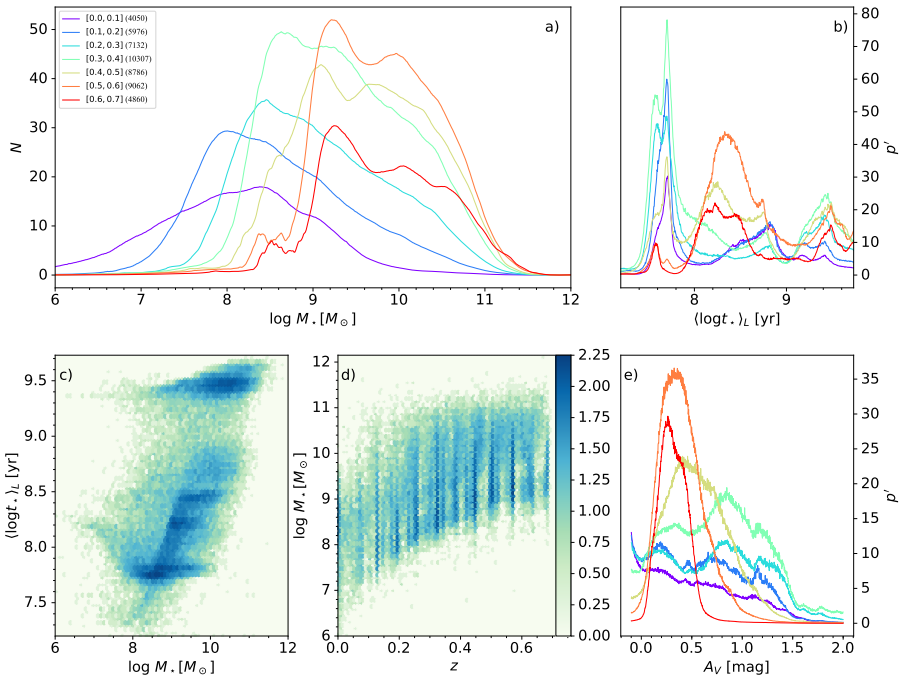

FIGURE 4.4 ALHAMBRA gold derived physical properties. Panels (a), (b) and (e) shows the distribution of the $\log M_\star$, $\langle \log t \rangle_L$ and A_V for redshift bins from 0 to 0.7 with 0.1 intervals shown with colors from blue (low z) to red (high z) with the redshift bin ranges and number of objects in each bin shown in the legend of (a). Panel (c) shows the $M_\star$ versus $\langle \log t \rangle_L$ sample density physical color-magnitude diagram and panel (d) shows the $M_\star$ versus z sample density. On panels (c) and (d), for simplicity, we show each galaxy as the average of its PDF while in panels (a), (b) and (e) we show the sum of the probability on a certain bin of the property in a given z range.

calculated by using HST imaging in the same fields as ALHAMBRA. Objects were binned in intervals of m_{F814W} and the completeness per magnitude range is estimated by the ratio of the detection counts in the ALHAMBRA survey with the detection counts in the (much deeper) HST data (Molino et al., 2014). In this thesis we limit the completeness on $m_{F814W} > 23$.

4.3 Stellar properties

Applying our method to the 50311 galaxies in our sample gives us PDFs for $M_\star$, $\langle \log t \rangle_L$ and A_V. Fig. 4.4 offers a first look at the results. In panel (a) we show the histogram of the stellar mass, the primary property of interest. The histogram is broken in different ranges of redshift, represented with colors from blue for $z \sim 0$ to red for $z \sim 0.7$. The plot shows that the mean $M_\star$ increases with z, but this is a direct effect of the magnitude limit of the sample, which leads to the exclusion of low mass galaxies at higher distances. Low mass galaxies are therefore progressively under-represented as z increases. This raw luminosity function will be corrected for selection effects in the next section.

In panels (b) and (e) we show raw histograms for the mean log. stellar age $\langle \log t \rangle_L$ and extinction A_V, respectively. The distribution of ages has a surprisingly large peak at $\langle \log t \rangle_L \sim 7.5$. This is a direct consequence of the high frequency of usage of template SB1, as seen in Fig. 4.2c.

In Fig. 4.4c we show the mass versus age plot. This is a physical analog of the observational color-magnitude diagram of galaxies (Bell et al., 2004; Baldry et al., 2004), where absolute magnitude and color play the role of proxies for the stellar mass and mean stellar age, respectively. The familiar red-sequence + blue-cloud pattern is visible in this diagram. Again, however, the large probabilities attributed by BPZ to SB1 and other late-type templates introduces distortions in the way galaxies populate this diagram. The unexpected concentration of points around mean ages of ~ 50 Myr is a consequence of the fact that BPZ fits have a strong preference for the templates SB1 and Scd, as seen in Fig. 4.2a and c.

In Fig. 4.4d we show the distribution of galaxies in the stellar mass versus redshift plane. There seems to be a gap in $M_\star$ for fixed z. Again, this is a result of SB-like templates, which have large mass-to-light ratios (see Fig. 3.8).

This first assessment of the results looks both promising and worrying. On the one hand, we are able to obtain a mass-age relation which is qualitatively in agreement with what is known about galaxies in general. On the contrary, however, the results seem to be quantitatively offset, with ages which are too young to be real whenever the SB templates are given significant weight by BPZ. Old, red, early type galaxies are immune to this problem, but others are not. This point is examined again in the final section of this chapter.

4.4 Effective volumes

To reach our main goal of deriving a mass function for ALHAMBRA galaxies we have to convert the raw counts of galaxies in bins of $M_\star$ (as shown in Fig. 4.4) to the number density of galaxies of a given stellar mass. This requires defining a volume for the sample. Further-

more, given the substantial redshift range spanned by ALHAMBRA this must be done breaking up the sample in z-bins, so we seek to compute $\Phi(M_\star, z)$, as defined in eq. 4.1. The discrete version of eq. 4.1 is

$$\Phi(M_\star, z) = \frac{dN}{dV d\log M_\star} = \frac{\Delta N(M_\star, z)}{\Delta V_{eff} \Delta \log M_\star} \tag{4.2}$$

where $\Delta N(M_\star, z)$ is the number of galaxies in a given bin in log mass and redshift, $\Delta \log M_\star$ is the width of the bin in log mass, and ΔV_{eff} is the cosmic volume effectively sampled by the data.

Evaluating ΔV_{eff} is a non-trivial exercise, as in practice $\Delta V_{eff} = \Delta V_{eff}(z, M_\star)$, i.e., it depends both on z and $M_\star$. The dependence on z is actually simple. For a solid angle Ω (the survey area), the cosmic volume between z and $z + dz$ is

$$dV(z) = D_H \frac{(1+z)^2 D_A^2}{E(z)} \Omega dz \tag{4.3}$$

where D_A is, for a flat ΛCDM Universe,

$$D_A = D_H \int_0^z \frac{dz'}{E(z')} \tag{4.4}$$

$E(z)$ is

$$E(z) \equiv \sqrt{\Omega_M (1+z)^3 + \Omega_k (1+z)^2 + \Omega_\Lambda} \tag{4.5}$$

and $D_H = \frac{c}{H_0}$ is the Hubble distance.

$H_0, \Omega_M, \Omega_k, \Omega_\Lambda$ are the cosmological constants and c is the speed of light in the vaccuum. As in Molino et al. (2014), we adopt a flat ΛCDM cosmology with $H_0 = 70 km s^{-1} Mpc^{-1}$, $\Omega_M = 0.3$ and $\Omega_\Lambda = 0.7$. For a redshift bin running from z_l to z_u one simply has to integrate this expression to obtain the corresponding cosmic volume in the bin (Hogg, 1999, and references therein):

$$\Delta V(z) = \int_{z_l}^{z_u} \frac{dV}{dz} dz = \Omega D_H \int_{z_l}^{z_u} \frac{(1+z)^2 D_A^2}{E(z)} dz \tag{4.6}$$

For example, for z between $z_l = 0.2$ and $z_u = 0.3$ and for the area covered by ALHAMBRA, the cosmic volume is $\Delta V(z = 0.25) = 3.28 \times 10^5$ Mpc^3.

One must, however, account for selection effects. Given the magnitude limited nature of the sample, we are bound to miss galaxies. The ALHAMBRA gold sample is complete to $m_{F814W} = 23$, meaning that all galaxies brighter than 23 in the (observed-frame) F814*W* band are accounted for, so the volume really accessible in a z-bin depends on $M_\star$. At a fixed z, this implies an upper limit in absolute magnitude (or a lower limit in luminosity), and thus to a lower limit in $M_\star$, so that low stellar mass galaxies will be differentially missed. To account for missed galaxies, let us define the effective volume as

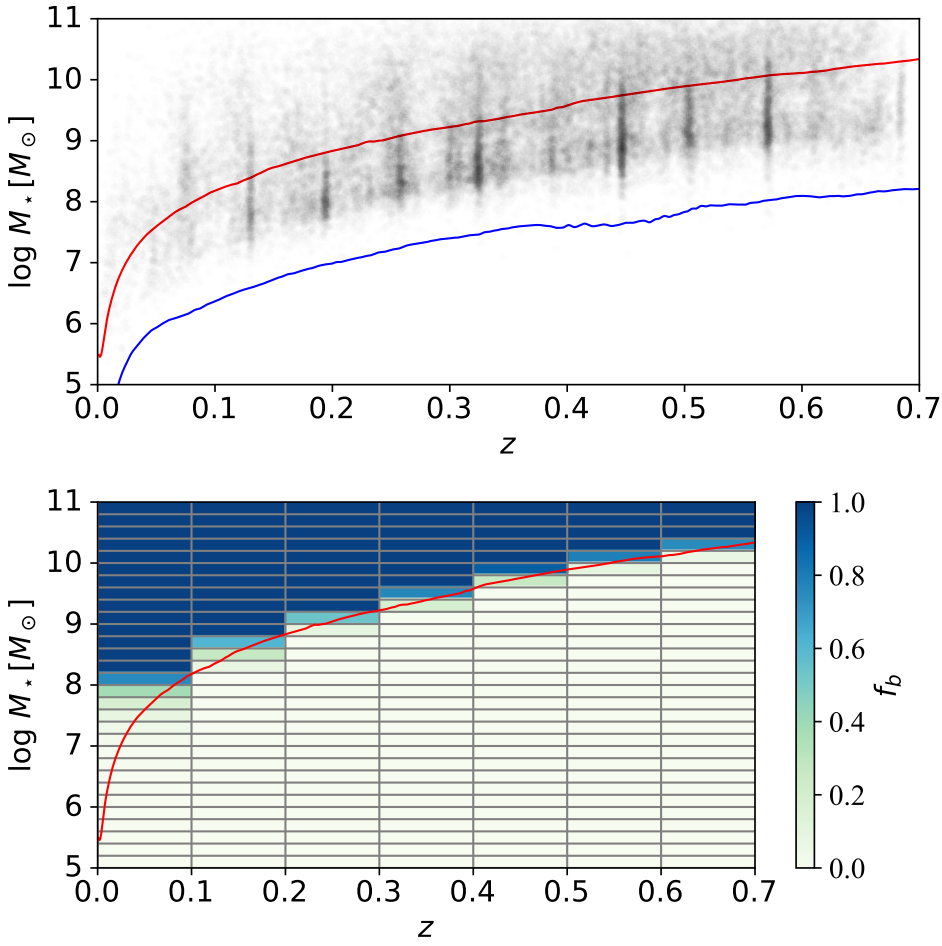

FIGURE 4.5 z vs $\log M_\star$ sampling. Top panel: Distribution of objects of the sample in black, the maximum $\log M_\star$ for a galaxy with apparent magnitude $m_{F814W} = 23$ plotted in red and the minimum mass for the same magnitude in blue. Bottom: Bins in the mass-redshift space with in each bin the value of f_b.

(4.7) $$\Delta V_{eff}(M_\star, z) = f(M_\star, z)\Delta V(z)$$

where $\Delta V(z)$ is the cosmic volume of eq. 4.6, and f is a correction factor between 0 and 1.

In the top panel of Fig. 4.5 we show the distribution of objects of our sample in the stellar mass versus redshift space. The red and blue curves

are, respectively, the most and least massive BPZ template for a limiting magnitude of $m_{F814W} = 23$. We will use the most massive one to define the completeness limit. This will be done in bins of size $\Delta \log M_\star = 0.2$ dex and $\Delta z = 0.1$ in the $\log M_\star$-z plane.

In the bottom panel of Fig. 4.5 we show the completeness correction factor f in our $\log M_\star$ and z grid. For galaxies in bins well above the completeness curve, (those painted in dark blue in fig 4.5) no correction is necessary, so $f = 1$. For those well below the curve, no galaxy is counted, as they belong to a non-complete region of the survey, and, therefore $f = 0$. For those bins which are intercepted by the completeness curve, a correction factor must be applied to take in account the missed galaxies. This correction factor is equal to the fraction of the area of the bin which lies above the curve.[1]. Note that, as z decreases, more bins need to be corrected for the missing objects ($0 < f_b < 1$).

4.5 The stellar mass function of ALHAMBRA galaxies

Joining the methodology to obtain stellar masses presented on chapter 3 and the method to calculate the effective volume seen by the ALHAMBRA survey presented in previous sections of this chapter, we can calculate the final stellar mass function for the survey. As indicated above, we evaluate $\Phi(M_\star, z)$, given by equation 4.2, counting galaxies in a $M_\star$-z grid and dividing by the corresponding effective volume.

The mass function for all bins of redshift is shown in fig. 4.6. In the top panel, we show the 3-dimensional representation of the mass function on the plane $\log M_\star$ versus z. As in fig. 4.5, the red line is the stellar mass limit line that divides the masses of galaxies belong to the complete part of the survey of those who are not. The galaxies below this mass limit are discarded, reducing the size of our sample from 50311 galaxies to 20846.

In the bottom panel of fig. 4.6 we show the mass function obtained for all our seven redshift bins. The number of objects in each bin is shown in the legend. We marked with stars the bins that had been corrected by the correction factor described in § 4.4, i.e. $0 < f < 1$. As commented earlier, the number of bins corrected is bigger for lower redshifts.

In fig. 4.7 we show the same curves of the bottom panel of fig. 4.6, but separated, each one in one box. For comparison, we plotted the Schecter fits for the total MF calculated by Ilbert et al. (2010). It is evident that the estimated $\log \phi$ is different from those found in the literature. Ilbert et al. (2009) finds that the difference between their MF fit and others in the literature (see right panel of fig. 4.1) is 0.2 dex or lower in the high mass end, while ours compared to it gives values larger than that. Also,

[1] Although we plotted the bins and curves in z versus mass space plane for clarity, the calculation of the area above the completeness curve must be done in the cosmic volume versus mass space, i.e. $V(z)$ versus $M_\star$.

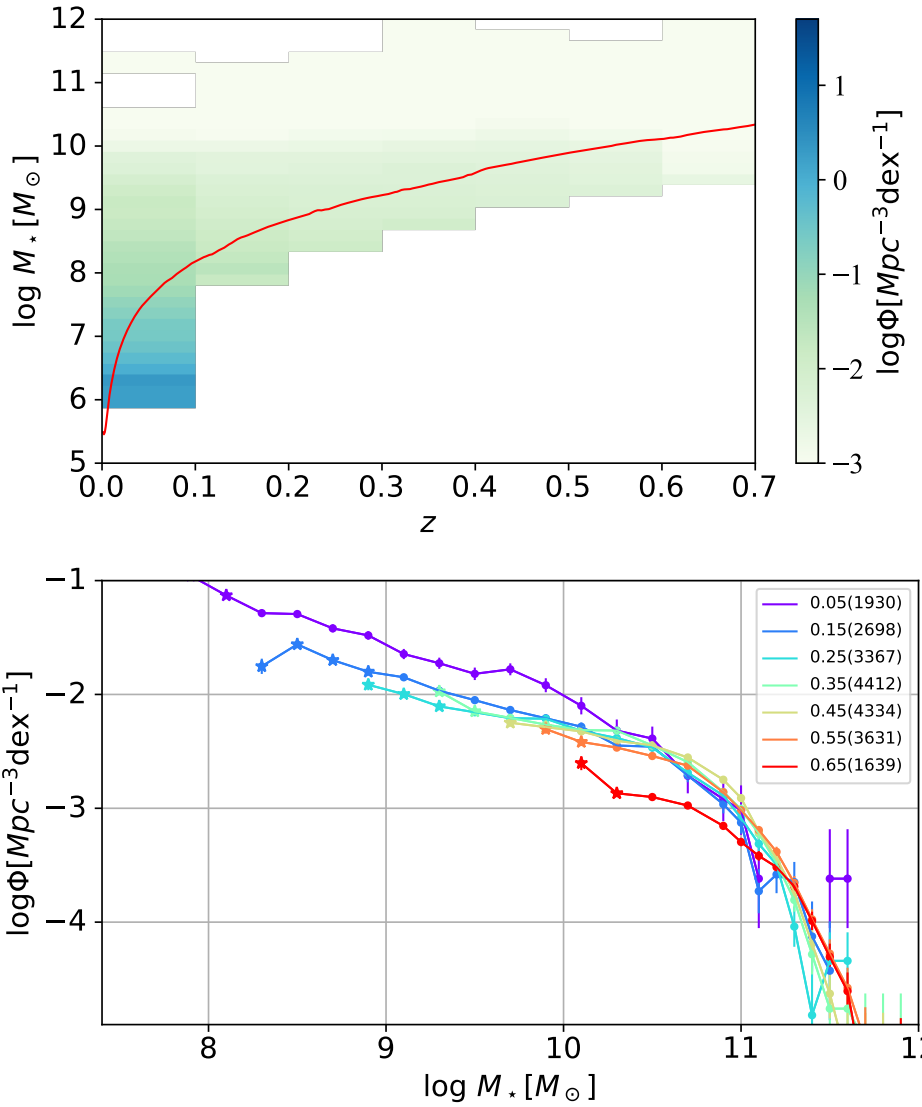

FIGURE 4.6 Top: ALHAMBRA gold stellar MF for each bin in redshift and stellar mass. The red curve is the limiting mass where the objects are considered in the sample or not. Bottom: The MF versus stellar mass for bins in redshift varying from 0 in blue to 0.7 in red. Points marked with stars correspond to bins that have $0 < f < 1$.

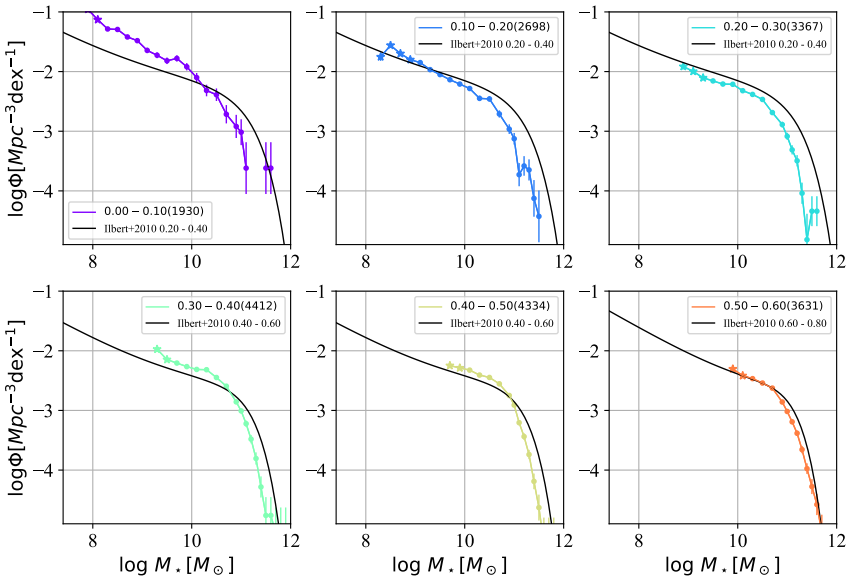

FIGURE 4.7 ALHAMBRA mass functions in redshift bins. The black line is the double Schecter function fit for the MF of Ilbert et al. (2009).

in the lower mass region, where generally there is a good agreement between different works, our MF is overestimated on almost all bins of redshift. Overall, although our results fall in the same "ballpark" as other estimates, the differences are substantial and larger than the formal uncertainties, calculated from the square root of $\Delta N(M_\star, z)$. It is unclear if the differences are mostly along the x-axis, and thus related to the estimates of $M_\star$, or along the y-axis, and thus refers to the galaxy number densities. In the next section, we will discuss further these problems of the mass function, their possible causes and how to address them.

4.6 Discussion

As seen in Fig. 4.7, our stellar MFs have approximately the same general appearance of MFs found in the literature, but with differences too large to be explained only by the statistical errors in stellar mass, which, as found in chapter 3, are of the order of 0.1–0.2 dex. Differences in the low redshift bins (i.e. $z < 0.2$) are not worrisome and will not be taken too seriously. Given the small survey area, the cosmic volumes at low redshift lead to cosmic variances that can reach 30% (Moster et al., 2011).

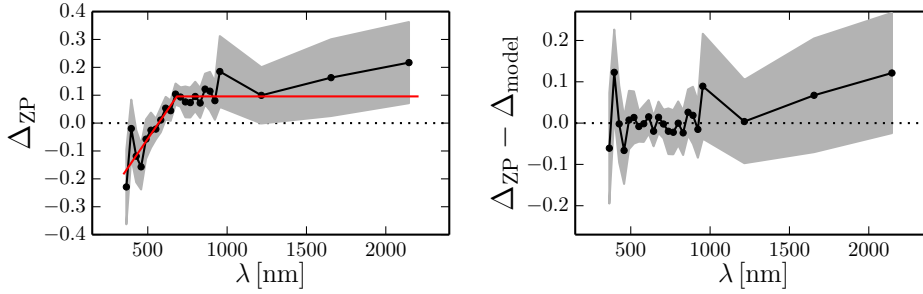

FIGURE 4.8 Left: Median zero point correction estimated by Molino et al. (2014). The red line is the color correction factor of the zero point Δ_{model} calculated by López-Sanjuan et al. (2016). Right: The "corrected" zero points for the ALHAMBRA survey. The gray area in both panels is the dispersion of the correction calculated over the 8 ALHAMBRA fields. Figure extracted from López-Sanjuan et al. (2016).

Indeed Ilbert et al. (2009) show their MFs for the COSMOS survey only for redshift bins of $z > 0.2$.

For the redshift bins of $z > 0.3$–0.4 the cosmic variance effects play a minor role, but still, the discrepancies shown are high enough to be a source of concern. In this case, the most probable source for the offsets between our MF and the literature would be related to systematic offsets on our stellar mass estimates. In §4.3 we have seen some indications that the stellar population properties could be compromised. For example, in Fig. 4.4, we see an anomalous distribution of mean stellar ages, with an overdensity of galaxies with mean ages around 50Myr. This leads to the strange-looking pattern of the blue cloud in the physical CMD drawn in panel (c) of Fig. 4.4. For comparison, Fig. 4.9, extracted from Schoenell (2012), shows the physical CMD obtained for 299.253 galaxies of the SDSS, in the local Universe with stellar properties derived from full spectral fitting by the STARLIGHT code Cid Fernandes et al. (2005). The distribution of galaxies in this diagram looks much smoother than in the diagram seen here. In particular, there are no concentrations around very young ages as that seen in Fig. 4.4b.

As discussed in § 4.3, this anomaly is related to the unusual preference of BPZ to use the SB1 and Sbc templates. A probable cause for those discrepancies is that BPZ templates and priors were calibrated using a sample of galaxies from the Hubble Deep Field North (HDF-N) with a typical redshift of $z \sim 0.5$ (Benítez, 2000). For that reason, there could be an under-representation of early-type templates, characteristic at lower redshifts.

These discrepancies in the PDF shape were seen in other works where the PDF was used besides the primary goal of getting photo-z's. For

example, López-Sanjuan et al. (2016) shown that these biases in the BPZ templates would lead to a color term in the zero points calculated by BPZ. The BPZ zero points for the ALHAMBRA survey were calculated by Molino et al. (2014) following the recipe showed by Coe et al. (2006). First, galaxies that have spectroscopic redshifts and a good signal-to-noise ratio ($S/N > 10$, in all filters) had their magnitudes fit with the BPZ empirical template set. The template that best fits each galaxy is then chosen to be the "correct" template, and the difference between its synthetic magnitude and the observed magnitude in each band is called the zero point. The average zero points and their field-to-field dispersion are shown in the left panel of Fig. 4.8, extracted from López-Sanjuan et al. (2016).

López-Sanjuan et al. (2016) circumvent this color term introduced by BPZ by computing a linear plus constant model, and subtracting it from the zero points calculated by Molino et al. (2014). This correction is shown as the red line in Fig. 4.8 and it is zero for $z > 0.5$ and decreases for redshifts lower than 0.5.

Although the zero points given by BPZ are useful to get high-quality photometric redshifts as shown by, for example, Benítez (2000); Coe et al. (2006); Capak et al. (2007); Hildebrandt et al. (2008); Molino et al. (2014), the color term that it introduces (which can be up to 0.2 mag in the blue filters) should be treated with care.

This factor does not only fine tune the photometric calibration of the survey data, but also corrects for biases and systematics that would be present in the photo-z templates themselves, so this zero point factor plays more a role of a cross-calibration factor between data and photo-z templates than an instrumental zero point correction, as its name suggests.

The artificial preference of BPZ for the mentioned SB templates is induced by the zero point factors, leading to an underestimation of the ages of the galaxies and, by doing that, underestimating the stellar masses. A direct consequence of this can be seen in the stellar MFs of Fig. 4.7, were galaxies migrate from the right, more massive, side of the MF "knee" to the left, less massive, side of it. This effect is more evident in the 0.3–0.4 and 0.4–0.5 redshift bins.

Therefore, the origin of the problems in the whole analysis seems to be traced to the lack of representation of some galaxy types in the BPZ templates. A better set of photo-z templates is expected to alleviate the discrepancies in stellar properties, moving galaxies to their right place in the MF. This makes the method presented in this thesis still useful and, once the templates issue is fixed, the stellar properties should be fixed too.

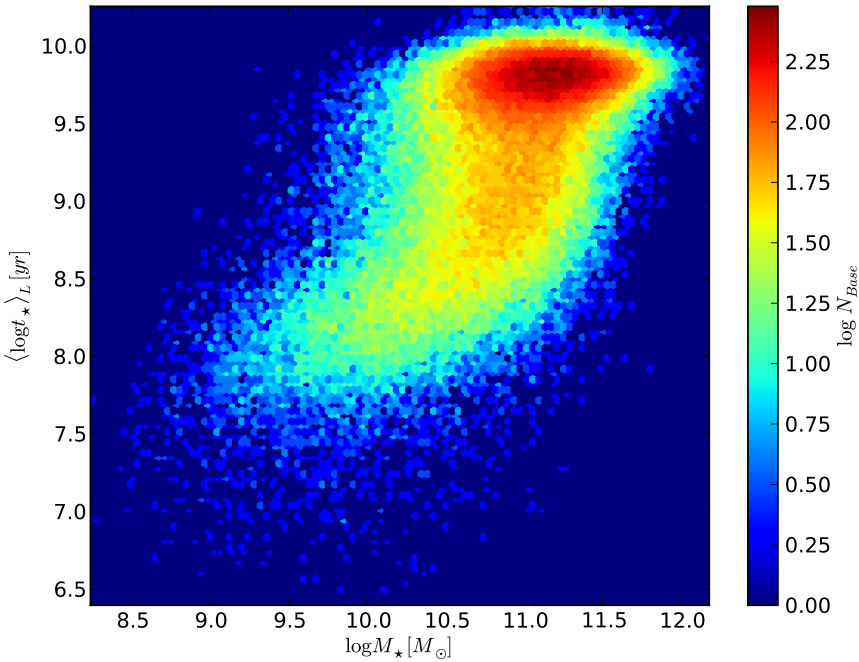

FIGURE 4.9 Physical CMD for a sample of 299.253 galaxies from SDSS. In each pixel, we show the log. number of objects inside it. The stellar properties were derived using the STARLIGHT code Cid Fernandes et al. (2005). Extracted from Schoenell (2012).

Chapter Five

Conclusions and future work

In this chapter, we summarize the conclusions obtained in this doctorate thesis and discuss which will be the next steps to finish the work started here. This thesis presented two parallel works: the project, execution and first light of an 80 cm robotic telescope in the Chilean Andes, as detailed in §2, and a new method for deriving stellar masses and physical properties of galaxies out of their redshift PDF, as described in detail in §3, and its application to the calculation of the stellar mass function, as described in detail in §4.

5.1 Conclusions

For the construction of a new 80 cm telescope in Chile, presented in §2, we can summarize the developments done on the following points:

- Between the years of 2015 and 2016 the T80S telescope and its instrument was installed and commissioned. The instrument has two modes: photometric and polarimetric, and only the photometric was commissioned during the thesis, being the polarimetric mode left for further publication. Together with the telescope and instrument, a dozen of other support peripherals was installed in conjunction with a small data center for local on-line data reduction. We detailed the observatory's telescope and instrument characteristics.

- Since we had total freedom of choice on the hardware that would be installed in the observatory, we chose to have all the appliances connected by an Ethernet layer and all the systems inside the observatory virtualized. This has shown to minimize the necessity of visits to the telescope building for hardware fixes.

- Telescope and all the auxiliary peripherals are controlled by the `chimera` Observatory Control System. For that, the software was upgraded, with a dozen of new plugins was added. The `chimera` plugins control from the low-level instrument communication, e.g. controlling the camera and filter wheel, up to high-level tasks as

doing the automatic optical alignment by fitting Zernike coefficients to the images of defocused stars. All the plugins are Open Source publicly available at `chimera` GitHub repositories.

- Starting in 2017, the observatory operates autonomously every night, collecting data for the S-PLUS survey. Environmental data is gathered by a set of redundant weather stations and the OCS automatically takes decisions on whether the telescope should be open or not, and which observational program should be run in each night.

For the new method for obtaining stellar physical properties out of the photometric redshift PDF in §3 and its application to the estimation of the ALHAMBRA survey mass function in §4 we can summarize the results obtained in the following points:

- In Chap. 3 we derive a new method to estimate physical properties of galaxies from their template-redshift probability distribution function $p(z, T|D)$. This method uses information that is already computed when the photometric redshifts are estimated.

- We designed an application to the method introduced using the widely-used Composite Stellar Populations models technique together with a Markov Chain Monte Carlo method to construct the probability distribution functions for the stellar properties of the BPZ templates and, indirectly, of galaxies. The reliability of this implementation itself is tested in Appendix A. We find that, for the standard magnitude error of the ALHAMBRA survey, $\sigma \sim 0.05$, the expected precision in mean age and extinction is of $0.2 - 0.3$ dex while for the mass to light ratio is of 0.13 dex.

- We found that the existing BPZ templates add a color term in the zero point corrections for $z < 0.5$. This is because the calibration of BPZ templates was done for HST Deep Field observations with average redshift distributions greater than 0.5. This affect our mass estimation making them about 0.25 dex lower compared to the masses obtained by Taylor et al. (2011). The lack of red templates, typical of lower redshifts, is balanced by the over-use of bluer templates which are artificially reddened by introducing zero point factors.

- In Appendix A we show that, for simulated galaxies, the recovered mass to light ratios proved to be very stable up to noises of 0.1 mag, where the typical noises of the ALHAMBRA gold catalog are of 0.05 mag. This fact supports our expectations that the stellar masses will more reasonable after the BPZ templates are fixed.

- With the stellar masses estimated by the method and its implementation described in Chapter 3, we derive a stellar mass function for the ALHAMBRA gold catalog in Chapter 4.

- Again, the stellar mass functions estimated with the method are lower than expected, being galaxies found to be bluer than what is expected in the literature. This effect is shown in Figs. 4.4 and 4.7. The differences are too large to be explained only by statistical errors, so the effect of the template misrepresentation seen in Chap. 3 becomes more evident.

5.2 Future Work

For the robotic telescope and the S-PLUS survey, we still have four years of observations. Although the telescope is fully robotized, there is still room for improvement of the software that automatically switches between different surveys. Nowadays it only takes into account the moon phase and altitude to chose between the Main Survey or the others, so the most important task now is to fix parameters that define if a night is photometric or not. As commented in Chap. 2, there are three available options to take those decisions which can be used in parallel to obtain the most accurate (and redundant) information. The methods are:

- Make a quick reduction in the data that is being taken by the telescope and check its quality online. This quality control process is done by a `chimera` which waits for readout camera events, estimating quality parameters of the images right after they are produced.
- Use data from the all-sky cameras in the mountain, like TASCA. This method has the disadvantage of, when there is too much Moon brightness, false positives can be triggered.
- Use data from aTmCam, a small transparency monitor located near the 4m Blanco telescope. For that happen, the quality of the output data of the transparency monitor should be assessed, and an agreement to provide online data should be formed.

For the stellar masses and the stellar mass function, as shown in Chapters 3 and 4, the method developed in this thesis proved to have a great potential to robust generate stellar masses, and stellar mass function estimates. Nevertheless, for the stellar masses estimates are too low at redshifts lower than 0.5. As discussed in Chapter 4, this is caused due to a lack of red templates in the BPZ code library. For the fixing of these issues, we propose the following:

- Do an extensive study of template combinations to minimize the false color effect found in the zero points calculated by BPZ. The new set of templates must be simultaneously precise on the redshift estimation and physical properties. This requires a big step back into the Bayesian photometric redshift basics, and an extensive simulation will be necessary.

- With the lack of red templates issue solved, a new catalog of photometric redshifts and their PDFs will be estimated
- The stellar mass function for the ALHAMBRA survey will be then re-estimated with a more reliable set of PDFs, and they should agree better with other stellar mass functions of the literature, expanding the MF to redshifts bigger than 0.7 as done here.
- Confirmed the reliability of the method it can be applied to essentially any survey where BPZ can be run. Examples include SDSS, DES, J-PAS and others.

Appendix A

Validation of the $p(\vec{\theta}|z_i, T_j)$ *fit*

In this appendix, we explore the implementation of the method to estimate galaxy properties out of photometry, proposed in §3.4. Using mock galaxies, generated from the models themselves and perturbed with Gaussian noise, we explore how accurate the physical properties can be recovered. We also compare our method to the linear relationship of the stellar mass-to-light ratio with the $(g-i)$ *color, derived by Taylor et al. (2011).*

A.1 Simulations

Monte Carlo simulations are a traditional and efficient way to evaluate the efficiency of a method. In our case, the method is that presented in chapter 3, where we explain how to estimate physical properties of galaxies (mass-to-light ratios, mean ages, etc.) from photometric data alone. The simulations described below are designed to map how accurately these properties can be derived in the presence of errors. The effects of redshift, which shifts the photometric bands across the spectra as z-varies, are also studied.

To make these simulations, we created a mock catalog with 500 fake galaxies, generated by randomly sampling the parameters of the single exponential burst described in table 3.1. From the spectra generated from these parameters, we compute synthetic magnitudes for the 20 optical filters of the ALHAMBRA survey following the same procedure done for the BPZ templates in 3.4.1. Gaussian noise was added to the magnitudes of each object to simulate photometric uncertainties. We perform experiments for four levels of noise: $\sigma_n = 0$, 0.05, 0.1 and 0.5 mag, where σ_n is the standard deviation of the noise distribution.

$\sigma_n = 0$ runs, which correspond to no errors at all, are useful to map intrinsic degeneracies of stellar populations, such as that between age and extinction. These runs, therefore, establish the limiting precision which can be reached in the estimation of a property θ given perfect data (and the model assumptions, of course). In the other extreme, runs with $\sigma_n = 0.5$ mag represent the limit of very bad photometric data. The actual data used in thesis (the ALHAMBRA data) has a typical photometric uncertainty of $\sigma_n = 0.05$ mag, so this is the case most relevant

to this particular study. Simulations with $\sigma_n = 0.1$ mag correspond to a survey worse than ALHAMBRA but not as bad as $\sigma_n = 0.5$ mag.

The mock galaxy parameters that are randomized are the burst date, t_0, the e-folding timescale of the SFR(t) function, τ (actually, we randomize $\beta = \tau/t_0$), the extinction, A_V, and the metallicity, Z. As explained in § 3.4.4, however, t_0 and τ are not very meaningful nor interesting by themselves. A better way to evaluate the simulations is to compare more interesting and robust properties such as the mass-to-light ratio and mean stellar ages. In other words, though we generate mock galaxies from randomized values of t_0 and τ, we prefer to describe them in terms of an alternative and more physically meaningful pair of parameters: the mass-to-light ratio (Υ) and the luminosity weighted mean stellar age ($\langle \log t \rangle_L$). Specifically, we do the comparisons regarding the I-band mass-to-Light ratio, Υ_I, the mean age weighted by the V-band flux, $\langle \log t \rangle_L$, the extinction in the V-band, A_V, and the stellar metallicity $Z_\star$. The methodology to estimate these properties from photometric data is explained in detail in § 3.4.4.

The noise-added synthetic magnitudes are fed into the fitting algorithm, and the output properties are compared with the known input properties by means of their differences, i.e. $\Delta p = p_{out} - p_{in}$, and their standard deviations.

In Fig. A.1 we show the results of the simulations. Each panel compares input (x-axis) and output (y-axis) values of the mean age, extinction, and stellar mass-to-light ratio, from left to right, respectively. From top to bottom we increase the level of noise from $\sigma_n = 0$ to 0.05, 0.1 and 0.5 mag. The mock galaxy spectra in these simulations were generated from a redshift $z = 0$, since we want first to evaluate the effects of noise upon the derived properties. The Calzetti et al. (1994) reddening law was used in all simulations described here.

The plots show that, as the noise σ_n increases, the age and extinction estimates become increasingly dispersed around the output = input line, as intuitively expected. Even for $\sigma_n = 0$ (i.e., no noise) there is some dispersion, but it is small: 0.10 dex in $\langle \log t \rangle_L$, and 0.12 mag in A_V (see Table A.1). The dispersion increases to 0.23 dex in $\langle \log t \rangle_L$, and 0.27 mag in A_V for ALHAMBRA-like photometric errors $\sigma_n = 0.05$ mag, reaching 0.54 dex in $\langle \log t \rangle_L$, and 0.49 mag in A_V in the limit of very bad data, $\sigma_n = 0.5$ mag. Ages and extinctions estimates are therefore very sensitive to photometric errors. Stellar metallicities (not plotted in Fig. A.1, but listed in Table A.1) are even worse.

In contrast, the estimate of the stellar mass-to-light ratio does not degrade as fast. The right panels of Fig. A.1 show that Υ_i remains quite stable, being recoverable within a satisfactory margin of error up to $\sigma_n = 0.1$ dex. This implies that stellar masses can be estimated with relatively good precision even when ages and extinctions cannot.

This intriguing behavior is a result of the degeneracy between age and extinction. As shown in Fig. A.2, when the method overestimates

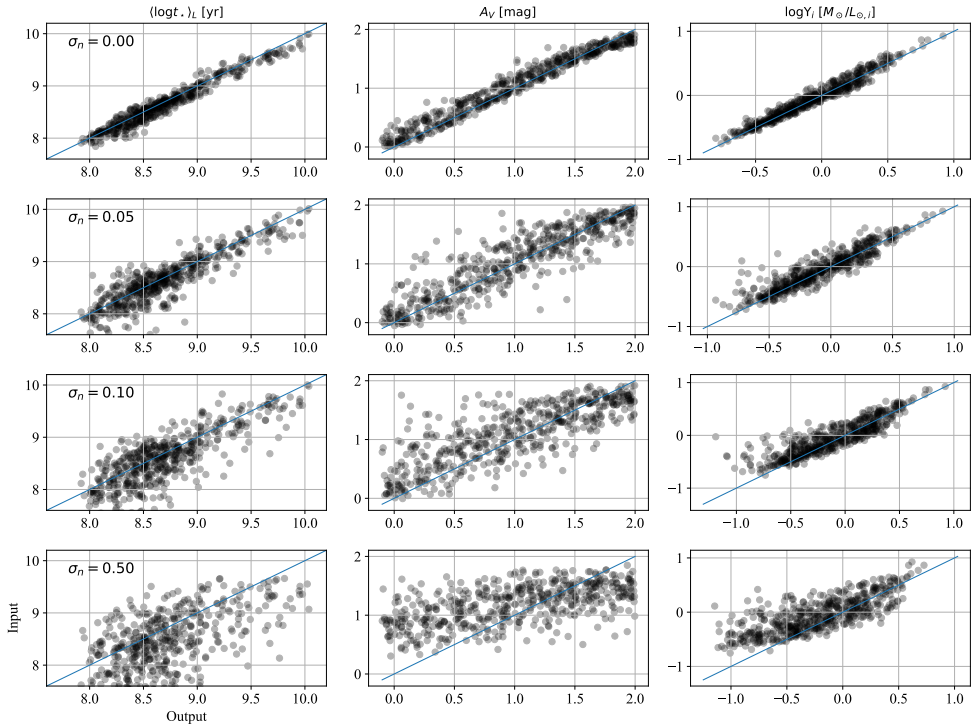

FIGURE A.1 Input parameters in x axis versus the average parameters from the output PDF in y to, from left, the age, extinction and stellar mass-to-light ratio. From top added noises in the input synthetic magnitudes of $\sigma_n = 0, 0.05, 0.1$ and 0.5 mag.

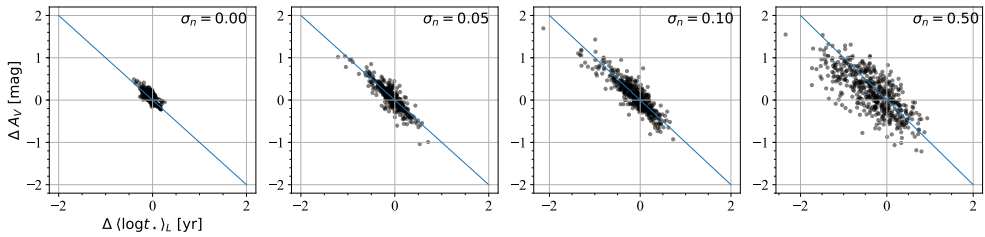

FIGURE A.2 Output minus input difference in $\langle \log t \rangle_L$ plotted against the corresponding differences in A_V. Each panel shows results for simulations with different levels of photometric noise ($\sigma_n = 0$, 0.05, 0.1, and 0.5 mag), as indicated in the labels.

noise	$\Delta \log \Upsilon_i$	$\Delta\langle \log t\rangle_L$	ΔA_V [mag]	$\Delta \log Z$
0 [1]	0.00 ± 0.07	-0.04 ± 0.10	0.05 ± 0.12	0.03 ± 0.19
0.05	-0.02 ± 0.13	-0.06 ± 0.23	0.05 ± 0.27	0.00 ± 0.28
0.1	-0.03 ± 0.17	-0.12 ± 0.35	0.10 ± 0.36	0.02 ± 0.35
0.5	-0.08 ± 0.24	-0.33 ± 0.54	0.18 ± 0.49	-0.02 ± 0.40

TABLE A.1 Summary of input versus output simulations. For the different noises, we have the average output minus input values $\pm$ the standard deviation for the mock catalog of 500 random parameter sets. Calzetti et al. (1994) extinction law was used and $z = 0$.

$\langle \log t\rangle_L$ it tends to underestimate A_V. This well-known degeneracy of stellar populations is present even for perfect data ($\sigma_n = 0$), and it only gets worse as σ_n increases. The physical explanation is simple and well known. Both age and A_V redden a galaxy spectrum as they increase in value. Hence, if one is overestimated, the other must be underestimated (and vice-versa) to compensate.

The mass-to-light ratio, on the other hand, increases with both age and A_V. As a stellar population gets older, it produces less light per unit mass (hence larger Υ). Similarly, the more extinct it is, the less stellar light will come out per unit mass (hence larger Υ too). Therefore, overestimating the age while simultaneously underestimating the extinction (or vice-versa) have opposite and approximately canceling effects upon Υ (e.g., Taylor et al. 2011). In other words, the same age-extinction degeneracy which has a negative influence on the estimation of $\langle \log t\rangle_L$ and A_V, conspire to make Υ a much more robust property than either $\langle \log t\rangle_L$ and A_V.

Table A.1 summarizes the results of the simulations. The values in this table confirm that Υ is much less sensitive to errors than any of the other stellar properties. This explains why most of this study focused on results related to stellar masses, and relatively little attention was devoted to stellar ages, extinction, and metallicity.

All the discussion so far focused on the effects of noise (σ_n) upon the estimation of stellar properties, and all simulations described above were performed assuming $z = 0$. As z increases, the ALHAMBRA filters sample different parts of the (mock) galaxy spectra, which in turn leads to distinct sensitivities to properties like mean age, extinction, mass-to-light ratio, and metallicity.

To study the impact of the redshift in the recoverability of the parameters we repeat the same simulations above but for eight values of z between 0 and 1. In Fig. A.3 we summarize the results of these simulations. For each property (mass-to-light ratio, mean age, extinction and metallicity) we compute the statistics of the output minus input difference, $\Delta p = p_{out} - p_{in}$. This is done for each of the four levels of σ_n and the 8 z's. In each panel in Fig. A.3 the error bars show the average

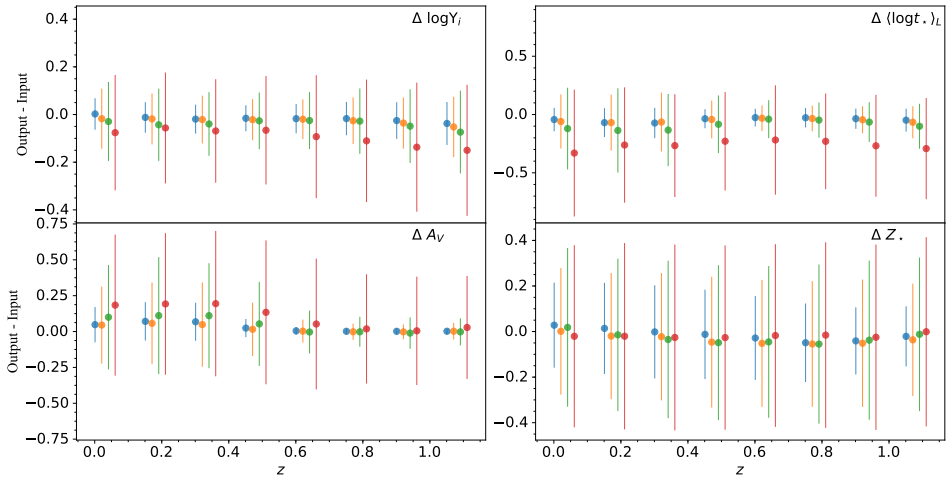

FIGURE A.3 Average difference between output and input simulated properties and its standard deviation (error bars). Each set of lines correspond to a different redshift ($z = 0, 0.15, 0.30, 0.45, 0.60, 0.75, 0.90$ and 1.05), with each color line representing a different Gaussian noise added of $\sigma = 0, 0.05, 0.1$ and 0.5 with a small offset in redshift for display purposes.

$\pm$ one standard deviation of Δp versus z for a given property. Different levels of noise are plotted with different colors, and the points have been slightly offset in z for better display (σ_n increases from left to right).

The average differences are primarily flat with redshift, indicating that our method does not introduce any significant trend to systematically under or overestimate stellar properties as z increases. The only minor exception is Υ_i (top right panel), which shows a slight downwards slope in the limit of large photometric errors ($\sigma_n = 0.5$ mag), but the bias is negligible given the error bars. Furthermore, we see that for a fixed σ_n, the size of the error bars in $\log \Upsilon_i$, $\langle \log t \rangle_L$, and $\log Z$ do not change with z. This implies that the precision of the estimates is the same at all redshifts. The exception to this rule is A_V (bottom right panel), whose error bars tend to decrease as z increases. This interesting behavior of A_V is explained by the shape of the extinction curve, which rises towards smaller λ's. As z increases the ALHAMBRA filters sample bluer regions of the galaxy spectrum, which are more sensitive to dust extinction. This leads to the systematic decrease in the uncertainty in A_V as z increases seen in the plot. The estimation of A_V thus becomes more precise as z increases.

A.2 Comparison with the literature

It is a common practice to adopt a linear relationship between the stellar mass-to-light ratio and (rest-frame) and galaxy colors. Examples of studies that have used such relationships include Kannappan and Gawiser (2007); Taylor et al. (2011); Wilkins et al. (2013). In this section, we compare our mass-to-light ratios with that derived using the $g-i$ color, as proposed by Taylor et al. (2011). In its current implementation the BPZ code already estimates galaxy masses using the $\Upsilon = \Upsilon(g-i)$ relation of Taylor et al. (2011), so we want to check if our Υ values agree with it.

Taylor et al. (2011) define a relation between the (rest-frame) *i*-band stellar mass-to-light ratio and the (rest-frame) $g-i$ color as

$$\log \Upsilon_i = -0.68 + 0.70(g-i) \tag{A.1}$$

where Υ_i is in solar units.

Combining this equation with the *i*-band absolute magnitude M_i of a galaxy gives us the stellar mass:

$$\log M_\star = 1.15 + 0.70(g-i) - 0.4M_i \tag{A.2}$$

where $M_\star$ is given in solar masses, and $M_{i,\odot} = 4.58$ was assumed.

This relation was derived for the objects in the GAMA catalog which is based on a set of galaxies with spectroscopic redshifts complete in the range of $0 < z < 0.65$. The (spectroscopic) redshifts and the galaxy magnitudes in the SDSS filters are compared to a pre-computed grid of τ-models based on the Bruzual and Charlot (2003) stellar population models and with reddening given by the Calzetti et al. (1994) law. In total, a grid of $34 t_0's \times 19\tau's \times 43 A_V's \times 6 Z_\star's = 166.688$ models was generated for each of the 66 redshifts producing a total of ~ 11 million models.

In Fig. A.4, extracted from Taylor et al. (2011), we show how the relation between mass-to-light ratio and $(g-i)$ color was derived: A set of galaxies from the GAMA catalog had their stellar mass-to-light ratios estimated using their grid of τ-models, then the galaxies were plotted in the plane $(g-i)$ versus $\log \Upsilon_i$ and a linear fit is performed. The fitted relation (equation A.1) is shown as the red line in Fig. A.4. The average relation from their full library of models is shown by the solid black line.

In Fig. A.5 we show the comparison between the (PDF-averaged) masses obtained by our method with the masses derived from the $(g-i)$ color. In the left panel, we show in the x axis the stellar mass obtained with eq. A.2 and in the y axis the stellar mass estimated with the method described in this thesis. In the right panel, we show the difference between the two. In both panels, it is evident that there is a bimodality in the differences of the masses. The differences are negligible for

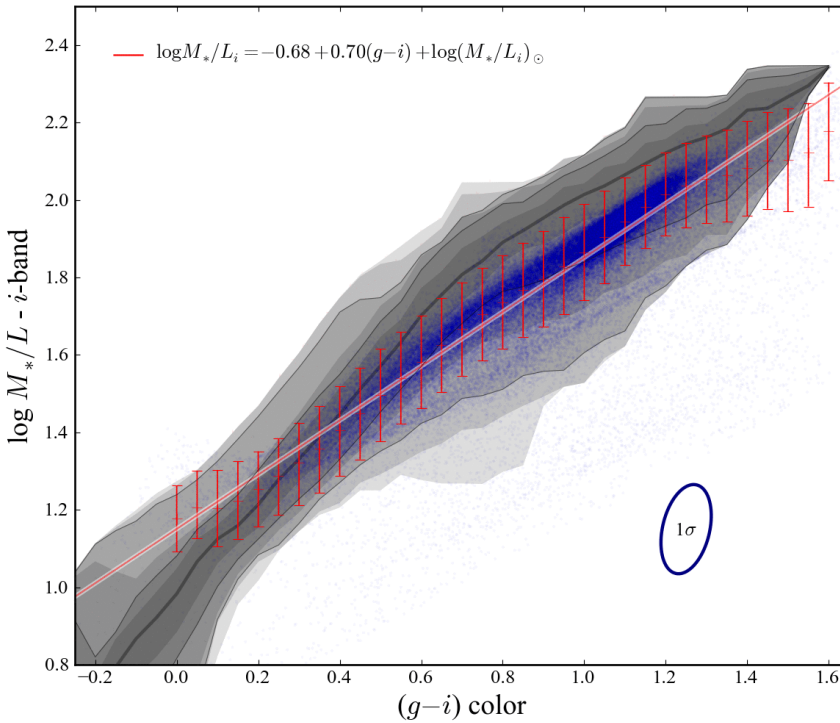

FIGURE A.4 Relation between restframe $g-i$ color and $\log M_\star/L_i$ extracted from Taylor et al. (2011). Blue dots are the galaxies for the GAMA catalog. The red dots are the median of the mass-to-light in narrow bins of $g-i$, and the error bars account for $\pm 1\sigma$ of the objects in the bin. The solid red line shows the linear fit for the $g-i$ versus mass-to-light relation, given by Eq. A.1. The black central line corresponds to the prior-weighted median for the models in their stellar population library with the contours are equivalent to the $\pm 0.5, 1.0, \ldots, 3.0\sigma$ of the distribution.

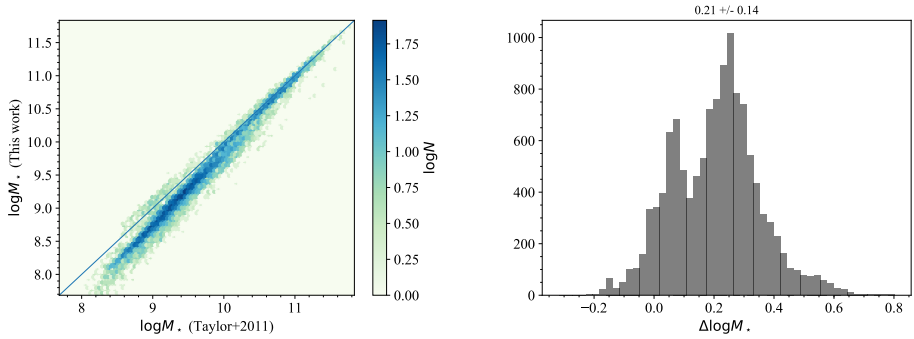

FIGURE A.5 Left: Stellar masses obtained by our method versus stellar masses obtained using the relation provided by Taylor et al. (2011) Each point is marked by the log. number of the objects in that bin. Right: Histogram of the difference between the stellar mass estimated by our method and the mass determined by Taylor et al. (2011) method, i.e., $\Delta \log M_\star = \log M_\star$ (Taylor+2011) $- \log M_\star$ (This work).

$M_\star \gtrsim 10^{10} M_\odot$, but for less massive galaxies our method tends to produce $M_\star$-values systematically lower that those obtained with eq. A.2.

In Fig. A.6 we investigate further this bimodality by plotting Υ_i versus rest-frame $(g-i)$ color for each template using eq. A.1 (black dots) and the mass-to-light calculated by our methodology (points colored by template type, with error bars as the standard deviation of the PDF). We see that for most of the BPZ templates, there is an excellent agreement between our stellar mass-to-light ratios and the ones from A.1. However, for the SB templates, our mass-to-light ratios can be up to 0.7 dex lower than theirs. This mismatch is at the root of the differences in mass reported above.

We can see in Fig. A.4 that there are very few objects below $(g-i) = 0.2$ in the GAMA data used by Taylor et al. (2011) to calibrate eq. A.1. Judging by the average curve for their grid of models (the black line), one sees that eq. A.1 tend to overestimate Υ_i when $(g-i) < 0.2$. Because of cosmic downsizing (Lilly et al., 1996), low mass galaxies tend to have younger stars and thus bluer colors, so they are the ones most affected by this incorrect extrapolation of eq. A.1, in agreement with what we saw in the left panel of Fig. A.5.

Another reason for the difference in stellar mass estimates is related to frequent use, by BPZ, of the bluest templates. $(g-i)$ rest-frame color of 0.2 or less occur for the eight bluest template interpolations from the BPZ library. These templates are the best-fit ones for 25% of the objects in the ALHAMBRA gold catalog, but are almost absent from Taylor's sample (Fig. A.4). As seen in Fig. A.6, these are also the ones for which

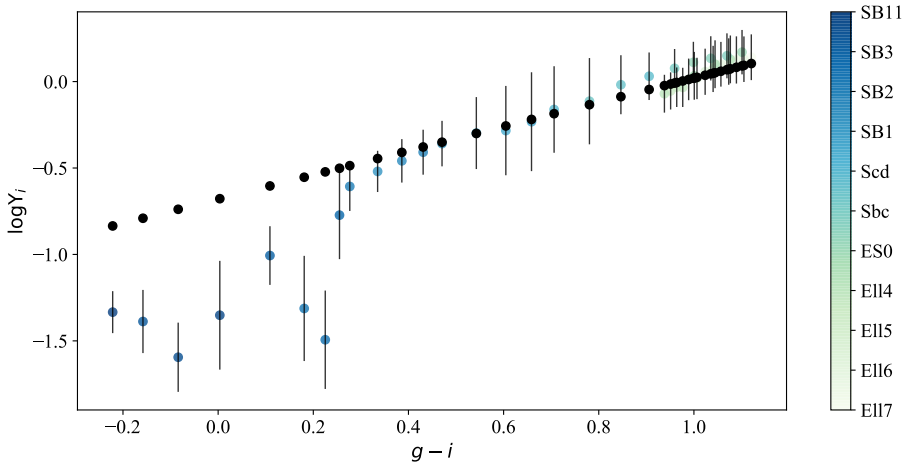

FIGURE A.6 Comparison between our $\log \Upsilon_i$ and the obtained from eq. A.1 in black. The colored points represent the average $\log \Upsilon_i$ from the method of this thesis, with error bars showing the dispersion on the distributions and colors indicating the BPZ template.

our estimates of Υ_i differs the most from the Taylor relation.

As discussed in §4.6, this high frequency with which these templates are used by BPZ is a side-effect of the lack of red templates in its library, combined with an artificial compensation as a color term in the zero-point calibrations. Also, as commented in §4.6, the solution for this problem lies on a revision of the BPZ library templates to better represent the galaxy populations in $0 < z < 0.5$.

Appendix B

T80S building plant

In this Appendix, we show the plans for the T80S telescope buildings. These plans are essential to the understanding of how the installations were organized and serve as a source of information for projecting future upgrades.

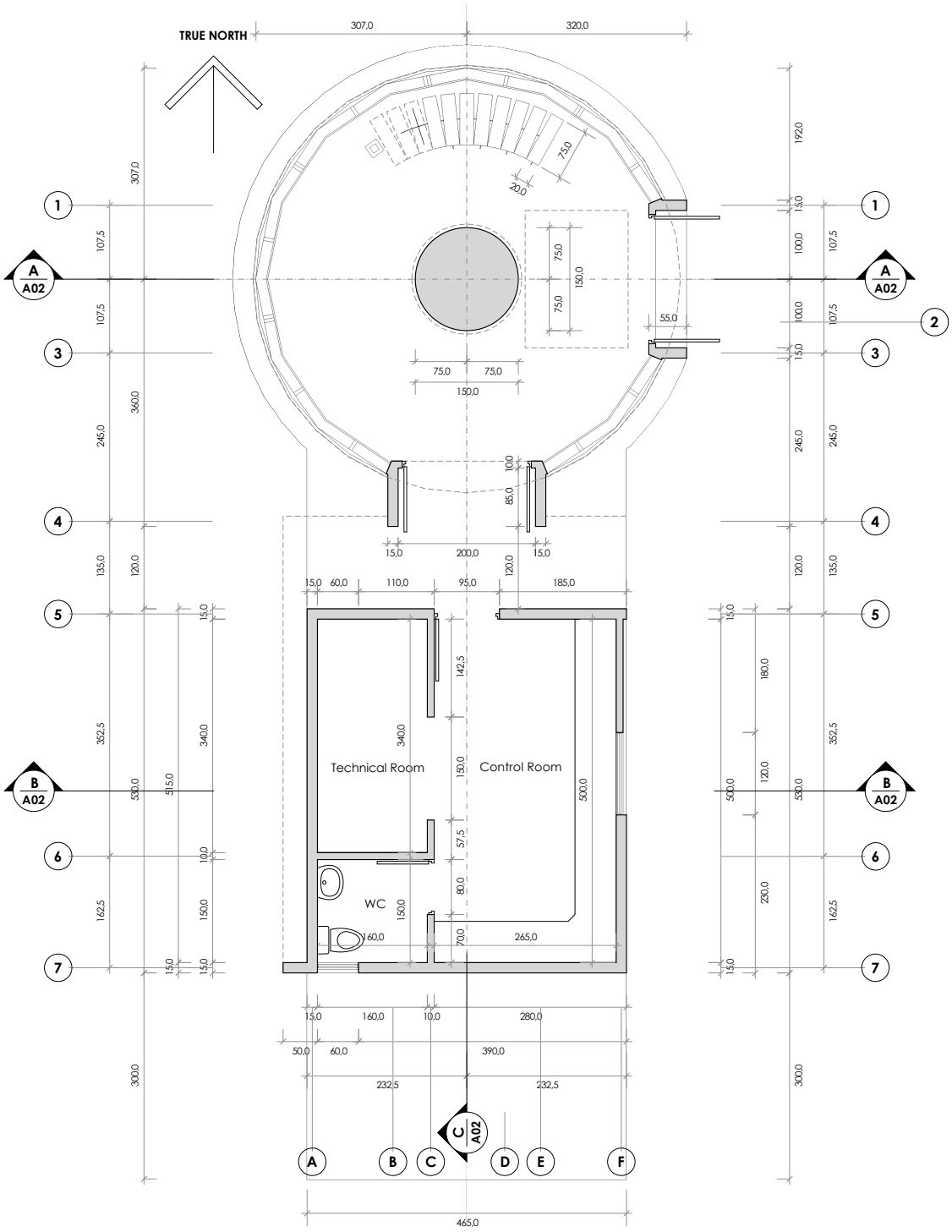

01

Planta Primer Piso

escala 1:50

03 Corte A-A
escala 1:50

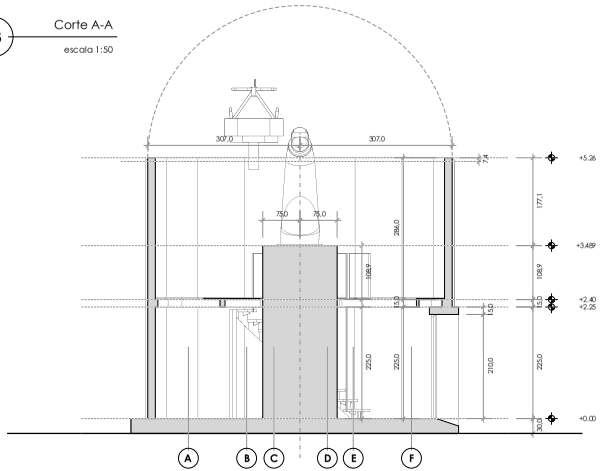

04 Corte B-B
escala 1:50

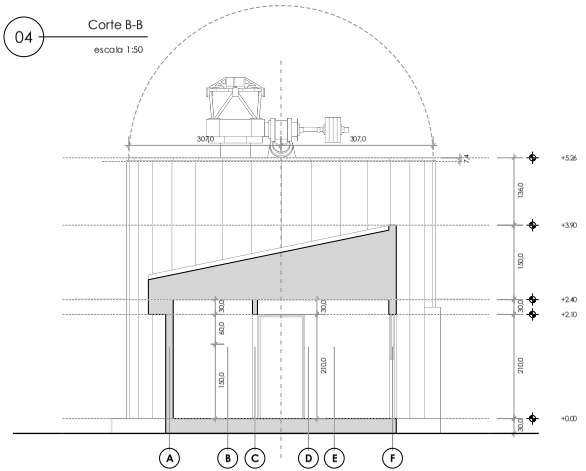

05 Corte C-C
escala 1:50

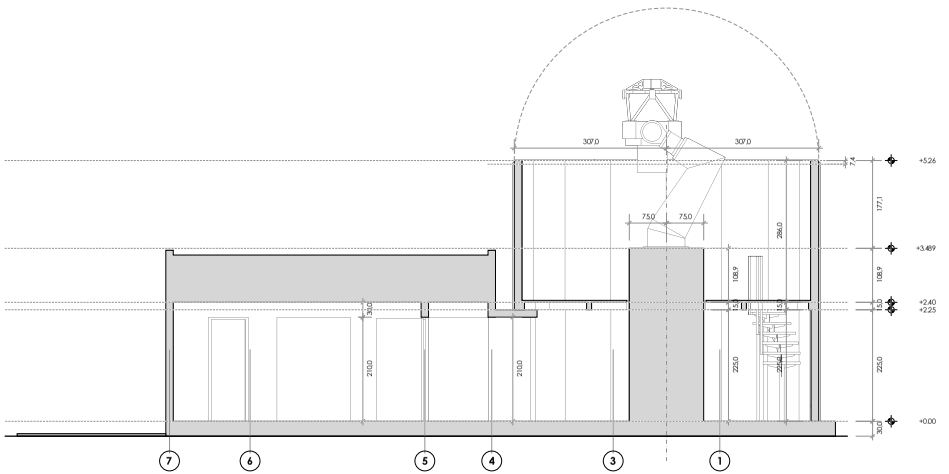

revisiones

1	2022.03	
2	2022.03	
3		
4		

Proyecto de Arquitectura T-80 Telescope AURA Inc.

Association of Universities for Research in Astronomy, Aura Inc.

Rodrigo Pino Materno
arquitecto C-4990

Association of Universities for Research in Astronomy, Aura Inc.

contenido
01 corte A-A
02 corte B-B
03 corte C-C

escala 1:50
formato A1 (420 x 594)

lámina
A02

06 Elevación Este

escala 1:50

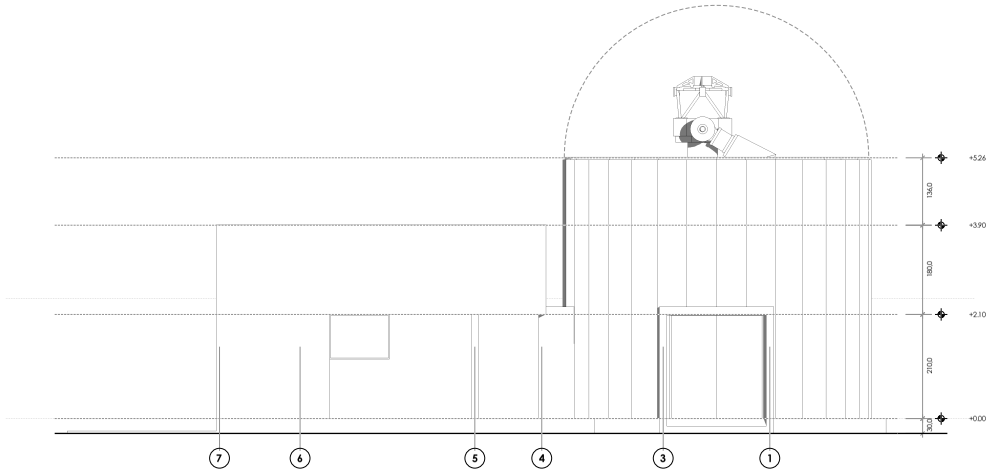

07 Elevación Oeste

escala 1:50

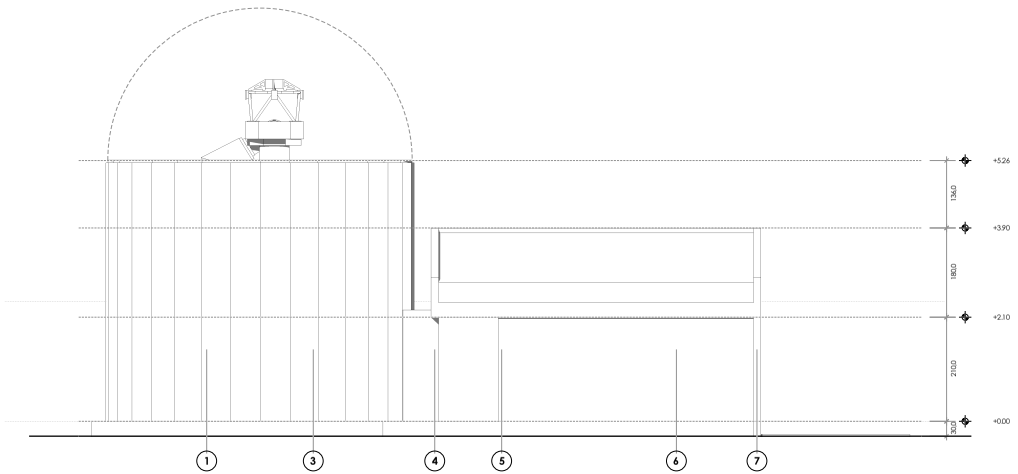

revisiones		
1	2020.11.13	
2	2020.12.13	
3		
4		

Proyecto de Arquitectura T-80 Telescopio AURA Inc.

Association of Universities for Research in Astronomy, Aura Inc.

Rodrigo Pino Moreno
arquitecto - curitiba

Association of Universities for Research in Astronomy, Aura Inc.

contenido

elevaciones

escala 1:50
formato A1 (420 x 594)

lámina

A03

08 Elevación Sur

escala 1:50

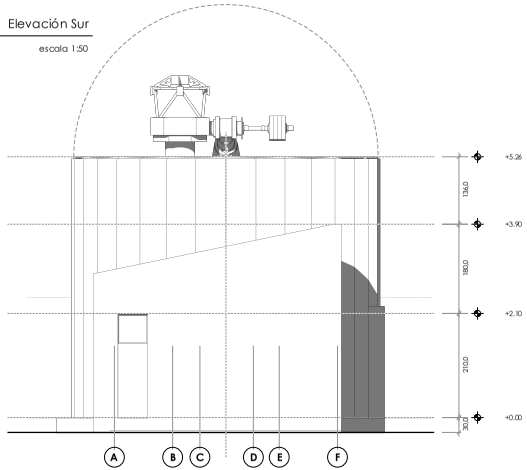

09 Elevación Norte

escala 1:50

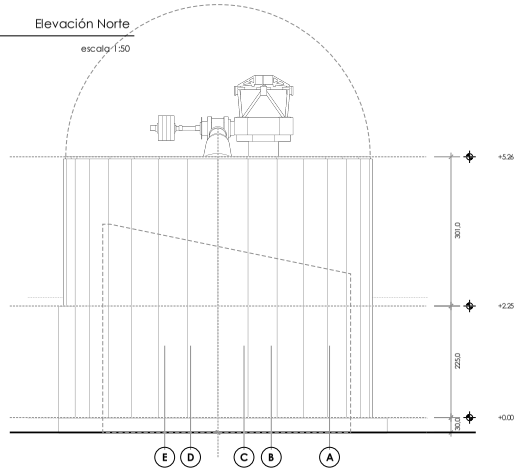

10 Perspectiva

s/escala

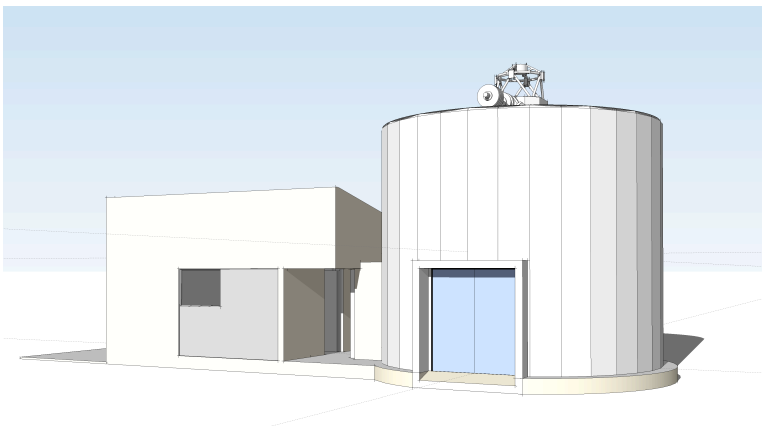

revisiones		
N°	fecha	
1	2022.12.13	
2	2022.12.13	
3		
4		
5		

Proyecto de Arquitectura
T-80 Telescope AURA Inc.

Association of Universities for Research in Astronomy, Aura Inc.

Rodrigo Pino Moreno
arquitecto - curtidor

Association of Universities for Research in Astronomy, Aura Inc.

contenido
A04 - Alzados
A05 - Secciones
3D - perspectivas
formato A1 (420 x 594)

lámina
A04

Appendix C

T80SCam readout gains and noises

In this Appendix, we show a Table with the gains and readout noises measured in Spectral Instruments Laboratory. This information is crucial to scale the counts values of each T80SCam amplifier correctly and to calculate the count errors obtained in each amplifier.

T80SCam gain and read out noises. Each row represents a readout mode while each column represents a different amplifier of the CCD.

Amplifier	Readout	0		1		2		3		4		5		6		7	
Mode	rate	Gain	RON	Gain	RON	Gain	RON	Gain	RON	Gain	RON	Gain	RON	Gain	RON	Gain	RON
0	1.01MHz	2.06	6.58	2.06	6.58	2.02	6.58	2.02	6.57	2.01	6.58	2.00	6.79	1.97	6.43	2.00	6.64
1	1.01MHz	0.92	5.26	0.92	5.25	0.92	5.25	0.90	5.25	0.90	5.25	0.90	5.51	0.88	5.18	0.90	5.24
2	1.01MHz	1.97	6.25	1.94	6.26	1.93	6.26	1.90	6.27	1.91	6.25	1.92	6.48	1.87	6.11	1.91	6.31
3	1.01MHz	0.90	5.13	0.90	5.13	0.89	5.13	0.88	5.14	0.88	5.13	0.88	5.40	0.86	5.08	0.87	5.11
4	500kHz	2.15	4.43	2.14	4.39	2.12	4.47	2.11	4.39	2.12	4.46	2.10	4.78	2.06	4.30	2.09	4.42
5	500kHz	0.96	3.40	0.96	3.39	0.96	3.40	0.94	3.37	0.94	3.40	0.94	3.86	0.92	3.36	0.93	3.38
6	500kHz	2.05	4.20	2.02	4.18	2.00	4.25	2.00	4.26	2.00	4.22	1.99	4.54	1.96	4.10	2.00	4.22
7	500kHz	0.94	3.31	0.94	3.33	0.94	3.31	0.92	3.31	0.92	3.31	0.92	3.75	0.90	3.28	0.91	3.29
8	250kHz	2.18	3.47	2.16	3.46	2.14	3.48	2.13	3.48	2.13	3.47	2.12	3.93	2.09	3.43	2.11	3.43
9	250kHz	0.97	2.72	0.97	2.71	0.97	2.71	0.95	2.71	0.95	2.72	0.96	3.22	0.93	2.70	0.94	2.71
10	250kHz	2.07	3.31	2.05	3.30	2.04	3.30	2.02	3.30	2.01	3.31	2.02	3.74	1.98	3.25	2.02	3.32
11	250kHz	0.94	2.66	0.94	2.65	0.94	2.66	0.93	2.66	0.93	2.66	0.93	3.15	0.91	2.65	0.92	2.66
12	100kHz	2.18	2.78	2.17	2.78	2.15	2.78	2.13	2.78	2.15	2.78	2.13	3.09	2.09	2.74	2.13	2.80
13	100kHz	0.96	2.33	0.96	2.33	0.96	2.33	0.95	2.33	0.95	2.33	0.95	2.69	0.92	2.29	0.94	2.34
14	100kHz	2.08	2.66	2.06	2.67	2.04	2.66	2.03	2.67	2.04	2.66	2.02	2.96	1.99	2.63	2.03	2.67
15	100kHz	0.95	2.30	0.95	2.31	0.95	2.30	0.93	2.31	0.93	2.31	0.93	2.66	0.91	2.28	0.92	2.32

Amplifier	Readout	8		9		10		11		12		13		14		15	
Mode	rate	Gain	RON	Gain	RON	Gain	RON	Gain	RON	Gain	RON	Gain	RON	Gain	RON	Gain	RON
0	1.01MHz	2.09	6.62	2.06	6.58	2.03	6.51	2.04	6.59	2.04	6.60	2.04	6.73	2.04	6.56	2.02	6.63
1	1.01MHz	0.93	5.23	0.92	5.24	0.91	5.23	0.92	5.29	0.92	5.32	0.92	5.34	0.92	5.28	0.90	5.25
2	1.01MHz	1.99	6.27	1.95	6.25	1.93	6.18	1.95	6.29	1.95	6.30	1.95	6.39	1.96	6.31	1.90	6.23
3	1.01MHz	0.91	5.14	0.90	5.07	0.89	5.15	0.90	5.17	0.90	5.19	0.90	5.20	0.91	5.15	0.89	5.13
4	500kHz	2.18	4.57	2.15	4.48	2.12	4.40	2.13	4.42	2.12	4.56	2.14	4.61	2.12	4.44	2.10	4.45
5	500kHz	0.97	3.39	0.96	3.35	0.95	3.37	0.96	3.44	0.96	3.48	0.96	3.43	0.96	3.39	0.95	3.40
6	500kHz	2.07	4.33	2.05	4.25	2.02	4.15	2.02	4.19	2.03	4.34	2.04	4.36	2.04	4.24	2.00	4.19
7	500kHz	0.95	3.29	0.95	3.28	0.93	3.27	0.94	3.36	0.94	3.40	0.94	3.37	0.94	3.31	0.93	3.34
8	250kHz	2.20	3.48	2.17	3.40	2.14	3.42	2.16	3.52	2.15	3.50	2.16	3.50	2.15	3.44	2.13	3.49
9	250kHz	0.99	2.65	0.98	2.64	0.96	2.71	0.97	2.77	0.97	2.79	0.97	2.73	0.97	2.68	0.95	2.70
10	250kHz	2.10	3.33	2.07	3.25	2.04	3.28	2.05	3.37	2.04	3.34	2.05	3.33	2.04	3.27	2.03	3.32
11	250kHz	0.96	2.61	0.95	2.58	0.93	2.63	0.94	2.71	0.95	2.73	0.95	2.68	0.95	2.63	0.94	2.67
12	100kHz	2.20	2.69	2.17	2.68	2.15	2.73	2.17	2.82	2.16	2.87	2.18	2.81	2.16	2.76	2.13	2.76
13	100kHz	0.98	2.20	0.97	2.24	0.95	2.29	0.96	2.38	0.96	2.41	0.97	2.35	0.97	2.31	0.95	2.32
14	100kHz	2.10	2.58	2.07	2.57	2.05	2.62	2.07	2.69	2.04	2.74	2.07	2.70	2.07	2.65	2.03	2.65
15	100kHz	0.97	2.18	0.95	2.20	0.94	2.28	0.96	2.37	0.96	2.41	0.95	2.33	0.95	2.27	0.94	2.31

Appendix D

Chimera usage example

In this Appendix, we show a practical example of usage of `chimera`*. We show how to connect to a setup of a Telescope and a Camera and take a test exposure from inside a Python script. The steps involved in this process are described along with the script.*

Import chimera modules

```
In [52]: from chimera.core.manager import Manager
         from chimera.util.position import Position, Epoch
```

Import miscellaneous modules: astropy, numpy and matplotlib

```
In [53]: import numpy as np
         from astropy.io import fits
         from matplotlib import cm
         import matplotlib.pyplot as plt
         %matplotlib inline
```

Set up a chimera manager

```
In [54]: manager = Manager()
```

Get a proxy for the Telescope and Camera

```
In [55]: telescope = manager.getProxy("127.0.0.1:7666/FakeTelescope/fake")
         camera = manager.getProxy("127.0.0.1:7666/FakeCamera/fake")
```

Slew telescope to NGC 4755 (Jewel Box)

```
In [56]: telescope.slewToRaDec(Position.fromRaDec(Coord.fromHMS("12:53:39"),
                                                  Coord.fromDMS("-60:21:00"),
                                                  epoch=Epoch.J2000))
```

Expose camera for 1 second (FakeCamera returns a DSS archive image)

```
In [57]: image = camera.expose(exptime=1)
```

Images have a `http()` method to be easily accessed over network

```
In [58]: print image[0].http()
```

```
http://127.0.0.1:7669/image/96a2836c1278b22c66a0862b916dbf2c27e
```

So we can easily load the raw image into a variable

```
In [59]: img = fits.getdata(image[0].http())
```

```
Downloading http://127.0.0.1:7669/image/96a2836c1278b22c66a0862b916dbf2c27e [Done]
```

and plot it

```
In [60]: plt.imshow(np.log10(img), cmap=cm.hot)
```

```
Out[60]: <matplotlib.image.AxesImage at 0x1168956d0>
```

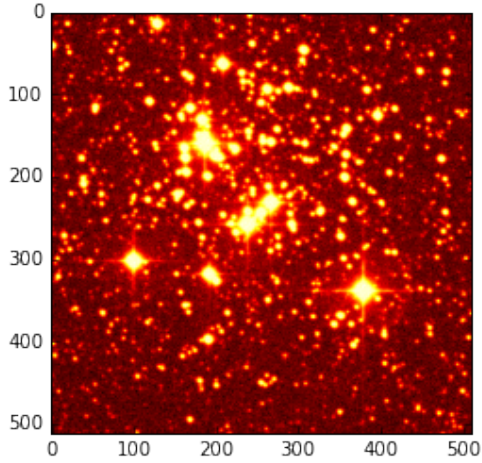
0
100
200
300
400
500
0
100
200
300
400
500

Appendix E

List of Publications

The following list of scientific publications represents the different contributions done during the period of this thesis. The refereed publications are those published in refereed journals while the Non-refereed publications are mainly articles published on meeting proceedings and on pre-print archives.

E.1 Refereed publications

1. CLASH: Accurate Photometric Redshifts with 14 HST bands in Massive Galaxy Cluster Cores (Molino et al., 2017, accepted)
2. Star formation and AGN activity in the most luminous LINERs in the local universe (Pović et al., 2016)
3. An accurate cluster selection function for the J-PAS narrow-band wide-field survey (Ascaso et al., 2016)
4. Galaxy clusters and groups in the ALHAMBRA survey (Ascaso et al., 2015)
5. Results of two multichord stellar occultations by dwarf planet (1) Ceres (Gomes-Júnior et al., 2015)
6. The ALHAMBRA Survey: Bayesian photometric redshifts with 23 bands for 3 deg (Molino et al., 2014)
7. The Size, Shape, Albedo, Density, and Atmospheric Limit of Transneptunian Object (50000) Quaoar from Multi-chord Stellar Occultations (Braga-Ribas et al., 2013)

E.2 Non-refereed publications

1. Star formation and AGN activity in the most luminous LINERs in the local universe (Márquez et al., 2017)
2. The Astropy Problem Muna et al. (2016)

3. Chasing FERMI, Swift, and INTEGRAL GRBs with the T80 telescope of Javalambre Observatory (Gorosabel et al., 2014)
4. MagAl: A new tool to analyse galaxies photometric data (Schoenell et al., 2014)
5. Software and cyber-infrastructure development to control the Observatorio Astrofísico de Javalambre (OAJ) (Yanes-Díaz et al., 2014)
6. Goals and strategies in the global control design of the OAJ Robotic Observatory (Rueda-Teruel et al., 2013)
7. Recovering physical properties from narrow-band photometry Schoenell et al. (2013)
8. Goals and strategies in the global control design of the OAJ Robotic Observatory (Yanes-Díaz et al., 2012)
9. Stellar Occultations by TNOs: the January 08, 2011 by (208996) 2003 AZ84 and the May 04, 2011 by (50000) Quaoar (Braga-Ribas et al., 2011)

Bibliography

Abrahamse, A., Knox, L., Schmidt, S., Thorman, P., Tyson, J. A., and Zhan, H.: 2011, *ApJ* **734**, 36

Asari, N. V., Cid Fernandes, R., Stasińska, G., Torres-Papaqui, J. P., Mateus, A., Sodré, L., Schoenell, W., and Gomes, J. M.: 2007, *MNRAS* **381**, 263

Ascaso, B., Benítez, N., Dupke, R., Cypriano, E., Lima-Neto, G., López-Sanjuan, C., Varela, J., Alcaniz, J. S., Broadhurst, T., Cenarro, A. J., Devi, N. C., Díaz-García, L. A., Fernandes, C. A. C., Hernández-Monteagudo, C., Mei, S., Mendes de Oliveira, C., Molino, A., Oteo, I., Schoenell, W., Sodré, L., Viironen, K., and Marín-Franch, A.: 2016, *MNRAS* **456**, 4291

Ascaso, B., Benítez, N., Fernández-Soto, A., Arnalte-Mur, P., López-Sanjuan, C., Molino, A., Schoenell, W., Jiménez-Teja, Y., Merson, A. I., Huertas-Company, M., Díaz-García, L. A., Martínez, V. J., Cenarro, A. J., Dupke, R., Márquez, I., Masegosa, J., Nieves-Seoane, L., Pović, M., Varela, J., Viironen, K., Aguerri, J. A. L., Olmo, A. D., Moles, M., Perea, J., Alfaro, E., Aparicio-Villegas, T., Broadhurst, T., Cabrera-Caño, J., Castander, F. J., Cepa, J., Cerviño, M., Delgado, R. M. G., Cristóbal-Hornillos, D., Hurtado-Gil, L., Husillos, C., Infante, L., Prada, F., and Quintana, J. M.: 2015, *MNRAS* **452**, 549

Baldry, I. K., Driver, S. P., Loveday, J., Taylor, E. N., Kelvin, L. S., Liske, J., Norberg, P., Robotham, A. S. G., Brough, S., Hopkins, A. M., Bamford, S. P., Peacock, J. A., Bland-Hawthorn, J., Conselice, C. J., Croom, S. M., Jones, D. H., Parkinson, H. R., Popescu, C. C., Prescott, M., Sharp, R. G., and Tuffs, R. J.: 2012, *MNRAS* **421**, 621

Baldry, I. K., Glazebrook, K., Brinkmann, J., Ivezić, Ž., Lupton, R. H., Nichol, R. C., and Szalay, A. S.: 2004, *ApJ* **600**, 681

Baldry, I. K., Glazebrook, K., and Driver, S. P.: 2008, *MNRAS* **388**, 945

Bell, E. F., McIntosh, D. H., Katz, N., and Weinberg, M. D.: 2003, *ApJS* **149**, 289

Bell, E. F., Wolf, C., Meisenheimer, K., Rix, H.-W., Borch, A., Dye, S., Kleinheinrich, M., Wisotzki, L., and McIntosh, D. H.: 2004, *ApJ* **608**, 752

Benítez, N.: 2000, *ApJ* **536**, 571

Benitez, N., Dupke, R., Moles, M., Sodre, L., Cenarro, J., Marin-Franch, A., Taylor, K., Cristobal, D., Fernandez-Soto, A., Mendes de Oliveira, C., Cepa-Nogue, J., Abramo, L. R., Alcaniz, J. S., Overzier, R., Hernandez-Monteagudo, C., Alfaro, E. J., Kanaan, A., Carvano, J. M., Reis, R. R. R., Martinez Gonzalez, E., Ascaso, B., Ballesteros, F., Xavier, H. S., Varela, J., Ederoclite, A., Vazquez Ramio, H., Broadhurst, T., Cypriano, E., Angulo, R., Diego, J. M., Zandivarez, A., Diaz, E., Melchior, P., Umetsu, K., Spinelli, P. F., Zitrin, A., Coe, D., Yepes, G., Vielva, P., Sahni, V., Marcos-Caballero, A., Shu Kitaura, F., Maroto, A. L., Masip, M., Tsujikawa, S., Carneiro, S., Gonzalez Nuevo, J., Carvalho, G. C., Reboucas, M. J., Carvalho, J. C., Abdalla, E., Bernui, A., Pigozzo, C., Ferreira, E. G. M., Chandrachani Devi, N., Bengaly, Jr., C. A. P., Campista, M., Amorim, A., Asari, N. V., Bongiovanni, A., Bonoli, S., Bruzual, G., Cardiel, N., Cava, A., Cid Fernandes, R., Coelho, P., Cortesi, A., Delgado, R. G., Diaz Garcia, L., Espinosa, J. M. R., Galliano, E., Gonzalez-Serrano, J. I., Falcon-Barroso, J., Fritz, J., Fernandes, C., Gorgas, J., Hoyos, C., Jimenez-Teja, Y., Lopez-Aguerri, J. A., Lopez-San Juan, C., Mateus, A., Molino, A., Novais, P., OMill, A., Oteo, I., Perez-Gonzalez, P. G., Poggianti, B., Proctor, R., Ricciardelli, E., Sanchez-Blazquez, P., Storchi-Bergmann, T., Telles, E., Schoennell, W., Trujillo, N., Vazdekis, A., Viironen, K., Daflon, S., Aparicio-Villegas, T., Rocha, D., Ribeiro, T., Borges, M., Martins, S. L., Marcolino, W., Martinez-Delgado, D., Perez-Torres, M. A., Siffert, B. B., Calvao, M. O., Sako, M., Kessler, R., Alvarez-Candal, A., De Pra, M., Roig, F., Lazzaro, D., Gorosabel, J., Lopes de Oliveira, R., Lima-Neto, G. B., Irwin, J., Liu, J. F., Alvarez, E., Balmes, I., Chueca, S., Costa-Duarte, M. V., da Costa, A. A., Dantas, M. L. L., Diaz, A. Y., Fabregat, J., Ferrari, F., Gavela, B., Gracia, S. G., Gruel, N., Gutierrez, J. L. L., Guzman, R., Hernandez-Fernandez, J. D., Herranz, D., Hurtado-Gil, L., Jablonsky, F., Laporte, R., Le Tiran, L. L., Licandro, J., Lima, M., Martin, E., Martinez, V., Montero, J. J. C., Penteado, P., Pereira, C. B., Peris, V., Quilis, V., Sanchez-Portal, M., Soja, A. C., Solano, E., Torra, J., and Valdivielso, L.: 2014, *ArXiv e-prints*

Benítez, N., Gaztañaga, E., Miquel, R., Castander, F., Moles, M., Crocce, M., Fernández-Soto, A., Fosalba, P., Ballesteros, F., Campa, J., Cardiel-Sas, L., Castilla, J., Cristóbal-Hornillos, D., Delfino, M., Fernández, E., Fernández-Sopuerta, C., García-Bellido, J., Lobo, J. A., Martínez, V. J., Ortiz, A., Pacheco, A., Paredes, S., Pons-Bordería, M. J., Sánchez, E., Sánchez, S. F., Varela, J., and de Vicente, J. F.: 2009a, *ApJ* **691**, 241

Benítez, N., Moles, M., Aguerri, J. A. L., Alfaro, E., Broadhurst, T., Cabrera-Caño, J., Castander, F. J., Cepa, J., Cerviño, M., Cristóbal-Hornillos, D., Fernández-Soto, A., González Delgado, R. M., Infante, L., Márquez, I., Martínez, V. J., Masegosa, J., Del Olmo, A., Perea, J., Prada, F., Quintana, J. M., and Sánchez, S. F.: 2009b, *ApJ* **692**, L5

Bernardi, M., Meert, A., Sheth, R. K., Vikram, V., Huertas-Company, M., Mei, S., and Shankar, F.: 2013, *ArXiv e-prints*

Blanton, M. R., Hogg, D. W., Bahcall, N. A., Brinkmann, J., Britton, M., Connolly, A. J., Csabai, I., Fukugita, M., Loveday, J., Meiksin, A., Munn, J. A., Nichol, R. C., Okamura, S., Quinn, T., Schneider, D. P., Shimasaku, K., Strauss, M. A., Tegmark, M., Vogeley, M. S., and Weinberg, D. H.: 2003, *ApJ* **592**, 819

Blanton, M. R., Schlegel, D. J., Strauss, M. A., Brinkmann, J., Finkbeiner, D., Fukugita, M., Gunn, J. E., Hogg, D. W., Ivezić, Ž., Knapp, G. R., Lupton, R. H., Munn, J. A., Schneider, D. P., Tegmark, M., and Zehavi, I.: 2005, *AJ* **129**, 2562

Borch, A., Meisenheimer, K., Bell, E. F., Rix, H.-W., Wolf, C., Dye, S., Kleinheinrich, M., Kovacs, Z., and Wisotzki, L.: 2006, *A&A* **453**, 869

Bordoloi, R., Lilly, S. J., and Amara, A.: 2010, *MNRAS* **406**, 881

Braga-Ribas, F., Sicardy, B., Ortiz, J. L., Jehin, E., Camargo, J. I. B., Assafin, M., Behrend, R., Unda-Sanzana, E., Colque, J. P., Morales, N., Tancredi, G., Roland, S., Bruzzone, S., Salvo, R., Almenares, L., Emilio, M., Schoenell, W., Gil-Hutton, R., Milone, A., Jacques, C., Vanzi, L., Kavelaars, J. J., Cacella, P., Maury, A., Alvarez, E., van der Bliek, N. S., Vieira-Martins, R., Colas, F., Lecacheux, J., Vachier, F., Roques, F., Widemann, T., Thirouin, A., Gillon, M., Manfroid, J., Bergengruen, A., Martinez, M., Capeche, J., Amorim, A., Pimentel, E., Leiva, R., Toledo, I., Almeida, L. A., Magalhães, V. S., Montaña, C. E., and Rodrigues, C. V.: 2011, in *EPSC-DPS Joint Meeting 2011*, p. 1060

Braga-Ribas, F., Sicardy, B., Ortiz, J. L., Lellouch, E., Tancredi, G., Lecacheux, J., Vieira-Martins, R., Camargo, J. I. B., Assafin, M., Behrend, R., Vachier, F., Colas, F., Morales, N., Maury, A., Emilio, M., Amorim, A., Unda-Sanzana, E., Roland, S., Bruzzone, S., Almeida, L. A., Rodrigues, C. V., Jacques, C., Gil-Hutton, R., Vanzi, L., Milone, A. C., Schoenell, W., Salvo, R., Almenares, L., Jehin, E., Manfroid, J., Sposetti, S., Tanga, P., Klotz, A., Frappa, E., Cacella, P., Colque, J. P., Neves, C., Alvarez, E. M., Gillon, M., Pimentel, E., Giacchini, B., Roques, F., Widemann, T., Magalhães, V. S., Thirouin, A., Duffard, R., Leiva, R., Toledo, I., Capeche, J., Beisker, W., Pollock, J., Cedeño Montaña, C. E., Ivarsen, K., Reichart, D., Haislip, J., and Lacluyze, A.: 2013, *ApJ* **773**, 26

Brinchmann, J., Charlot, S., White, S. D. M., Tremonti, C., Kauffmann, G., Heckman, T., and Brinkmann, J.: 2004, *MNRAS* **351**, 1151

Bruzual, G. and Charlot, S.: 2003, *MNRAS* **344**, 1000

Bundy, K.: 2006, *Ph.D. thesis*, California Institute of Technology

Bundy, K., Ellis, R. S., Conselice, C. J., Taylor, J. E., Cooper, M. C., Willmer, C. N. A., Weiner, B. J., Coil, A. L., Noeske, K. G., and Eisenhardt, P. R. M.: 2006, *ApJ* **651**, 120

Calzetti, D., Kinney, A. L., and Storchi-Bergmann, T.: 1994, *ApJ* **429**, 582

Capak, P., Abraham, R. G., Ellis, R. S., Mobasher, B., Scoville, N., Sheth, K., and Koekemoer, A.: 2007, *ApJS* **172**, 284

Cardelli, J. A., Clayton, G. C., and Mathis, J. S.: 1989, *ApJ* **345**, 245

Chabrier, G.: 2003, *ApJ* **586**, L133

Charlier, C. V. L.: 1922, *Meddelanden fran Lunds Astronomiska Observatorium Serie I* **98**, 1

Chromey, F. R. and Hasselbacher, D. A.: 1996, *PASP* **108**, 944

Cid Fernandes, R., Mateus, A., Sodré, L., Stasińska, G., and Gomes, J. M.: 2005, *MNRAS* **358**, 363

Coe, D., Benítez, N., Sánchez, S. F., Jee, M., Bouwens, R., and Ford, H.: 2006, *AJ* **132**, 926

Coe, D., Umetsu, K., Zitrin, A., Donahue, M., Medezinski, E., Postman, M., Carrasco, M., Anguita, T., Geller, M. J., Rines, K. J., Diaferio, A., Kurtz, M. J., Bradley, L., Koekemoer, A., Zheng, W., Nonino, M., Molino, A., Mahdavi, A., Lemze, D., Infante, L., Ogaz, S., Melchior, P., Host, O., Ford, H., Grillo, C., Rosati, P., Jiménez-Teja, Y., Moustakas, J., Broadhurst, T., Ascaso, B., Lahav, O., Bartelmann, M., Benítez, N., Bouwens, R., Graur, O., Graves, G., Jha, S., Jouvel, S., Kelson, D., Moustakas, L., Maoz, D., Meneghetti, M., Merten, J., Riess, A., Rodney, S., and Seitz, S.: 2012, *ApJ* **757**, 22

Cole, S., Norberg, P., Baugh, C. M., Frenk, C. S., Bland-Hawthorn, J., Bridges, T., Cannon, R., Colless, M., Collins, C., Couch, W., Cross, N., Dalton, G., De Propris, R., Driver, S. P., Efstathiou, G., Ellis, R. S., Glazebrook, K., Jackson, C., Lahav, O., Lewis, I., Lumsden, S., Maddox, S., Madgwick, D., Peacock, J. A., Peterson, B. A., Sutherland, W., and Taylor, K.: 2001, *MNRAS* **326**, 255

Cunha, C. E., Lima, M., Oyaizu, H., Frieman, J., and Lin, H.: 2009, *MNRAS* **396**, 2379

Dark Energy Survey Collaboration, Abbott, T., Abdalla, F. B., Aleksić, J., Allam, S., Amara, A., Bacon, D., Balbinot, E., Banerji, M., Bechtol, K., Benoit-Lévy, A., Bernstein, G. M., Bertin, E., Blazek, J., Bonnett, C., Bridle, S., Brooks, D., Brunner, R. J., Buckley-Geer, E., Burke, D. L., Caminha, G. B., Capozzi, D., Carlsen, J., Carnero-Rosell, A., Carollo, M., Carrasco-Kind, M., Carretero, J., Castander, F. J., Clerkin, L., Collett, T., Conselice, C., Crocce, M., Cunha, C. E., D'Andrea, C. B., da Costa, L. N., Davis, T. M., Desai, S., Diehl, H. T., Dietrich, J. P., Dodelson, S., Doel, P., Drlica-Wagner, A., Estrada, J., Etherington, J., Evrard, A. E., Fabbri, J., Finley, D. A., Flaugher, B., Foley, R. J., Fosalba, P., Frieman, J., García-Bellido, J., Gaztanaga, E., Gerdes, D. W., Giannantonio, T., Goldstein, D. A., Gruen, D., Gruendl, R. A., Guarnieri, P., Gutierrez, G., Hartley, W., Honscheid, K., Jain, B., James, D. J., Jeltema, T., Jouvel, S., Kessler, R., King, A., Kirk, D., Kron, R., Kuehn, K., Kuropatkin, N., Lahav, O., Li, T. S., Lima, M., Lin, H., Maia, M. A. G., Makler, M., Manera, M., Maraston, C., Marshall, J. L., Martini, P., McMahon, R. G., Melchior, P., Merson, A., Miller, C. J., Miquel, R., Mohr, J. J., Morice-Atkinson, X., Naidoo, K., Neilsen, E., Nichol, R. C., Nord, B., Ogando, R., Ostrovski, F., Palmese, A., Papadopoulos, A., Peiris, H. V., Peoples, J., Percival, W. J., Plazas, A. A., Reed, S. L., Refregier, A., Romer, A. K., Roodman, A., Ross, A., Rozo, E., Rykoff, E. S., Sadeh, I., Sako, M., Sánchez, C., Sanchez, E., Santiago, B., Scarpine, V., Schubnell, M., Sevilla-Noarbe, I., Sheldon, E., Smith, M., Smith, R. C., Soares-Santos, M., Sobreira, F., Soumagnac, M., Suchyta, E., Sullivan, M., Swanson, M., Tarle, G., Thaler, J., Thomas, D., Thomas, R. C., Tucker, D., Vieira, J. D., Vikram, V., Walker, A. R., Wechsler, R. H., Weller, J., Wester, W., Whiteway, L., Wilcox, H., Yanny, B., Zhang, Y., and Zuntz, J.: 2016, *MNRAS* **460**, 1270

Davidzon, I., Bolzonella, M., Coupon, J., Ilbert, O., Arnouts, S., de la Torre, S., Fritz, A., De Lucia, G., Iovino, A., Granett, B. R., Zamorani, G., Guzzo, L., Abbas, U., Adami, C., Bel, J., Bottini, D., Branchini, E., Cappi, A., Cucciati, O., Franzetti, P., Fumana, M., Garilli, B., Krywult, J., Le Brun, V., Le Fevre, O., Maccagni, D., Malek, K., Marulli, F., McCracken, H. J., Paioro, L., Peacock, J. A., Polletta, M., Pollo, A., Schlagenhaufer, H., Scodeggio, M., Tasca, L. A. . M., Tojeiro, R., Vergani, D., Zanichelli, A., Burden, A., Di Porto, C., Marchetti, A., Marinoni, C., Mellier, Y., Moscardini, L., Moutard, T., Nichol, R. C., Percival, W. J., Phleps, S., and Wolk, M.: 2013, *ArXiv e-prints*

Díaz-García, L. A., Cenarro, A. J., López-Sanjuan, C., Ferreras, I., Varela, J., Viironen, K., Cristóbal-Hornillos, D., Moles, M., Marín-Franch, A., Arnalte-Mur, P., Ascaso, B., Cerviño, M., González Delgado, R. M., Márquez, I., Masegosa, J., Molino, A., Pović, M., Alfaro, E., Aparicio-Villegas, T., Benítez, N., Broadhurst, T., Cabrera-Caño, J., Castander, F. J., Cepa, J., Fernández-Soto, A., Husillos, C., Infante, L., Aguerri,

J. A. L., Martínez, V. J., del Olmo, A., Perea, J., Prada, F., Quintana, J. M., and Gruel, N.: 2015, *A&A* **582**, A14

Drory, N., Bundy, K., Leauthaud, A., Scoville, N., Capak, P., Ilbert, O., Kartaltepe, J. S., Kneib, J. P., McCracken, H. J., Salvato, M., Sanders, D. B., Thompson, D., and Willott, C. J.: 2009, *ApJ* **707**, 1595

Duriscoe, D. M., Luginbuhl, C. B., and Moore, C. A.: 2007, *PASP* **119**, 192

Fioc, M. and Rocca-Volmerange, B.: 1997, *A&A* **326**, 950

Fontana, A., Pozzetti, L., Donnarumma, I., Renzini, A., Cimatti, A., Zamorani, G., Menci, N., Daddi, E., Giallongo, E., Mignoli, M., Perna, C., Salimbeni, S., Saracco, P., Broadhurst, T., Cristiani, S., D'Odorico, S., and Gilmozzi, R.: 2004, *A&A* **424**, 23

Fontana, A., Salimbeni, S., Grazian, A., Giallongo, E., Pentericci, L., Nonino, M., Fontanot, F., Menci, N., Monaco, P., Cristiani, S., Vanzella, E., de Santis, C., and Gallozzi, S.: 2006, *A&A* **459**, 745

Foreman-Mackey, D., Hogg, D. W., Lang, D., and Goodman, J.: 2013, *PASP* **125**, 306

Gallazzi, A., Charlot, S., Brinchmann, J., White, S. D. M., and Tremonti, C. A.: 2005, *MNRAS* **362**, 41

Gomes-Júnior, A. R., Giacchini, B. L., Braga-Ribas, F., Assafin, M., Vieira-Martins, R., Camargo, J. I. B., Sicardy, B., Timerson, B., George, T., Broughton, J., Blank, T., Benedetti-Rossi, G., Brooks, J., Dantowitz, R. F., Dunham, D. W., Dunham, J. B., Ellington, C. K., Emilio, M., Herpich, F. R., Jacques, C., Maley, P. D., Mehret, L., Mello, A. J. T., Milone, A. C., Pimentel, E., Schoenell, W., and Weber, N. S.: 2015, *ArXiv e-prints*

González Delgado, R. M., García-Benito, R., Pérez, E., Cid Fernandes, R., de Amorim, A. L., Cortijo-Ferrero, C., Lacerda, E. A. D., López Fernández, R., Vale-Asari, N., Sánchez, S. F., Mollá, M., Ruiz-Lara, T., Sánchez-Blázquez, P., Walcher, C. J., Alves, J., Aguerri, J. A. L., Bekeraité, S., Bland-Hawthorn, J., Galbany, L., Gallazzi, A., Husemann, B., Iglesias-Páramo, J., Kalinova, V., López-Sánchez, A. R., Marino, R. A., Márquez, I., Masegosa, J., Mast, D., Méndez-Abreu, J., Mendoza, A., del Olmo, A., Pérez, I., Quirrenbach, A., and Zibetti, S.: 2015, *A&A* **581**, A103

Gorosabel, J., Schoenell, W., Fernández-Soto, A., Benítez, N., Moles, M., Cenarro, A. J., de Ugarte Postigo, A., Castro-Tirado, A. J., and Thöne, C.: 2014, in *Revista Mexicana de Astronomia y Astrofisica Conference Series*, Vol. 45 of *Revista Mexicana de Astronomia y Astrofisica Conference Series*, pp 61–

Hickson, P., Gibson, B. K., and Callaghan, K. A. S.: 1994, *MNRAS* **267**, 911

Hickson, P. and Mulrooney, M. K.: 1998, *ApJS* **115**, 35

Hildebrandt, H., Wolf, C., and Benítez, N.: 2008, *A&A* **480**, 703

Hogg, D. W.: 1999, *ArXiv Astrophysics e-prints*

Hogg, D. W., Blanton, M., Strateva, I., Bahcall, N. A., Brinkmann, J., Csabai, I., Doi, M., Fukugita, M., Hennessy, G., Ivezić, Ž., Knapp, G. R., Lamb, D. Q., Lupton, R., Munn, J. A., Nichol, R., Schlegel, D. J., Schneider, D. P., and York, D. G.: 2002, *AJ* **124**, 646

Hubble, E.: 1929, *Proceedings of the National Academy of Science* **15**, 168

Hubble, E. P.: 1925, *The Observatory* **48**, 139

Ilbert, O., Capak, P., Salvato, M., Aussel, H., McCracken, H. J., Sanders, D. B., Scoville, N., Kartaltepe, J., Arnouts, S., Le Floc'h, E., Mobasher, B., Taniguchi, Y., Lamareille, F., Leauthaud, A., Sasaki, S., Thompson, D., Zamojski, M., Zamorani, G., Bardelli, S., Bolzonella, M., Bongiorno, A., Brusa, M., Caputi, K. I., Carollo, C. M., Contini, T., Cook, R., Coppa, G., Cucciati, O., de la Torre, S., de Ravel, L., Franzetti, P., Garilli, B., Hasinger, G., Iovino, A., Kampczyk, P., Kneib, J.-P., Knobel, C., Kovac, K., Le Borgne, J. F., Le Brun, V., Fèvre, O. L., Lilly, S., Looper, D., Maier, C., Mainieri, V., Mellier, Y., Mignoli, M., Murayama, T., Pellò, R., Peng, Y., Pérez-Montero, E., Renzini, A., Ricciardelli, E., Schiminovich, D., Scodeggio, M., Shioya, Y., Silverman, J., Surace, J., Tanaka, M., Tasca, L., Tresse, L., Vergani, D., and Zucca, E.: 2009, *ApJ* **690**, 1236

Ilbert, O., Salvato, M., Le Floc'h, E., Aussel, H., Capak, P., McCracken, H. J., Mobasher, B., Kartaltepe, J., Scoville, N., Sanders, D. B., Arnouts, S., Bundy, K., Cassata, P., Kneib, J.-P., Koekemoer, A., Le Fèvre, O., Lilly, S., Surace, J., Taniguchi, Y., Tasca, L., Thompson, D., Tresse, L., Zamojski, M., Zamorani, G., and Zucca, E.: 2010, *ApJ* **709**, 644

Kannappan, S. J. and Gawiser, E.: 2007, *ApJ* **657**, L5

Kauffmann, G., Heckman, T. M., White, S. D. M., Charlot, S., Tremonti, C., Brinchmann, J., Bruzual, G., Peng, E. W., Seibert, M., Bernardi, M., Blanton, M., Brinkmann, J., Castander, F., Csábai, I., Fukugita, M., Ivezic, Z., Munn, J. A., Nichol, R. C., Padmanabhan, N., Thakar, A. R., Weinberg, D. H., and York, D.: 2003, *MNRAS* **341**, 33

Lang, D., Hogg, D. W., Mierle, K., Blanton, M., and Roweis, S.: 2010, *AJ* **139**, 1782

Leavitt, H. S. and Pickering, E. C.: 1912, *Harvard College Observatory Circular* **173**, 1

Li, T., DePoy, D. L., Marshall, J. L., Nagasawa, D. Q., Carona, D. W., and Boada, S.: 2014, in *Ground-based and Airborne Instrumentation for Astronomy V*, Vol. 9147 of *Proc. SPIE*, p. 91476Z

Lilly, S. J., Le Fevre, O., Hammer, F., and Crampton, D.: 1996, *ApJ* **460**, L1

López-Sanjuan, C., Tempel, E., Benítez, N., Molino, A., Viironen, K., Díaz-García, L. A., Fernández-Soto, A., Santos, W. A., Varela, J., Cenarro, A. J., Moles, M., Arnalte-Mur, P., Ascaso, B., Montero-Dorta, A. D., Pović, M., Martínez, V. J., Nieves-Seoane, L., Stefanon, M., Hurtado-Gil, L., Márquez, I., Perea, J., Aguerri, J. A. L., Alfaro, E., Aparicio-Villegas, T., Broadhurst, T., Cabrera-Caño, J., Castander, F. J., Cepa, J., Cerviño, M., Cristóbal-Hornillos, D., González Delgado, R. M., Husillos, C., Infante, L., Masegosa, J., del Olmo, A., Prada, F., and Quintana, J. M.: 2016, *ArXiv e-prints*

LSST Dark Energy Science Collaboration: 2012, *ArXiv e-prints*

Mamajek, E. E.: 2012, *ArXiv e-prints*

Mandelbaum, R., Seljak, U., Hirata, C. M., Bardelli, S., Bolzonella, M., Bongiorno, A., Carollo, M., Contini, T., Cunha, C. E., Garilli, B., Iovino, A., Kampczyk, P., Kneib, J.-P., Knobel, C., Koo, D. C., Lamareille, F., Le Fèvre, O., Le Borgne, J.-F., Lilly, S. J., Maier, C., Mainieri, V., Mignoli, M., Newman, J. A., Oesch, P. A., Perez-Montero, E., Ricciardelli, E., Scodeggio, M., Silverman, J., and Tasca, L.: 2008, *MNRAS* **386**, 781

Manfroid, J.: 1995, *A&AS* **113**, 587

Maraston, C., Pforr, J., Henriques, B. M., Thomas, D., Wake, D., Brownstein, J. R., Capozzi, D., Bundy, K., Skibba, R. A., Beifiori, A., Nichol, R. C., Edmondson, E., Schneider, D. P., Chen, Y., Masters, K. L., Steele, O., Bolton, A. S., York, D. G., Bizyaev, D., Brewington, H., Malanushenko, E., Malanushenko, V., Snedden, S., Oravetz, D., Pan, K., Shelden, A., and Simmons, A.: 2012, *ArXiv e-prints*

Maraston, C., Pforr, J., Renzini, A., Daddi, E., Dickinson, M., Cimatti, A., and Tonini, C.: 2010, *MNRAS* **407**, 830

Márquez, I., Povic, M., Netzer, H., Masegosa, J., Nordon, R., Pérez, E., and Schoenell, W.: 2017, in S. Arribas, A. Alonso-Herrero, F. Figueras, C. Hernández-Monteagudo, A. Sánchez-Lavega, and S. Pérez-Hoyos (eds.), *Highlights on Spanish Astrophysics IX*, pp 181–186

Minniti, D., Lucas, P. W., Emerson, J. P., Saito, R. K., Hempel, M., Pietrukowicz, P., Ahumada, A. V., Alonso, M. V., Alonso-Garcia, J., Arias, J. I., Bandyopadhyay, R. M., Barbá, R. H., Barbuy, B., Bedin, L. R., Bica, E., Borissova, J., Bronfman, L., Carraro, G., Catelan, M., Clariá, J. J., Cross, N., de Grijs, R., Dékány, I., Drew, J. E., Fariña, C.,

Feinstein, C., Fernández Lajús, E., Gamen, R. C., Geisler, D., Gieren, W., Goldman, B., Gonzalez, O. A., Gunthardt, G., Gurovich, S., Hambly, N. C., Irwin, M. J., Ivanov, V. D., Jordán, A., Kerins, E., Kinemuchi, K., Kurtev, R., López-Corredoira, M., Maccarone, T., Masetti, N., Merlo, D., Messineo, M., Mirabel, I. F., Monaco, L., Morelli, L., Padilla, N., Palma, T., Parisi, M. C., Pignata, G., Rejkuba, M., Roman-Lopes, A., Sale, S. E., Schreiber, M. R., Schröder, A. C., Smith, M., , Jr., L. S., Soto, M., Tamura, M., Tappert, C., Thompson, M. A., Toledo, I., Zoccali, M., and Pietrzynski, G.: 2010, *New A* **15**, 433

Moles, M., Benítez, N., Aguerri, J. A. L., Alfaro, E. J., Broadhurst, T., Cabrera-Caño, J., Castander, F. J., Cepa, J., Cerviño, M., Cristóbal-Hornillos, D., Fernández-Soto, A., González Delgado, R. M., Infante, L., Márquez, I., Martínez, V. J., Masegosa, J., del Olmo, A., Perea, J., Prada, F., Quintana, J. M., and Sánchez, S. F.: 2008, *AJ* **136**, 1325

Molino, A., Benítez, N., Ascaso, B., Coe, D., Postman, M., Jouvel, S., Host, O., Lahav, O., Seitz, S., Medezinski, E., Rosati, P., Schoenell, W., Koekemoer, A., Jimenez-Teja, Y., Broadhurst, T., Melchior, P., Balestra, I., Bartelmann, M., Bouwens, R., Bradley, L., Czakon, N., Donahue, M., Ford, H., Graur, O., Graves, G., Grillo, C., Infante, L., Jha, S. W., Kelson, D., Lazkoz, R., Lemze, D., Maoz, D., Mercurio, A., Meneghetti, M., Merten, J., Mostazas, L., Nonino, M., Orgaz, S., Riess, A., Rodney, S., Sayers, J., Umetsu, K., Zheng, W., and Zitrin, A.: 2017, *ArXiv e-prints*

Molino, A., Benítez, N., Moles, M., Fernández-Soto, A., Cristóbal-Hornillos, D., Ascaso, B., Jiménez-Teja, Y., Schoenell, W., Arnalte-Mur, P., Pović, M., Coe, D., López-Sanjuan, C., Díaz-García, L. A., Varela, J., Stefanon, M., Cenarro, J., Matute, I., Masegosa, J., Márquez, I., Perea, J., Del Olmo, A., Husillos, C., Alfaro, E., Aparicio-Villegas, T., Cerviño, M., Huertas-Company, M., Aguerri, J. A. L., Broadhurst, T., Cabrera-Caño, J., Cepa, J., González, R. M., Infante, L., Martínez, V. J., Prada, F., and Quintana, J. M.: 2014, *MNRAS* **441**, 2891

Moster, B. P., Somerville, R. S., Newman, J. A., and Rix, H.-W.: 2011, *ApJ* **731**, 113

Moustakas, J., Coil, A., Aird, J., Blanton, M. R., Cool, R. J., Eisenstein, D. J., Mendez, A. J., Wong, K. C., Zhu, G., and Arnouts, S.: 2013, *ArXiv e-prints*

Muna, D., Alexander, M., Allen, A., Ashley, R., Asmus, D., Azzollini, R., Bannister, M., Beaton, R., Benson, A., Berriman, G. B., Bilicki, M., Boyce, P., Bridge, J., Cami, J., Cangi, E., Chen, X., Christiny, N., Clark, C., Collins, M., Comparat, J., Cook, N., Croton, D., Delberth Davids, I., Depagne, É., Donor, J., dos Santos, L. A., Douglas, S., Du, A., Durbin, M., Erb, D., Faes, D., Fernández-Trincado, J. G., Foley, A., Fotopoulou, S., Frimann, S., Frinchaboy, P., Garcia-Dias, R.,

Gawryszczak, A., George, E., Gonzalez, S., Gordon, K., Gorgone, N., Gosmeyer, C., Grasha, K., Greenfield, P., Grellmann, R., Guillochon, J., Gurwell, M., Haas, M., Hagen, A., Haggard, D., Haines, T., Hall, P., Hellwing, W., Herenz, E. C., Hinton, S., Hlozek, R., Hoffman, J., Holman, D., Holwerda, B. W., Horton, A., Hummels, C., Jacobs, D., Juel Jensen, J., Jones, D., Karick, A., Kelley, L., Kenworthy, M., Kitchener, B., Klaes, D., Kohn, S., Konorski, P., Krawczyk, C., Kuehn, K., Kuutma, T., Lam, M. T., Lane, R., Liske, J., Lopez-Camara, D., Mack, K., Mangham, S., Mao, Q., Marsh, D. J. E., Mateu, C., Maurin, L., McCormac, J., Momcheva, I., Monteiro, H., Mueller, M., Munoz, R., Naidu, R., Nelson, N., Nitschelm, C., North, C., Nunez-Iglesias, J., Ogaz, S., Owen, R., Parejko, J., Patrício, V., Pepper, J., Perrin, M., Pickering, T., Piscionere, J., Pogge, R., Poleski, R., Pourtsidou, A., Price-Whelan, A. M., Rawls, M. L., Read, S., Rees, G., Rein, H., Rice, T., Riemer-Sørensen, S., Rusomarov, N., Sanchez, S. F., Santander-García, M., Sarid, G., Schoenell, W., Scholz, A., Schuhmann, R. L., Schuster, W., Scicluna, P., Seidel, M., Shao, L., Sharma, P., Shulevski, A., Shupe, D., Sifón, C., Simmons, B., Sinha, M., Skillen, I., Soergel, B., Spriggs, T., Srinivasan, S., Stevens, A., Streicher, O., Suchyta, E., Tan, J., Telford, O. G., Thomas, R., Tonini, C., Tremblay, G., Tuttle, S., Urrutia, T., Vaughan, S., Verdugo, M., Wagner, A., Walawender, J., Wetzel, A., Willett, K., Williams, P. K. G., Yang, G., Zhu, G., and Zonca, A.: 2016, *ArXiv e-prints*

Muzzin, A., Marchesini, D., Stefanon, M., Franx, M., McCracken, H. J., Milvang-Jensen, B., Dunlop, J. S., Fynbo, J. P. U., Brammer, G., Labbé, I., and van Dokkum, P. G.: 2013, *ApJ* **777**, 18

Pacifici, C., Kassin, S. A., Weiner, B. J., Holden, B., Gardner, J. P., Faber, S. M., Ferguson, H. C., Koo, D. C., Primack, J. R., Bell, E. F., Dekel, A., Gawiser, E., Giavalisco, M., Rafelski, M., Simons, R. C., Barro, G., Croton, D. J., Davé, R., Fontana, A., Grogin, N. A., Koekemoer, A. M., Lee, S.-K., Salmon, B., Somerville, R., and Behroozi, P.: 2016, *ApJ* **832**, 79

Panter, B., Heavens, A. F., and Jimenez, R.: 2004, *MNRAS* **355**, 764

Pović, M., Márquez, I., Netzer, H., Masegosa, J., Nordon, R., Pérez, E., and Schoenell, W.: 2016, *MNRAS* **462**, 2878

Pozzetti, L., Bolzonella, M., Lamareille, F., Zamorani, G., Franzetti, P., Le Fèvre, O., Iovino, A., Temporin, S., Ilbert, O., Arnouts, S., Charlot, S., Brinchmann, J., Zucca, E., Tresse, L., Scodeggio, M., Guzzo, L., Bottini, D., Garilli, B., Le Brun, V., Maccagni, D., Picat, J. P., Scaramella, R., Vettolani, G., Zanichelli, A., Adami, C., Bardelli, S., Cappi, A., Ciliegi, P., Contini, T., Foucaud, S., Gavignaud, I., McCracken, H. J., Marano, B., Marinoni, C., Mazure, A., Meneux, B., Merighi, R., Paltani, S., Pellò, R., Pollo, A., Radovich, M., Bondi, M., Bongiorno, A., Cucciati, O., de

la Torre, S., Gregorini, L., Mellier, Y., Merluzzi, P., Vergani, D., and Walcher, C. J.: 2007, *A&A* **474**, 443

Pozzetti, L., Bolzonella, M., Zucca, E., Zamorani, G., Lilly, S., Renzini, A., Moresco, M., Mignoli, M., Cassata, P., Tasca, L., Lamareille, F., Maier, C., Meneux, B., Halliday, C., Oesch, P., Vergani, D., Caputi, K., Kovač, K., Cimatti, A., Cucciati, O., Iovino, A., Peng, Y., Carollo, M., Contini, T., Kneib, J.-P., Le Févre, O., Mainieri, V., Scodeggio, M., Bardelli, S., Bongiorno, A., Coppa, G., de la Torre, S., de Ravel, L., Franzetti, P., Garilli, B., Kampczyk, P., Knobel, C., Le Borgne, J.-F., Le Brun, V., Pellò, R., Perez Montero, E., Ricciardelli, E., Silverman, J. D., Tanaka, M., Tresse, L., Abbas, U., Bottini, D., Cappi, A., Guzzo, L., Koekemoer, A. M., Leauthaud, A., Maccagni, D., Marinoni, C., McCracken, H. J., Memeo, P., Porciani, C., Scaramella, R., Scarlata, C., and Scoville, N.: 2010, *A&A* **523**, A13

Rheault, J.-P., DePoy, D. L., Behm, T. W., Kylberg, E. W., Cabral, K., Allen, R., and Marshall, J. L.: 2010, in *Ground-based and Airborne Instrumentation for Astronomy III*, Vol. 7735 of *Proc. SPIE*, p. 773564

Rueda-Teruel, S., Yanes-Díaz, A., Antón, J. L., Rueda-Teruel, F., Moles, M., Cenarro, A. J., Marín-Franch, A., Ederoclite, A., Gruel, N., Varela, J., Cristobal-Hornillos, D., Chueca, S., Díaz-Martín, M. C., Guillén, L., Luis-Simoes, R., Maícas, N., Lamadrid, J. L., López-Sainz, A. L., Hernández-Fuertes, J., Valdivielso, L., Mendes de Oliveira, C., Penteado, P., Schoenell, W., and Kanaan, A.: 2013, in J. C. Guirado, L. M. Lara, V. Quilis, and J. Gorgas (eds.), *Highlights of Spanish Astrophysics VII*, pp 954–954

Schechter, P.: 1976, *ApJ* **203**, 297

Schoenell, W.: 2012, *Master's thesis*, Universidade Federal de Santa Catarina, Centro de Ciências Físicas e Matemáticas. Programa de Pós-Graduação em Física.

Schoenell, W., Benítez, N., and Cid Fernandes, R.: 2014, in *Revista Mexicana de Astronomia y Astrofisica Conference Series*, Vol. 44 of *Revista Mexicana de Astronomia y Astrofisica, vol. 27*, pp 186–187

Schoenell, W., Cid Fernandes, R., Benítez, N., and Vale Asari, N.: 2013, in J. C. Guirado, L. M. Lara, V. Quilis, and J. Gorgas (eds.), *Highlights of Spanish Astrophysics VII*, pp 405–410

Sheldon, E. S., Cunha, C. E., Mandelbaum, R., Brinkmann, J., and Weaver, B. A.: 2012, *ApJS* **201**, 32

Silva, L., Granato, G. L., Bressan, A., and Danese, L.: 1998, *ApJ* **509**, 103

Silva, P. H., Schoenell, W., Ribeiro, T., and Kanaan, A.: 2017, *astroufsc/chimera: Version 1.0*

Sivia, D. and Sikilling, J.: 2006, *Data Analysis: A Bayesian Tutorial*, Oxford University Press, 2nd edition

Szomoru, D., Franx, M., van Dokkum, P. G., Trenti, M., Illingworth, G. D., Labbé, I., and Oesch, P.: 2013, *ApJ* **763**, 73

Taniguchi, Y., Scoville, N., Murayama, T., Sanders, D. B., Mobasher, B., Aussel, H., Capak, P., Ajiki, M., Miyazaki, S., Komiyama, Y., Shioya, Y., Nagao, T., Sasaki, S. S., Koda, J., Carilli, C., Giavalisco, M., Guzzo, L., Hasinger, G., Impey, C., LeFevre, O., Lilly, S., Renzini, A., Rich, M., Schinnerer, E., Shopbell, P., Kaifu, N., Karoji, H., Arimoto, N., Okamura, S., and Ohta, K.: 2007, *ApJS* **172**, 9

Taylor, E. N., Hopkins, A. M., Baldry, I. K., Brown, M. J. I., Driver, S. P., Kelvin, L. S., Hill, D. T., Robotham, A. S. G., Bland-Hawthorn, J., Jones, D. H., Sharp, R. G., Thomas, D., Liske, J., Loveday, J., Norberg, P., Peacock, J. A., Bamford, S. P., Brough, S., Colless, M., Cameron, E., Conselice, C. J., Croom, S. M., Frenk, C. S., Gunawardhana, M., Kuijken, K., Nichol, R. C., Parkinson, H. R., Phillipps, S., Pimbblet, K. A., Popescu, C. C., Prescott, M., Sutherland, W. J., Tuffs, R. J., van Kampen, E., and Wijesinghe, D.: 2011, *MNRAS* **418**, 1587

Tojeiro, R., Heavens, A. F., Jimenez, R., and Panter, B.: 2007, *MNRAS* **381**, 1252

Tokovinin, A., Baumont, S., and Vasquez, J.: 2003, *MNRAS* **340**, 52

Tokovinin, A. and Heathcote, S.: 2006, *PASP* **118**, 1165

Tokovinin, A. and Kornilov, V.: 2007, *MNRAS* **381**, 1179

Tremonti, C. A., Heckman, T. M., Kauffmann, G., Brinchmann, J., Charlot, S., White, S. D. M., Seibert, M., Peng, E. W., Schlegel, D. J., Uomoto, A., Fukugita, M., and Brinkmann, J.: 2004, *ApJ* **613**, 898

Walcher, C. J., Lamareille, F., Vergani, D., Arnouts, S., Buat, V., Charlot, S., Tresse, L., Le Fèvre, O., Bolzonella, M., Brinchmann, J., Pozzetti, L., Zamorani, G., Bottini, D., Garilli, B., Le Brun, V., Maccagni, D., Milliard, B., Scaramella, R., Scodeggio, M., Vettolani, G., Zanichelli, A., Adami, C., Bardelli, S., Cappi, A., Ciliegi, P., Contini, T., Franzetti, P., Foucaud, S., Gavignaud, I., Guzzo, L., Ilbert, O., Iovino, A., McCracken, H. J., Marano, B., Marinoni, C., Mazure, A., Meneux, B., Merighi, R., Paltani, S., Pellò, R., Pollo, A., Radovich, M., Zucca, E., Lonsdale, C., and Martin, C.: 2008, *A&A* **491**, 713

Wild, V., Almaini, O., Cirasuolo, M., Dunlop, J., McLure, R., Bowler, R., Ferreira, J., Bradshaw, E., Chuter, R., and Hartley, W.: 2014, *ArXiv e-prints*

Wilkins, S. M., Gonzalez-Perez, V., Baugh, C. M., Lacey, C. G., and Zuntz, J.: 2013, *MNRAS* **431**, 430

Wittman, D.: 2009, *ApJ* **700**, L174

Wolf, C., Meisenheimer, K., Rix, H.-W., Borch, A., Dye, S., and Kleinheinrich, M.: 2003, *A&A* **401**, 73

Wuyts, S., Labbé, I., Förster Schreiber, N. M., Franx, M., Rudnick, G., Brammer, G. B., and van Dokkum, P. G.: 2008, *ApJ* **682**, 985

Yanes-Díaz, A., Antón, J. L., Rueda-Teruel, S., Guillén-Civera, L., Bello, R., Jiménez-Mejías, D., Chueca, S., Lasso-Cabrera, N. M., Suárez, O., Rueda-Teruel, F., Cenarro, A. J., Cristobal-Hornillos, D., Marin-Franch, A., Luis-Simoes, R., López-Alegre, G., Rodríguez-Hernández, M. A. C., Moles, M., Ederoclite, A., Varela, J., Vazquez Ramió, H., Díaz-Martín, M. C., Iglesias-Marzoa, R., Maicas, N., Lamadrid, J. L., Lopez-Sainz, A., Hernández-Fuertes, J., Valdivielso, L., Mendes de Oliveira, C., Penteado, P., Schoenell, W., and Kanaan, A.: 2014, in *Software and Cyberinfrastructure for Astronomy III*, Vol. 9152 of *Proc. SPIE*, p. 915215

Yanes-Díaz, A., Rueda-Teruel, S., Antón, J. L., Rueda-Teruel, F., Moles, M., Cenarro, A. J., Marín-Franch, A., Ederoclite, A., Gruel, N., Varela, J., Cristóbal-Hornillos, D., Chueca, S., Díaz-Martín, M. C., Guillén, L., Luis-Simoes, R., Maícas, N., Lamadrid, J. L., López-Sainz, A., Hernández-Fuertes, J., Valdivielso, L., Mendes de Oliveira, C., Penteado, P., Schoenell, W., and Kanaan, A.: 2012, in *Society of Photo-Optical Instrumentation Engineers (SPIE) Conference Series*, Vol. 8448 of *Society of Photo-Optical Instrumentation Engineers (SPIE) Conference Series*

Zernike, v. F.: 1934, *Physica* **1**, 689